Master's thesis

NTNU
Norwegian University of Science and Technology
Faculty of Engineering
Department of Mechanical and Industrial Engineering

Kristoffer Sjøwall

Hydrodynamic Design Principles and Structural Verification of a Hydrofoil Concept for Kiteboarding

Master's thesis in Engineering Design and Materials
Supervisor: Nils Petter Vedvik
July 2022

NTNU
Norwegian University of
Science and Technology

Kristoffer Sjøwall

Hydrodynamic Design Principles and Structural Verification of a Hydrofoil Concept for Kiteboarding

Master's thesis in Engineering Design and Materials
Supervisor: Nils Petter Vedvik
July 2022

Norwegian University of Science and Technology
Faculty of Engineering
Department of Mechanical and Industrial Engineering

NTNU
Norwegian University of
Science and Technology

NTNU
Kunnskap for en bedre verden

Department of Mechanical and Industrial Engineering

TMM4960 - Produktutvikling og materialer
Masteroppgave

Hydrodynamic Design Principles and Structural Verification of a Hydrofoil Concept for Kiteboarding

Author:
Kristoffer Sjøwall

July, 2022

Abstract

The use of hydrofoils in kiteboarding has gained traction in recent years and will be featured for the first time in the 2024 Olympic Games. Since its inception, the primary development effort has been on optimizing performance and implementing advanced materials, such as pre-preg carbon fiber. This has led to hydrofoils being expensive. This thesis aims to investigate the design principles of hydrofoils and to explore a unique and affordable design concept with adequate performance compared to more traditional designs. The significance of hydrodynamic design parameters was analyzed through the use of Xflr5 simulations. The results were summarized in a table that can be consulted for design development. By using the table, the hydrodynamic design was tuned for the requirements of novice riders. A structural design concept was proposed through a comparison of different materials and manufacturing methods. The concept incorporates a compression molded carbon-epoxy material known as forged carbon fiber. Due to the lack of information about forged carbon fiber, 4-point flexural testing was conducted to determine mechanical properties. The elastic modulus was determined to be 25670MPa, and the characteristic strength was determined to be 191MPa. A finite element analysis was conducted in Abaqus to investigate the proposed structural concept. The viability of forged CFRP as a structural material was compared with more traditional materials. It was found that the strength of forged CFRP was not adequate for this first design. A second design iteration was developed, and forged CFRP this design succeeded with a safety factor of 1.33. Based on the successful design, 60%-scale prototype parts were made of a forged carbon fibre mounting plate and fuselage. The parts were compression molded in 3D printed PLA molding tools. The molding process was successful, but the parts could not be considered fit for commercial applications. It was concluded that the design concept and manufacturing process has the potential for creating inexpensive, lightweight parts. However, better manufacturing equipment is needed to achieve a commercial standard. It was also hypothesized that better mechanical properties could be achieved with solid, permanent molds. However, the manufacturing process used in this thesis was deemed an efficient way of prototyping parts. Further research should aim at using industry-standard manufacturing equipment to explore the full potential of compression forging and the related mechanical properties.

Sammendrag

Bruken av hydrofoiler i kiteboarding har de siste årene blitt stadig mer populært og vil for første gang bli inkludert i de olympiske leker i 2024. Siden oppstarten har den primære utviklingsinnsatsen vært å optimalisere ytelsen og å implementere avanserte materialer, som pre-preg karbonfiber. Dette har ført til at hydrofoiler er dyre. Denne oppgaven tar sikte på å undersøke designprinsippene til hydrofoiler og å utforske et unikt og rimelig designkonsept med tilstrekkelig ytelse sammenlignet med mer tradisjonelle design. Betydningen av hydrodynamiske designparametere ble analysert ved bruk av Xflr5-simuleringer. Resultatene ble oppsummert i en tabell som kan konsulteres for designutvikling. Ved å bruke tabellen ble det hydrodynamiske designet tilpasset kravene til nybegynnere. Et strukturelt designkonsept ble foreslått gjennom en sammenligning av forskjellige materialer og produksjonsmetoder. Konseptet inneholder et kompresjonsstøpt karbon-epoksy material kjent som smidd karbonfiber. På grunn av mangel på informasjon om smidd karbonfiber, ble 4-punkts bøyestesting utført for å bestemme mekaniske egenskaper. Den elastiske modulusen ble bestemt til å være 25670 MPa, og den karakteristiske styrken ble bestemt til å være 191 MPa. En endelig elementanalyse ble utført i Abaqus for å undersøke det foreslåtte strukturelle konseptet. Potensialet til smidd CFRP som et strukturelt materiale ble sammenlignet med mer tradisjonelle materialer. Det ble funnet at styrken til smidd CFRP ikke var tilstrekkelig for dette designet. En designiterasjon til ble utviklet, og dette designet lyktes med en sikkerhetsfaktor på 1,33. Basert på det vellykkede designet ble prototypedeler i 60%-skala laget av en smidd karbonfiber for mounting plate og fuselage. Delene ble kompresjonsstøpt i 3D-printede PLA-støpeverktøy. Støpeprosessen var vellykket, men delene kunne ikke anses som egnet for kommersiell bruk. Det ble konkludert med at designkonseptet og produksjonsprosessen har potensial for å lage rimelige, lette deler. Bedre produksjonsutstyr er imidlertid nødvendig for å oppnå en kommersiell standard. Det ble også antatt at bedre mekaniske egenskaper kunne oppnås med solide, permanente former. Imidlertid ble produksjonsprosessen brukt i denne oppgaven ansett som en effektiv måte å lage prototyper på. Ytterligere forskning bør ta sikte på å utnytte industrielt produksjonsutstyr for å utforske det fulle potensialet til kompresjonssmiing og de tilhørende mekaniske egenskapene.

Acknowledgements

As a person with great love for the ocean, it has been a privilege to write a thesis related to a topic I am genuinely passionate about. I would like to direct a special thanks to my supervisor Nils Petter Vedvik for mentoring me through this project and for letting me write a thesis on a topic of my own creation. It has been a great motivation to be able to focus my effort on developing a product that one day potentially can turn into a business. Most of all, I need to thank my family for their continuous support not only in regard to this thesis but throughout my entire life leading up to this moment.

THIS THESIS IS DEDICATED

TO THE GREAT NATURAL FORCES OF THE EARTH

AND TO THE ONES ON A QUEST TO TAME THEM

Table of Contents

List of Figures

List of Tables

Nomenclature

α	Angle of Attack
δ_{max}	The maximum deflection
ϵ	Strain
γ	Wing dihedral angle
κ	Curvature
μ	Dynamic viscosity
ν	Kinematic viscosity
ν_{12}	Major Poisson's ratio
ν_f	Poisson's ratio of fibre reinforcement
ν_m	Poisson's ratio of matrix
ρ	Density
$\sigma(x, y)$	Stress as a function of the x and y coordinate
σ	Standard deviation
σ_{max}	The maximum stress
a	Outer span length
AC	Aerodynamic Centre
AoA	Angle of Attack
AoI	Angle of Incidence
AR	Aspect ratio
AR_h	Rear wing aspect ratio
B	Spiral stability parameter
b	Inner span length
b	The width of a cross-section
b	Wingspan
BMC	Bulk molding compound

c	Chord length
C_D	Coefficient of drag
C_L	Coefficient of lift
C_m	Coefficient of moment
CAE	Computer Aided Engineering
$CFRP$	Carbon Fibre Reinforced Polymer
CG	Centre of Gravity
CoP	Centre of Pressure
COV	Coefficient of variation
D_i	Induced drag
DOF	Degree of Freedom
E	Elastic modulus
E_1	Elastic modulus in the longitudinal direction
E_2	Elastic modulus in the transverse direction
E_f	Elastic modulus of the fibres
E_m	Elastic modulus of the matrix
F	Force
FEA	Finite Element Analysis
FEM	Finite Element Method
FOS	Factor of Safety
G	The Shear modulus
h	The height of a cross-section
I	The second moment of area
I_z	The second moment of area with respect to the z-axis
L	Length
l	Length in relation to Reynolds number
l_h	Rear wing moment arm
l_v	Mast moment arm
$M(x)$	The moment as a function of the x-coordinate
M	Moment
m_r	Resin mass
m_t	Total mass
$M_z(x)$	The moment about the z-axis as a function of the x-coordinate
m_{fibre}	Fibre mass
M_{max}	The maximum moment

m_{part}	Part mass
MAC	Mean Aerodynamic Chord
NP	Neutral Point
$p_{0.50}$	5th percentile
PVC	Polyvinyl chloride
Re	Reynolds number
S	Plan area
S_h	Rear wing plan area
S_v	Mast plan area
SD	Standard Deviation
SM	Static Margin
V	Velocity
V_f	Fibre volume fraction
V_h	Rear wing volume coefficient
V_m	Matrix volume fraction
V_v	Mast volume coefficient
V_{part}	Part volume
x	Longitudinal position
x_{cg}	Longitudinal location of the centre of gravity
x_{np}	Longitudinal loacation of the neutral point
y	Span wise position
z	Vertical position

Chapter 1

Introduction

1.1 Background - The Hydrofoil Used in Board Sports

The hydrofoil concept has come a long way since the Scottish-American inventor Alexander Graham Bell developed the first hydrofoil boat in 1906. Later, in 1919 his model HD-4 set the new world record as the fastest seafaring vessel with a top speed of 114km/h [32]. Since then, the hydrofoil's application has spanned several hydrocrafts, both military, commercial, and recreational. In recent years the hydrofoil concept has taken the aquatic board sports market by storm, offering new advantages over traditional designs, and has even created sub-disciplines within the sports. In surfing, the reduced drag of a hydrofoil enables the surfers to catch weaker waves and also to catch the waves earlier, further out from shore. This has opened a market opportunity in locations that rarely experience quality waves, such as the Mediterranean coast of Spain [19]. In kiteboarding, the reduced drag offered by hydrofoils enables the kiteboarders to perform in low wind conditions, where hydroplaning would prove exceedingly difficult using traditional boards. It also enables the kiteboarders to utilize smaller, more agile kites in good wind conditions. This fact has caused the hydrofoil designs to evolve into several categories depending on the desired use case in respective disciplines. Respective hydrofoil designs are now specialized for high-speed racing, low-wind conditions, and freestyle. The low drag offered by the hydrofoil has even spurred the advent of a radical new kite design, known as the kite foil. This kite encompasses elements from both traditional kites and windsurfing sails, and its invention can be regarded as the genesis of a new sport.

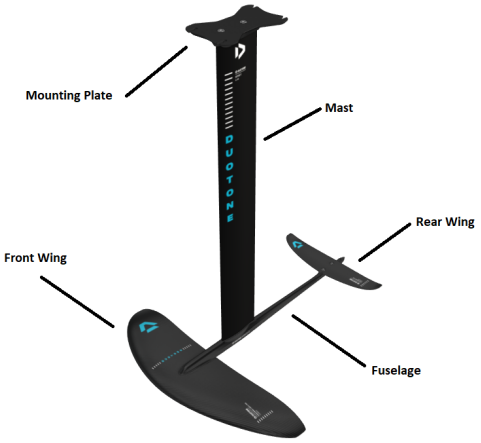

Figure 1.1: A Duotone hydrofoil with all the main parts labeled.

The typical hydrofoil assembly used in kiteboarding consists of five main parts. The assembly includes the front wing, the rear wing, the fuselage, the mast, and the mounting plate. The front wing is the largest of the wings, and its purpose is to provide enough lift to counter the force of gravity exerted on the hydrofoil and rider. The rear wing is smaller in area compared to the front wing, and its function is to counter the moment created due to the offset in the distance between the centre of gravity and the resultant force of the lift distribution produced by the front wing. The fuselage serves as a means to connect the front and rear wing, as well as the mast. The fuselage length determines the leverage arm distance from the front wing to the rear wing. The mast separates the board from the hydrofoil wings and enables the board and rider to be lifted entirely out of the water when forward speed is sufficient. The mast length influences the distance between the point of resultant lift and the centre of gravity in the vertical direction. This distance impacts the handling dynamics of the hydrofoil during operation. Lastly, the mounting plate serves as a simple solution for connecting the mast to the board. In addition to the main parts, different brands utilize auxiliary components, such as shims and other parts that aid in connecting different components.

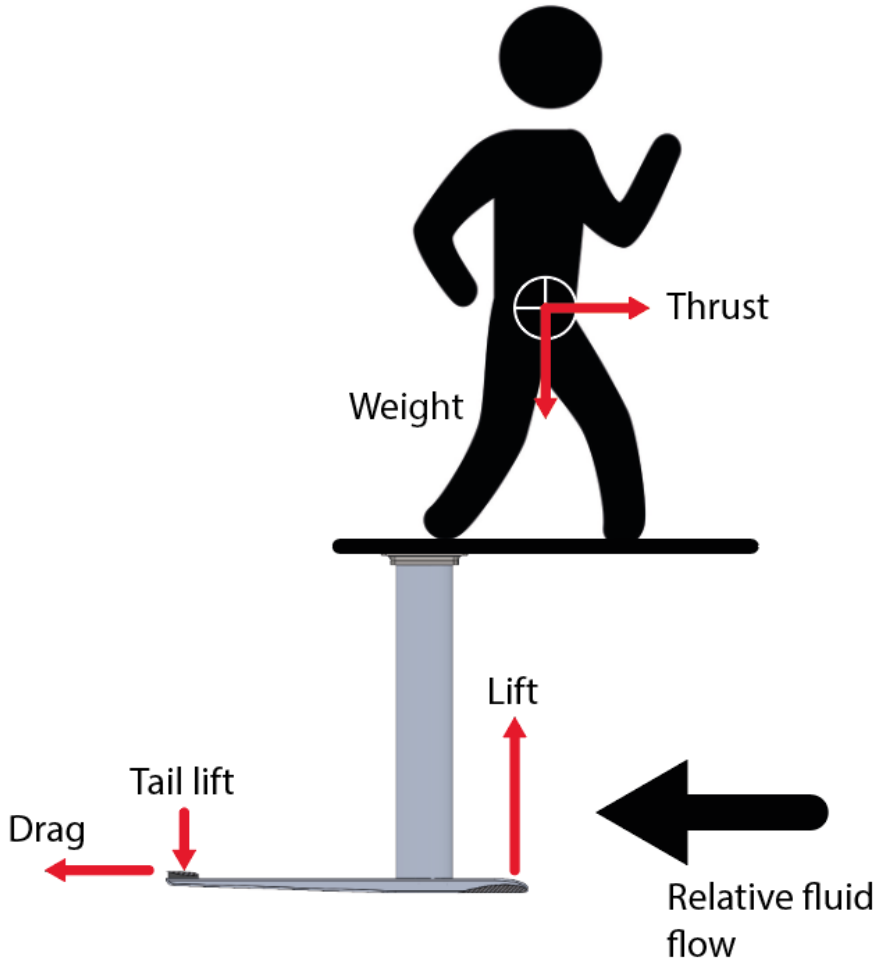

Figure 1.2: An illustration of a rider on a hydrofoil showing the main forces and the relative fluid flow.

1.2 Motivation

By now, all the major kiteboarding brands offer different versions of hydrofoils, and many offer a full range of products that cater to the individual needs and desired disciplines of the consumer. This new branch within the kiteboarding sport has also created room in the market for brands that focus solely on hydrofoil development and are pushing the envelope for new design innovations. Even though different brands implement different design solutions, many similarities occur amongst the offered products. A pre-study was conducted that gathered information about the design choices from the largest state-of-the-art hydrofoil manufacturers. The goal was to find and compare their material choices, manufacturing processes, and design trends to evaluate what is regarded as the industry standard. The task was executed by gathering technical information about the products from the manufacturer's official websites. The information is summarized in Table 1.1. A commonality between all the hydrofoils investigated is the high price point. The price usually ranges between $1,000.00 and $3,000.00, depending on the brand and the materials used. It is desired to investigate a manufacturing process for a lower-cost alternative, as such an alternative is hypothesized to draw more new consumers into the market. Through investigation of design principles, materials, and manufacturing processes, finding a lower-cost solution to traditional designs should be possible.

Table 1.1: Information about materials and manufacturing methods utilized by different brands in their hydrofoil production. Publicly available on their respective websites.

Brand	**Front Wing**	**Rear Wing**	**Fuselage**	**Mast**
Duotone	30°carbon lay-up for torsional stiffness	30°carbon lay-up for torsional stiffness	Aluminium or carbon composite	Aluminium mast with helicoils or carbon composite
Cabrinha	EPS/full prepreg carbon lay-up	EPS/full prepreg carbon lay-up	CNC-machined 6061-T6 aluminium	Extruded 6061-T6 aluminium hollow with helicoils
North	Lightweight foam/prepreg carbon and 3K carbon finish	Lightweight foam/prepreg carbon and 3K carbon finish	CNC-machined 6061-T6 or Prepreg carbon layup	Aluminium or carbon composite
Eleveight	EPS/biaxial carbon lay-up	EPS/biaxial carbon lay-up	CNC-machined 6061-T6 aluminium	Aluminium
F-one	Injected polymer reinforced carbon fiber	Injected polymer reinforced carbon fiber	Aluminium or carbon composite	Extruded 6063 aluminium or carbon composite
Core	PU/carbon fibre	PU/carbon fibre	CNC-machined 6063 aluminium	Extruded 6063 Aluminium thin-walled

The information from the websites is limited and varies in detail between the brands, but it is still possible to extract some key points about their main hydrofoil components. All the brands in question manufacture the front and rear wings using a foam core and a carbon composite skin, but they seem to utilize different composite manufacturing techniques and core material choices. Regarding the fuselage, the trend seems in favor of CNC-machined 6061-T6 aluminum. The trend also suggests that the mast is manufactured through aluminum extrusion, an efficient way of manufacturing parts with constant cross-section. However, there is not enough data to conclude what is the most favored aluminum alloy for this extruded part. Several brands also offer high-end carbon composite fuselages and masts, and some even complete assemblies manufactured into a single part. Public information also informs that the industry standard incorporates mounting plates with a rectangular four-bolt pattern where the longitudinal distance between the holes is 165mm, and the lateral distance between the holes is 90mm. The connection between the mounting plate and the board uses M8 bolts, and other hardware is typically 316-grade stainless steel. Some manufacturers also report incorporating helicoils for the internally threaded connections, which is

a favorable alternative to taped aluminum.

1.3 The Design Process

The development process for this hydrofoil to be used in kiteboarding depends on some distinct steps. The first is to define the hydrodynamic design parameters so the product will suit the intended application. In the case of the hydrofoil, these hydrodynamic parameters are closely related to the principles of an aircraft, as the working theory is essentially the same. In the same way an aircraft is designed for a specific use case that encompasses parameter decisions that influence behavior such as slow vs. fast cruising speed, stable flight vs. quick maneuvers - the hydrofoil needs to be designed with the same principles in mind. In this project, it is desired to design the hydrofoil in relation to the requirements and needs of an entry-level hydrofoil rider, as a low-cost alternative may draw more consumers into the market. Xflr5 is software based on Xfoil that can simulate 2D foil profiles, complete 3D models, and conduct stability analysis. It is a suitable tool for making design decisions and evaluating if hydrodynamic parameters meet the desired product requirements. The simulations also offer means to calculate the loads that will act on the hydrofoil during the operational conditions. The design parameters that need to be investigated include;

- Foil profiles
- Area of the front wing
- Area of the rear wing
- Distance between the front and rear wing (fuselage length)
- Angle of incidence of the front wing
- Angle of incidence of the rear wing
- Wing aspect ratios

The second step in the development process is to create a CAD model of a hydrofoil concept based on the decided design parameters found through the hydrodynamic analysis in Xflr5. It is necessary to create individual models of all the parts involved and join them in an assembly. For this project, the CAD models will be created using Dassault Systèmes SolidWorks under the NTNU student license. In this project, one of the most important considerations when designing the hydrofoil concept is an emphasis on reducing the production cost; hence, the CAD design will be based on favorable manufacturing methods. Choosing appropriate manufacturing techniques and materials for the individual parts will also be discussed in this stage of the development process. Another important consideration of the physical design is how the parts will be joined together. The structural parts must have a solid connection for the product to deliver maximum performance and be a viable choice comparable to established competitors. The connections between parts are often prone to failure, so it is necessary to make design decisions that ensure that the product maintains its structural integrity under reasonable operational conditions. It is good practice to design the CAD models with a high degree of parameterization so that it is uncomplicated to update and iterate the design if necessary.

The hydrofoil assembly consists of 5 main parts that needs to be designed;

- The front wing
- The rear wing
- The fuselage
- The mast

- The board mount

The last step in the development process is to verify the design concept structurally. The verification will be executed through Finite Element Analysis in Abaqus/CAE. If the structural design is not satisfactory and does not perform sufficiently in terms of strength and stiffness compared to more traditional concepts, then reiterations of the design will be necessary. Ideally, a prototype based on the final design will be created with the proposed manufacturing methods.

1.3.1 Objectives

The main objective of this project is to develop an original and functional hydrofoil design concept that can be brought to market with low initial investment and manufacturing costs per unit. To execute the task, the objectives to be fulfilled are as follows;

Hydrodynamic Design Objectives

- Investigate existing products and identify common key features.
- Identify product requirements for novice riders.
- Study the literature to identify the most important hydrodynamic design parameters regarding hydrofoil design.
- Investigate through the use of the desired software how changing hydrodynamic design parameters influences the dynamic behaviour of the hydrofoil.
- Identify parameter values for a stable hydrofoil design that suits the requirements of novice riders.

Structural Design Objectives

- Create a structural design concept that is favorable for economic manufacturing.
- Propose materials suitable for such a structural concept.
- Verify the design concept and material choices through FEA simulations.
- If necessary reiterate and improve the structural design.
- Create physical prototypes.

Chapter 2

Hydrodynamic Flight

2.1 Introduction

In order to develop a functional hydrofoil design, it is necessary to understand the basic hydrodynamic principles related to wing design. In essence, the hydrofoil assembly used in board sports closely resembles airplanes, and the working principles are essentially the same. In this chapter, the principles of hydrodynamic flight will be investigated. It is desired to explore key concepts related to flight in literature and apply these principles to obtain hydrodynamic parameter values for a functional hydrofoil design. This chapter will primarily be concerned with the design of wings and the parameters related to dynamic stability, focusing on simplistic design favorable for manufacturing. The design parameters will be chosen based on the presumptive needs of a novice rider. However, this chapter's design methodology and processes should apply to the needs of any user segment. In the project, this chapter will provide the first design constraints that need to be considered when the structural aspect of the hydrofoil design is to be developed.

2.2 Hydrofoil Theory

2.2.1 Foil profiles

When foil sections were developed in the early days of aviation, the geometries were largely engineered from empirical experiments with little methodological consideration. This resulted in a large variety of approaches for designing foil sections, with little consistency between them. The National Advisory Committee for Aeronautics in America has devised number-based systems to classify foil sections based on key geometric features that significantly impact the foil's qualities. One of these systems is the NACA 4-digit system, which has been hugely successful and widely used for general-purpose low-speed aircraft worldwide. In this system, the respective digits represent a specific aspect of the foil geometry [5].

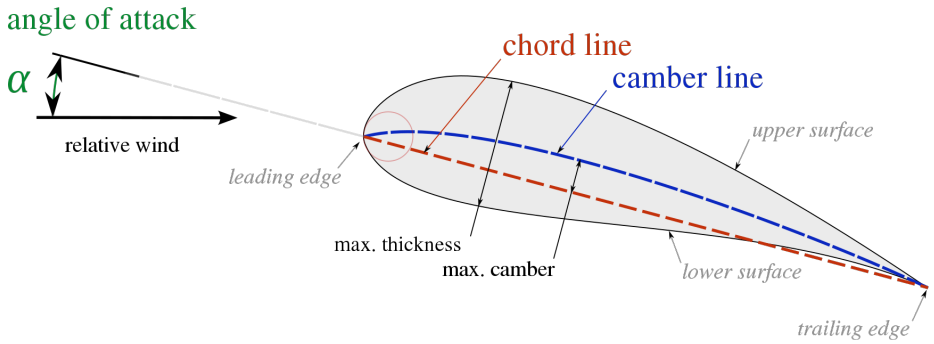

Figure 2.1: Nomenclature of a foil profile [34].

Camber is one of the key parameters that determine the properties of a foil profile. Camber is a term describing the curvature of the centreline, which is the line at an equal distance from the top and bottom surface of the foil. Symmetrical foils hence have no camber of the centreline. Camber is defined by the value of maximum curvature and the location of maximum camber along the chord, normalized as a percentage of the chord length. Camber significantly impacts the stall and drag characteristics of a hydrofoil. In general, foils with maximum camber further forward may experience lower drag but also incorporate poorer stall characteristics due to more abrupt flow separation over the surface. On the contrary, foils with maximum camber further back may experience more gentle stall characteristics [5]. Several classification systems exist, but this project will be limited to the NACA 4-digit series.

- The 1st digit represents the maximum camber given as a percentage of the chord length.
- The 2nd digit represents the distance from the leading edge to the position where the maximum camber is located, given in tenths of the chord length, i.e. 4 equals 0.4 of the chord length.
- The final two digits represent the foil's maximum thickness given as a percentage of the chord length.

For example, an asymmetrical NACA4212 foil with a chord length equal to 100mm, will have maximum camber equal to 4mm located 20mm from the leading edge and a maximum thickness of 12mm. In comparison, the symmetrical NACA0012 foil with a chord length equal to 100mm will have zero camber and hence no location of maximum camber, but the same maximum thickness of 12mm. The thickness distribution is derived from the Clark Y and Gottingen 398 airfoils; hence, all NACA 4-digit foils have their maximum thickness located at approximately x/c = 30% of the chord length [2]. The NACA 4-digit foil profiles are constructed by combining a thickness envelope with a camber or mean line. The equations which describe this procedure are explained in Appendix A.

Experimental results show that the lift, drag and pitching moment of a foil largely depends on the following factors [5];

- The cross-sectional shape of the foil profile
- The plan area S of the foil
- The velocity V squared
- The density ρ of the fluid

Experimental results show that the lift, drag, and pitching moment of a foil largely depends on the following factors [5];

$$Lift = C_L \frac{1}{2} \rho V^2 S \tag{2.1}$$

$$Drag = C_D \frac{1}{2} \rho V^2 S \tag{2.2}$$

$$Pitching\ Moment = C_m \frac{1}{2} \rho V^2 S c \tag{2.3}$$

Regarding the lift and pitching moment, S refers to the plan area of the foil. In the case of drag, S refers to the plan area for a streamlined object such as a foil, but to the projected frontal area for a blunt object. Since a moment vector is defined by the cross product of a force and a distance, c is introduced in the pitching moment equation as the chord length of the foil. The pitching moment is defined as positive when the moment is rotating the leading edge upwards and negative when the moment is rotating the leading edge downwards. The symbols C_L, C_D and C_m are known respectively as the lift coefficient, the drag coefficient and the pitching moment coefficient. The coefficients are dependent on the cross-sectional shape of the foil, and they will also change according to the foil's angle of attack (AoA or α). The angle of attack is defined as the angle between the direction of the relative fluid flow and the chord line of the foil, illustrated in figure 2.1. Another useful characteristic is the lift/drag ratio, which is the relationship between the coefficient of lift and the coefficient of drag. It describes the efficiency of the foil and is defined as [5];

$$Lift/Drag\ ratio = \frac{C_L}{C_D} \tag{2.4}$$

These coefficients are dimensionless and are useful when comparing the characteristics of various foils and wings. The characteristics of foils and wings can be evaluated by plotting the curves of C_L, C_D, C_m and C_L/C_D *ratio* against varying angle of attack or varying velocity from Reynolds number. It is favorable to plot the coefficients rather than the actual forces and moments acting on the foil since the results then will be independent of physical size, fluid density, and fluid velocity [5].

The lift coefficient of a foil profile will increase approximately linearly with increasing AoA until a certain angle where the lift coefficient will start to decrease with further increasing AoA. This is known as the stalling or critical angle of the foil. Through experiments, it has been observed that the cross-sectional shape of different foils seemingly has little effect on the stalling angle. The shape does, however, significantly impact the amount of lift generated at this angle. This critical angle is also relatively unaffected by the relative speed at which the fluid moves past the foil. The loss of lift beyond the critical angle results from flow separation at the top surface of the hydrofoil, which results in vortices forming, making the downstream flow more turbulent. The drag coefficient is least about 0°or at slightly negative AoA. Plotting the drag coefficient against AoA will present a parabolic curve, and the increase in drag is smaller at low AoA than at higher AoA, as illustrated

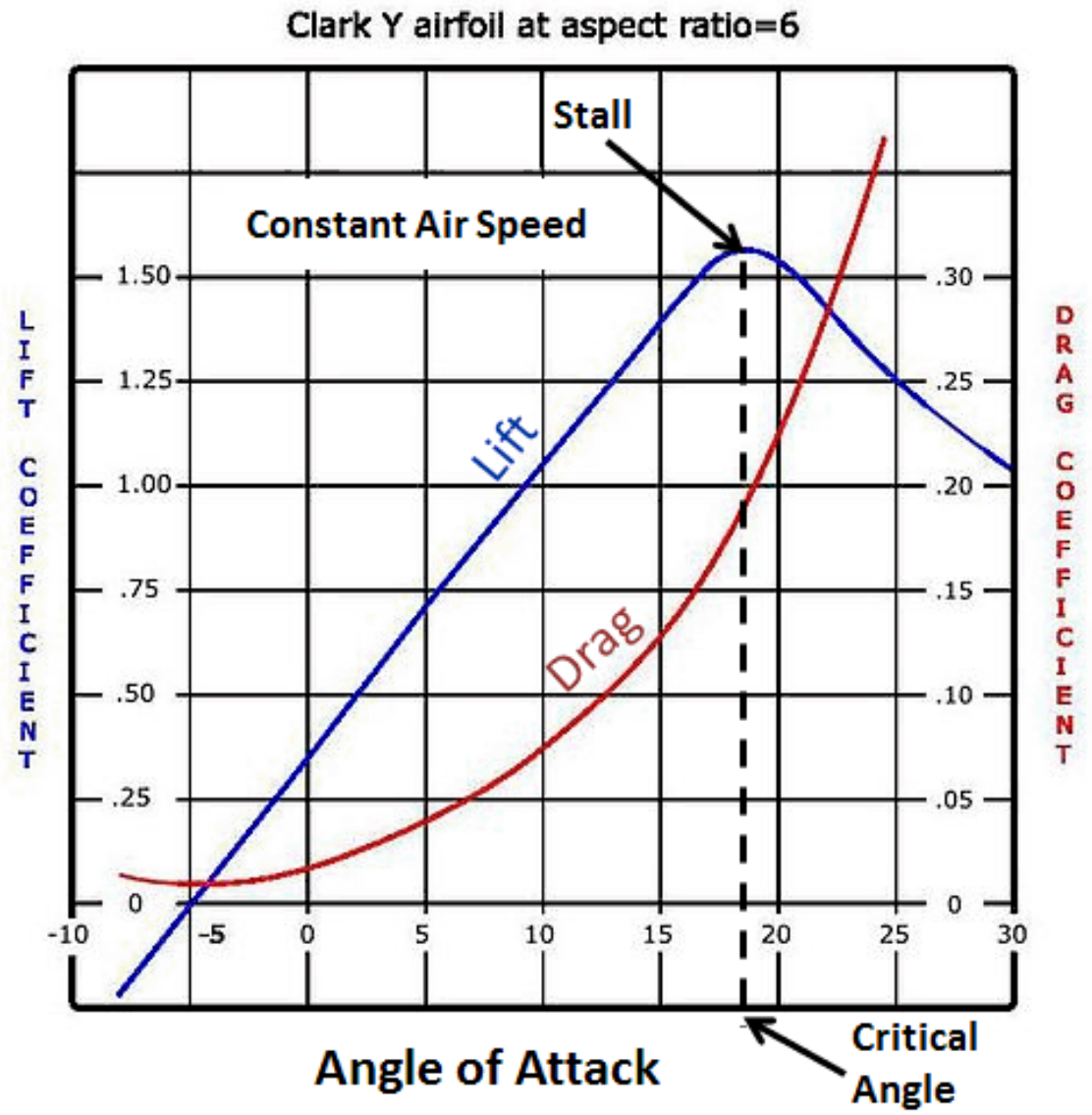

Figure 2.2: Illustration of the lift coefficient and the drag coefficient at different AoA and constant relative fluid velocity for a Clark Y airfoil with AR = 6. The AoA at which stall occurs is known as the critical angle [4].

in figure 2.2. Drag will rapidly increase beyond the critical angle as more abrupt flow separation occurs [5].

For efficient gliding, it is desired that the hydrofoil produces as much lift as possible with as little drag as possible. Since maximum lift and minimal drag are at two extremes of AoA, it is necessary to find a compromise between the two. By plotting the C_L/C_D ratio against AoA, it is possible to find the angle of the wing that produces the most efficient glide. The ratio increases rapidly at low AoA and rounds off about the maximum, at which point the drag increases faster than the lift when further increasing AoA (see figure 2.3). This results in a quite linear drop-off until the stalling angle is achieved [5]. The principal point of interest regarding the lift/drag ratio is to find the AoA at which the ratio is maximized. This AoA is a key design parameter when deciding the Angle of Incidence (AoI, the angle at which a wing is fixed to the fuselage) of the front wing relative to the hydrofoil fuselage.

The pitching moment is affected by both the resultant lift force and the point on the chord length where this force is acting, known as the Centre of Pressure (CoP). When AoA is increased, the

center of pressure moves from the trailing edge of the chord forwards toward the foil's leading edge. When AoA approaches the critical angle, the CoP will gradually move back towards the trailing edge again. The pitching moment coefficient needs to be considered in relation to a reference point. When using the leading edge of a general foil profile as the reference point, there will be a nose-down pitching moment about the leading edge until a certain AoA, and beyond this, AoA a nose-up pitching moment. For a foil profile, the aerodynamic center (also known as the neutral point) is defined as the point on the chord where the pitching moment coefficient is constant and independent of AoA. The position of the neutral point is usually at a distance of about 1/4 of the chord length from the leading edge at sub-sonic speeds (see figure 2.10) [5]. Hence 1/4 is often used as an approximation in equations.

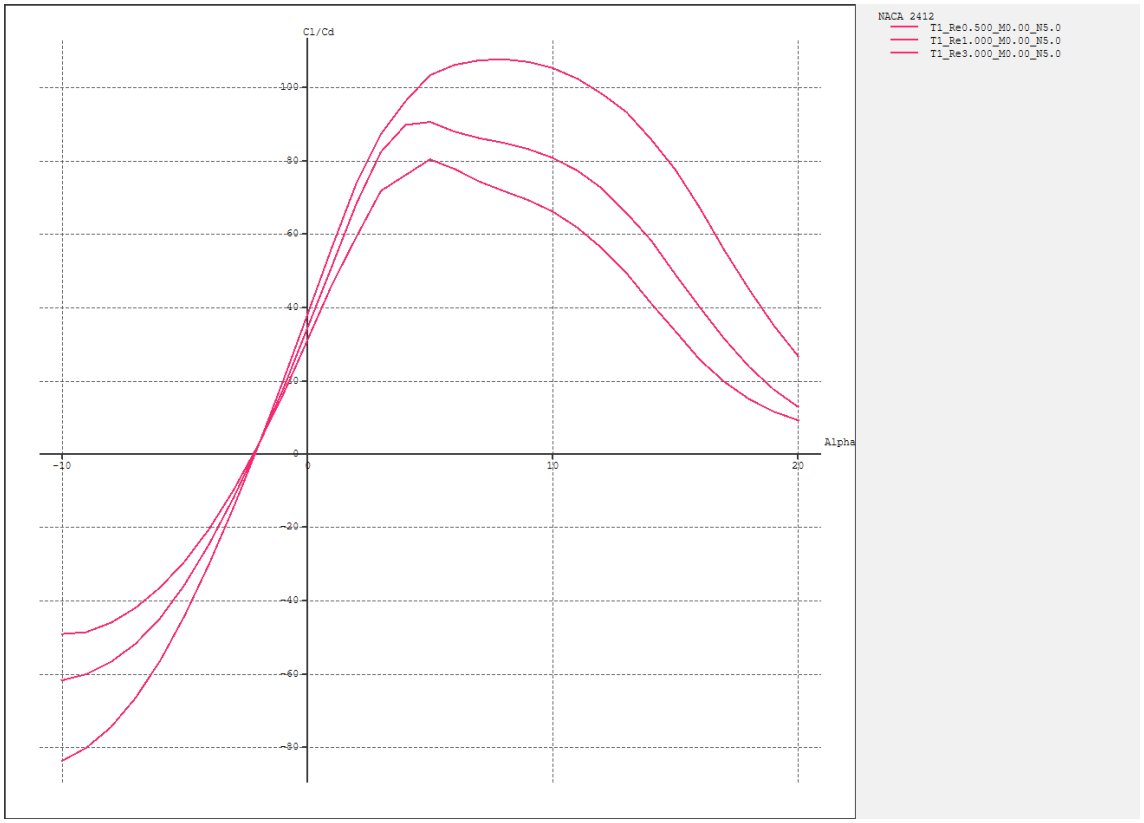

Figure 2.3: The C_L/C_D *ratio* ratio at different AoA for the NACA2412 foil profile for $Re = 500000$, $Re = 1000000$ and $Re = 3000000$. The graphs where produced in Xflr5.

Choosing a foil profile is all about making compromises. Improving one aspect of a foil design will tend to compromise another aspect. For example, reducing the drag coefficient to achieve higher top speed will tend to also decrease the lift coefficient for lower speeds. Hence, when designing a hydrofoil setup, it is necessary to optimize the setup for a given application, desired cruising speed and handling behaviour. An ideal foil profile would have the following properties;

1. A high maximum coefficient of lift so the hydrofoil will be able to maintain lift at slow speed.
2. A low coefficient of drag about AoA = 0° so the hydrofoil is able to reach a high top speed at cruise trim.
3. A high maximum lift/drag ratio for low resistance to motion and high efficiency.

2.2.2 Finite Wings

The finite wing plan form is the other major factor that dictates the behavior of hydrofoils. Until now, only the two-dimensional cross-section of foils has been considered. In such a 2D model, the lift, drag, and moment generated by a given foil should be proportional to increasing plan area and independent of plan form. However, experimental observations have shown that this is not the case for finite three-dimensional wings [5]. The aspect ratio (AR) is the relationship between the span and the chord of a wing, and is defined as;

$$AR = \frac{b}{c} \tag{2.5}$$

for a rectangular wing, or;

$$AR = \frac{b^2}{S} \tag{2.6}$$

for a wing with arbitrary plan form [13]. Where b is the span of the wing, c is the chord length and S is the wing plan area.

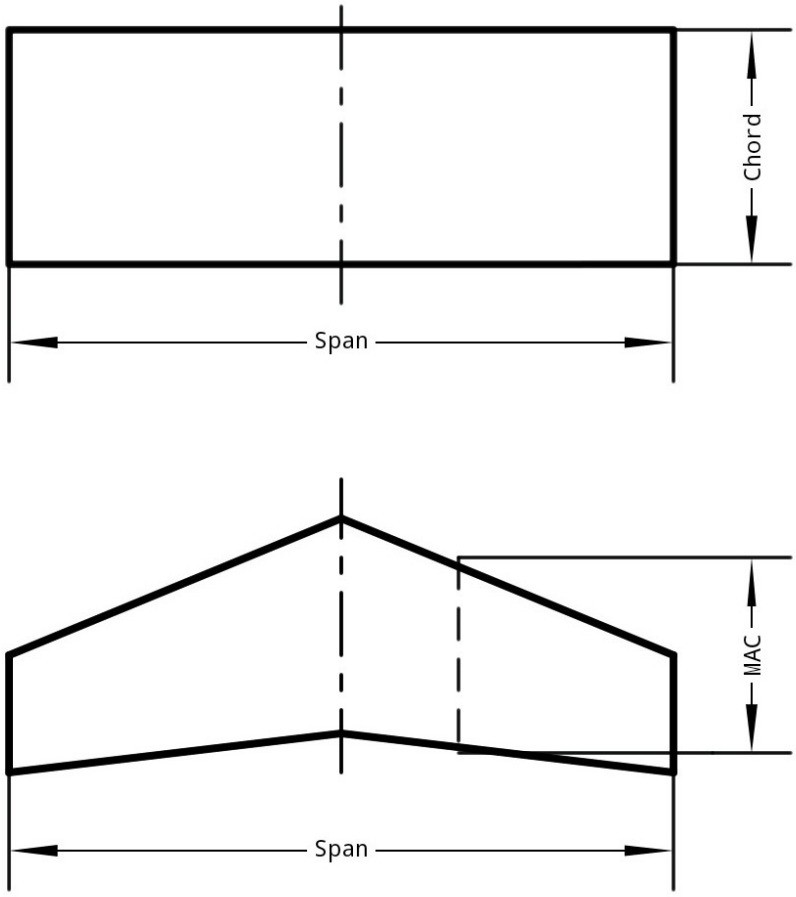

Figure 2.4: Nomenclature of a wing with rectangular plan form and a wing with swept plan form.

Based on the equations for foil profiles (see equation 2.1, 2.2), two wings of equal foil profile and plan area, but with different aspect ratios, should produce the same lift and drag. This is because the forces are proportional to the area. However, experiments show that this foil theory is not entirely applicable to finite wings. Generally, a high aspect ratio wing will generate more lift at any given AoA and have a greater maximum C_L/C_D ratio than a low aspect wing. It will also

have a greater moment of inertia, which makes it more roll stable. On the other hand, a low aspect ratio wing will experience stall at a higher AoA and hence maintain lift at a lower speed while also having greater maneuverability. The angle of no lift is however unaffected [5].

The main reason for the increased lift/drag ratio of a high aspect ratio wing is due to the pressure difference between the top and bottom surfaces of the wing. The ambient pressure outside the wingtips is greater than the pressure over the wing, resulting in an inward fluid flow at the upper side of the wing. On the bottom side, the pressure is greater than outside the wingtips, which results in an outward fluid flow. Hence, the fluid spills around the wingtips, from the bottom to the top surface. This spilling is not effective at providing lift, and since a high aspect wing has a shorter chord, a smaller proportion of fluid spills around the wingtips. Due to this tip effect, the direction of the flow on the top and bottom sides of the wing will be angled relative to the wing's chord line. The resulting flow on the top side of the wing will be angled inward toward the fuselage and angled outward toward the tips at the bottom side. Hence the flow over the top surface and under the bottom surface of the wing will meet at an angle at the trailing edge, and vortices with a downward directional component will be formed. This is known as induced downwash. Due to the fluid's momentum change in this vortex sheet at the trailing edge, the resultant force vector will be tilted backward, causing induced drag. This effect will be more profound on a low-aspect wing since the wingtips are closer together. The induced drag is given by the following formula [5], [13];

$$D_i = (\frac{C_L^2}{\pi AR})\frac{1}{2}\rho V^2 S \tag{2.7}$$

The other major drag component related to subsonic speeds is known as parasitic drag, which encompasses the drag related to the resistance of motion due to the shear friction the fluid exerts on the wing surfaces and the pressure on the projected frontal area of the wing. The induced drag will decrease with an increase in relative fluid flow, while the parasitic drag will increase (see figure 2.5). In aviation, it is essential to minimize the total drag as drag directly correlates with increased fuel consumption. Regarding hydrofoils in kiteboarding, the wind is the power source, and drag should instead be viewed from a top speed-limiting perspective.

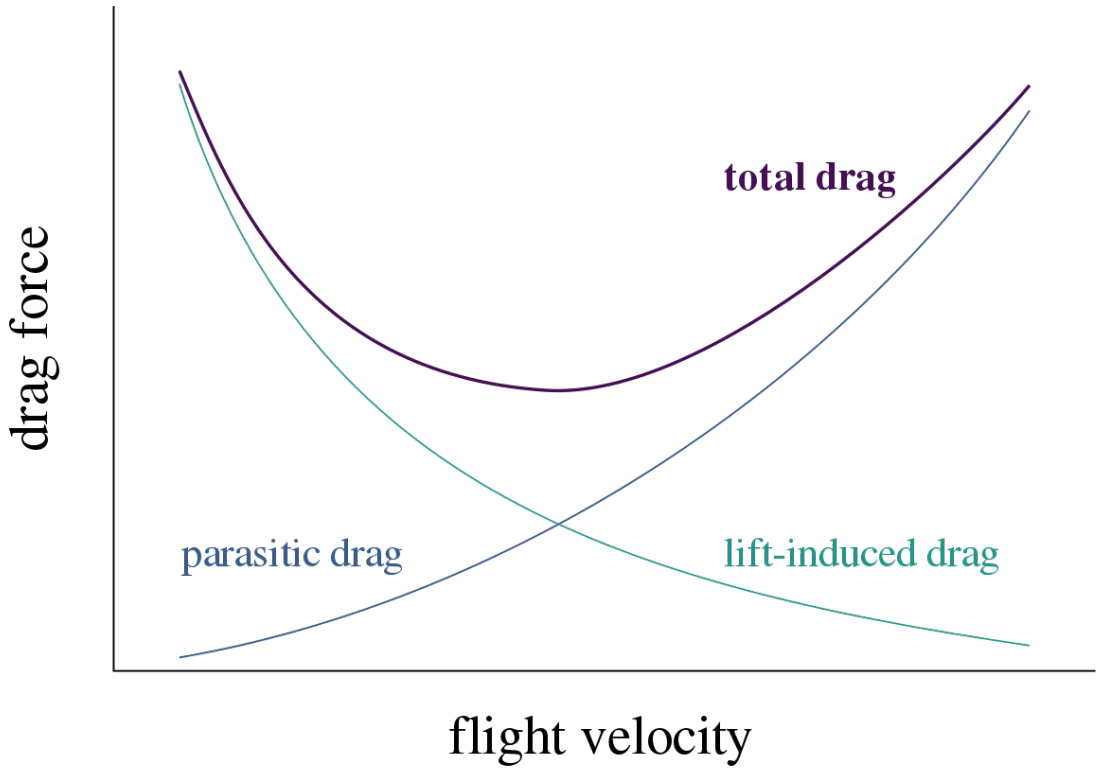

Figure 2.5: Illustration of the relationship between drag forces and flight velocity at constant AoA [38].

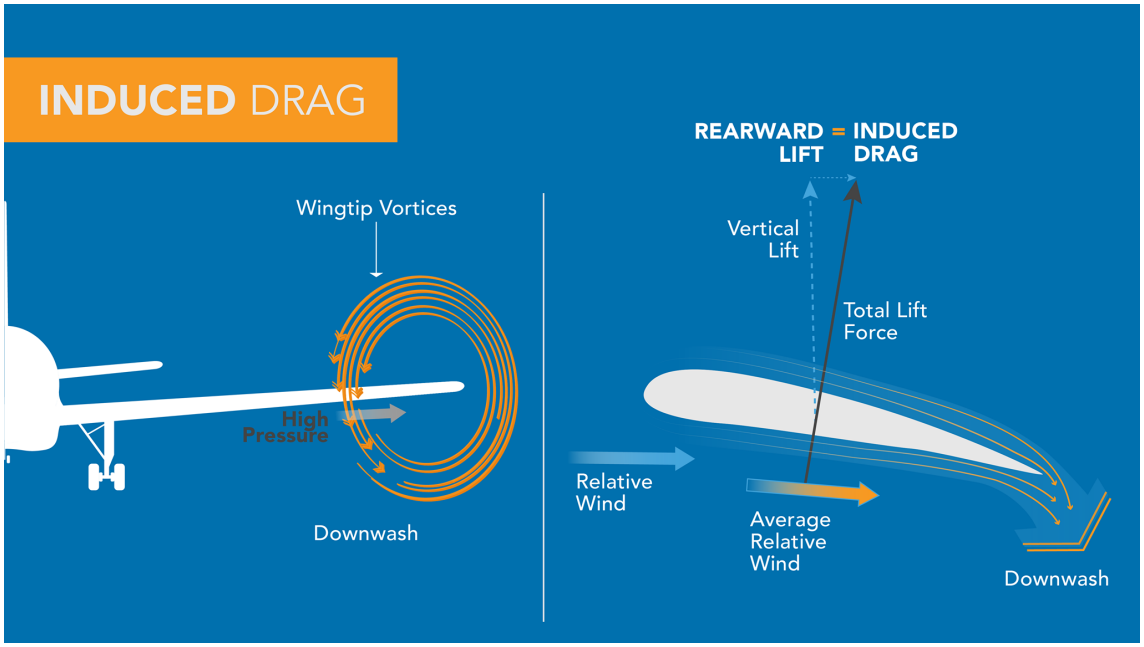

Figure 2.6: Illustration of the wingtip vortex of a airplane wing (left) and the induced downwash (right) [33].

2.2.3 Hydrofoil Dynamics

A hydrofoil has the ability to maintain leveled flight over a whole speed range. This range starts at the minimum speed at which the hydrofoil is able to generate enough lift to counter the force of gravity and up to the maximum attainable speed. A hydrofoil will need to be gliding at respective angles of attack depending on the speed to maintain leveled glide. This relationship can be explained using the lift formula explained earlier.

$$L = C_L \frac{1}{2} \rho V^2 S$$

Here we assume that the fluid is incompressible and hence that the density is constant. The wing area is also constant. Since the distance between the top and bottom surface of the wings are small, and the depth is no deeper than 1m, we choose to neglect the difference in the depth-dependent static water column pressure. Since the lift force shall be constant and equal to the force of gravity at any time, the parameters that can be adjusted are the lift coefficient C_L and the speed V. This means that if the speed increases the angle of attack needs to be reduced to maintain constant lift and have no motion in the vertical direction. Since C_L increases with AoA until the stall angle, the pitch attitude of the hydrofoil needs to be reduced [5]. Therefore every speed corresponds with a specific AoA for the respective weight of a rider. This fact also implies that the hydrofoil needs to be designed with a specific cruise speed and rider weight in mind for optimal performance, where the board will be parallel with the surface of the water.

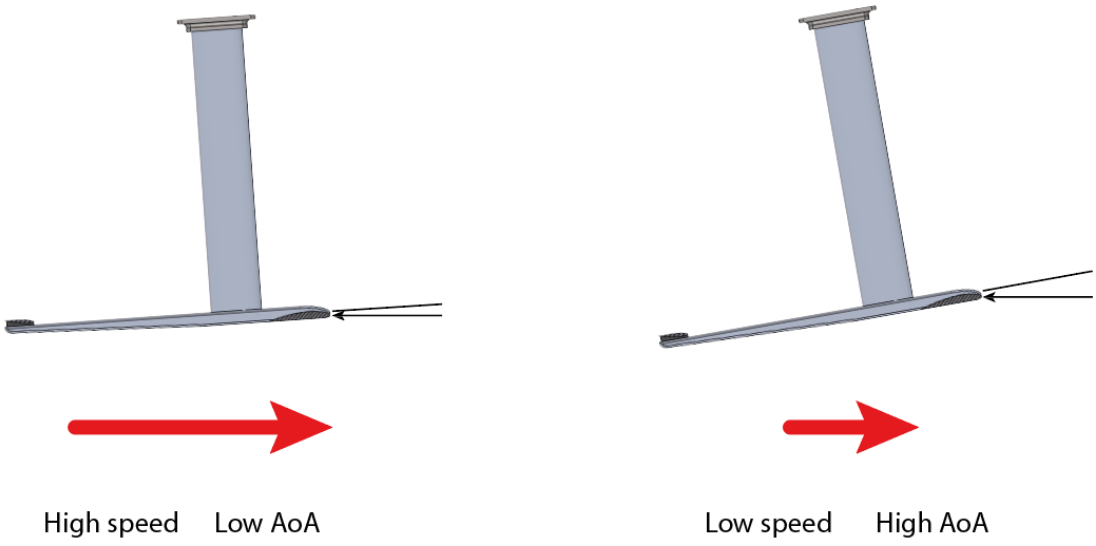

Figure 2.7: An illustration of the relationship between velocity and AoA at constant lift.

A hydrofoil must, to some extent, exhibit self-stabilizing behavior to be controllable. Optimizing the stability characteristics of a hydrofoil is a rather complex process, but some key criteria involving fundamental geometry should be evaluated in the design process. By convention, the longitudinal locations (in the x-direction) of geometric features are expressed relative to the leading edge of the front wing's mean aerodynamic cord (MAC). By this convention, aft is the positive direction, and forward is the negative direction. l_h denotes the distance between the center of gravity and the 1/4 cord location of the rear wing. This length represents the moment arm of the stabilizing rear wing about the CG. In the same way, l_v represents the the moment arm but in relation to the mast [37].

There are two main factors to consider regarding the pitch stability of the hydrofoil. Firstly, the size and longitudinal placement of the rear wing relative to the front wing, and secondly, the

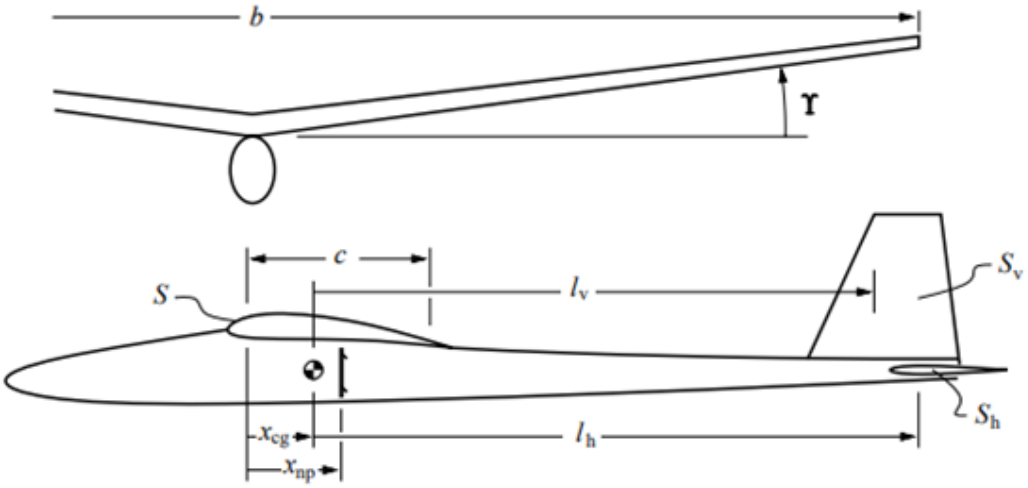

Figure 2.8: An illustration of an aircraft showing stability-related nomenclature [37].

placement of the CG. Pitch stability refers to the hydrofoil's ability to return to the original angle of attack and speed when subject to pitch disturbances. For hydrofoils used in water sports, there are no flaps or control surfaces on the rear wing to control the attitude of the hydrofoil. Instead, the pitch of the hydrofoil is controlled by the rider shifting the CG either forward or aft. Since the mass of the hydrofoil is small relative to the mass of the rider, the CG of the total system is approximately located at the CG of the rider [37].

At a specific CG position, the pitch stability of the system will be neutral; this position is referred to as the neutral point (NP). The position of the CG relative to the NP determines the stability about the pitch axis. This distance is referred to as the static margin (SM) and is an important design parameter when deciding the dynamic behavior of the hydrofoil. If SM = 0, then the resulting moment the hydrofoil experiences will be constant regardless of AoA [37].

$$SM = \frac{x_{np} - x_{cg}}{MAC} \tag{2.8}$$

Where x_{np} is the longitudinal position of the neutral point and x_{cg} is the longitudinal position of the centre of gravity. The value is normalized by dividing by the mean aerodynamic chord (MAC). A rear wing that produces more lift or has a longer moment arm relative to the front wing's center of pressure will cause the NP to be located further aft on the hydrofoil.

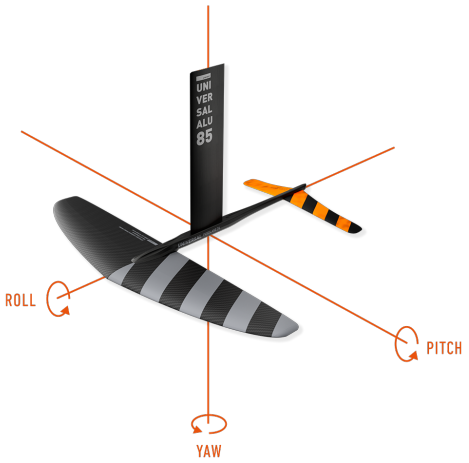

Figure 2.9: A RRD hydrofoil showing the axial directions of rotation [22].

The effectiveness of the rear wing is expressed with the horizontal tail volume coefficient V_h [37].

$$V_h = \frac{S_h l_h}{MACS} \tag{2.9}$$

Where S_h is the plan area of the rear wing and l_h is the moment arm. A lower tail volume coefficient will cause the pitch behavior of the hydrofoil to be more sensitive to CG location changes, making precise control more difficult. The hydrofoil will also be more susceptible to deviation from the desired pitch attitude. The longitudinal location of the NP can be estimated with the following equation and is directly influenced by V_h [37].

$$\frac{x_{np}}{MAC} = \frac{1}{4} + \frac{(1 + \frac{2}{AR})}{(1 + \frac{2}{AR_h})}(1 - \frac{4}{AR + 2})V_h \tag{2.10}$$

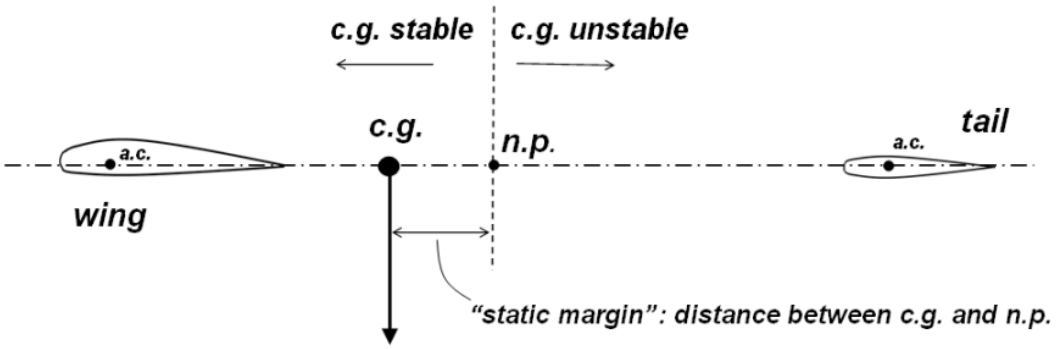

Figure 2.10: Illustration of static margin in relation to pitch stability [15].

When x_{cg} is forward of x_{np}, the static margin will be positive, and the hydrofoil will experience stable behaviour. On the other hand, when x_{cg} is aft of x_{np}, the static margin will be negative, and the hydrofoil will experience unstable behaviour. When a stable hydrofoil experiences a pitch disturbance, it will naturally return to its original attitude, while an unstable hydrofoil will reinforce the disturbance, requires constant active input, and hence is inherently difficult to control. A strongly positive SM will provide more pitch stability, but not without drawbacks. One of the undesirable effects is that there is a greater need for pitch trim when changing speed. In other words, an increase in speed will cause the hydrofoil to pitch up [37]. The pitch change needs to be countered by adjusting the trim, in this case by the rider moving the CG, causing the hydrofoil to return to leveled operation. Failure to react in time may cause the hydrofoil to breach the water's surface and risk injury to others or the rider himself. When designing the hydrofoil, it is necessary to find a compromise regarding stability and responsiveness.

The angle the wings make with the horizontal plane is known as the dihedral angle. If this angle is such that the wing tips are pointing upward, it is known as dihedral, while when pointing downward known as anhedral. The purpose of the dihedral/anhedral is to aid in lateral stability. A spirally unstable craft will naturally increase bank angle when rolling and hence requires control input by the rider. Conversely, a spirally stable craft will naturally return to an upright attitude when the rider is not giving any control input and hence is easier to control. The parameter B is commonly used to determine the spiral stability of a craft and is expressed with the following equation [37];

$$B = \frac{l_v \gamma}{b C_L} \tag{2.11}$$

When the parameter value is greater than B = 5, the hydrofoil is spirally stable and conversely spirally unstable when the value is less than B = 5. When designing for spiral stability, the dihedral angle γ is the common parameter to adjust in this equation. Spiral stability is not necessarily a hard requirement given that the instability is slow [37].

Yaw stability is another form of lateral stability and is controlled by a vertical tail. In most hydrofoil designs, the mast alone serves this function. The effectiveness is expressed by vertical tail volume coefficient V_v [37];

$$V_v = \frac{S_v l_h}{MACS} \tag{2.12}$$

Roll and yaw can also occur in unison in a stability mode known as dutch roll.

2.3 Method - Exploring Hydrodynamic Design Parameters

2.3.1 Xflr5 Analysis Method

Xflr5 is a modeling and simulation software originally intended for designing model sailplanes. Despite its intended purpose, the software has gained popularity for designing low Reynolds number crafts of various applications ranging from flying wing drones to hydrofoils. The primary purpose of Xflr5's development was to provide a user-friendly graphical user interface (GUI) based on the code of the already well-established software Xfoil. While Xfoil is based solely on simulations of 2D foil profiles, Xflr5 expanded the capabilities by adding 3D modeling and simulations. The algorithms for foil analysis are exactly the same as in Xfoil but translated from FORTRAN to C/C++. The source code is provided for use by everyone under the GNU General Public License rules. The modeling of finite wings, fins, and fuselages uses a 3D panel method, and the simulations are based on Non-linear Lifting Line Theory (LLT), as well as the Vortex Lattice Method (VLM) for designs with geometries that otherwise would be limited by LLT approximation [39].

Xflr5 offers four modules to aid in the design process. Direct Foil Design for comparing the geometry of standard foil profiles or designing custom foil profiles using B-splines. Inverse Design for modifying the geometry of a foil profile by graphically changing the velocity envelope along the cord length of the foil. Direct Analysis for plotting the polars of the foil profiles graphically to analyze and compare their fluid dynamic behavior. Wing and Plane Design for plotting the polars of finite wings and 3D geometries graphically to analyze and compare their fluid dynamic behavior. This last module also has the ability to conduct stability analysis, where longitudinal and lateral stability modes can be represented graphically in complex root loci plots and through time response plots. Although the functionalities in Xflr5 are rather comprehensive, the software is not intended for designing manned aircraft [39]. However, regarding recreational hydrofoils, the risks involved are substantially lower than for aircraft; Xflr5 is hence deemed as suitable analysis software for the application.

Some presumptions are made in order to conduct the analysis:

1. For the sake of this analysis, the model will be based on the rider and board as one system with a point mass of 75kg and with the height of the rider being 180cm. The vertical position of the CG of the system will vary while riding, so it is assumed that the average position is at 50% of the body height, and the mast height will be 700mm.

2. The masses of the parts are estimated based on typical values from top brands and will not necessarily represent the final design masses. Front wing = 900g; Rear wing = 100g; Fuselage = 700g; Mast = 2200g.

3. The design will be based on the product requirements suited for an inexperienced rider; ease of use, optimized for lift at slower speeds, early aquaplaning, and stability. These requirements are largely the opposite of a design for experienced or competitive riders that would favor a design optimization tailored for lift at higher speeds, low drag, and quick maneuverability.

4. The design will focus on simple geometries assumed convenient and cost-effective for manufacturing. Hence, the wing planforms will be rectangular, and the foil profiles will be constant along the span of the wings with no twist or dihedral.

5. In the Xflr5 documentation, it is not recommended to model the fuselage, as the intersection between the surfaces of different parts can limit the robustness of the results. Hence, the hydrodynamic effects of fuselage geometry will not be a part of this analysis. Fuselage mass will be included, but the hydrodynamic influences cannot be evaluated.

Since there is an almost endless variety of different foil profiles available, this study will be limited to four profiles from the NACA 4-digit series that have been widely used and studied in relation to low-speed aircraft. These foils are the NACA2412 and NACA4412 as an alternative for the front wing, and the symmetrical NACA0009 and NACA0012 as an alternative for the rear wing. The shape of the NACA4412 profile is highly similar to the historic general purpose Clark Y aerofoil, one of the foils on which the thickness distribution of the NACA 4-digit system has been based. The NACA2412 is best known for its use on several of the general-purpose Cessna aircraft. $C_L/C_D - \alpha$ plots of these foil profiles are given in table 2.11.

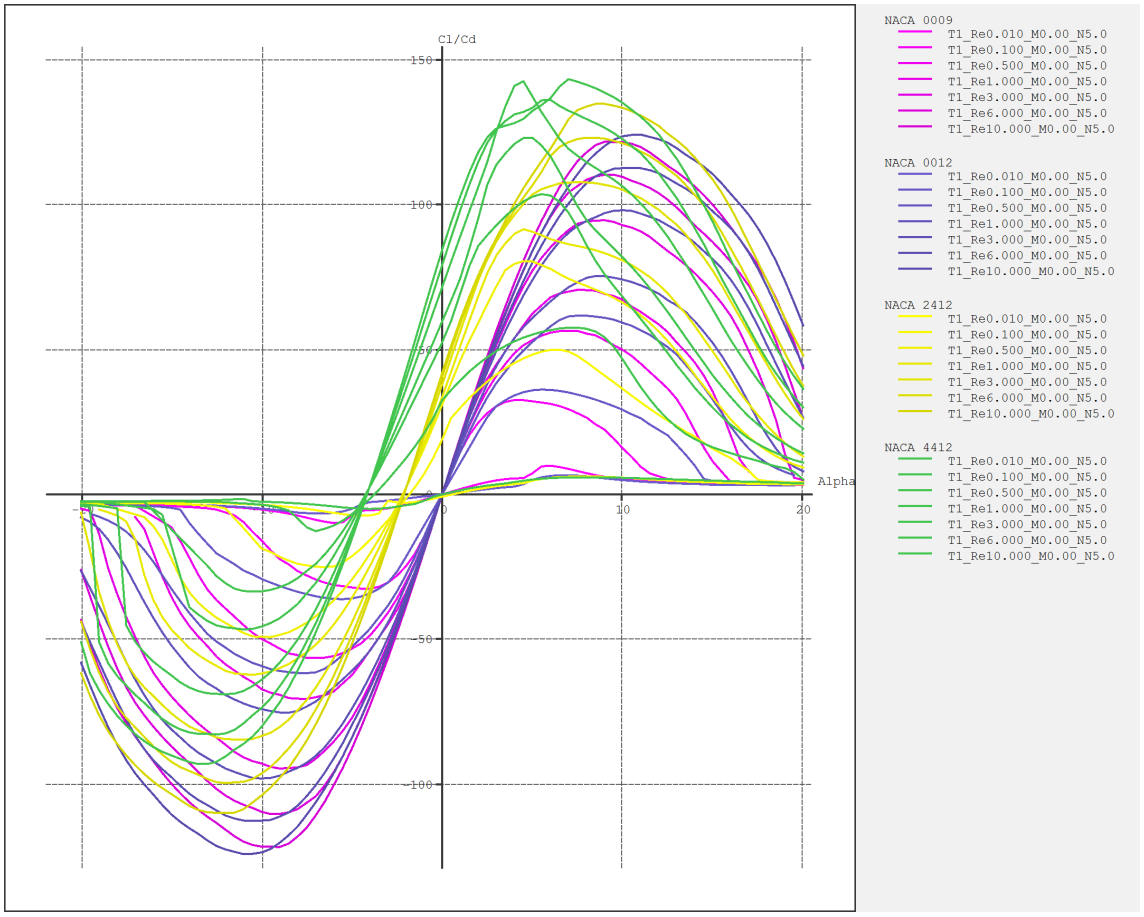

Figure 2.11: $C_L/C_D - \alpha$ plots of the NACA0009 (pink), NACA0012 (purple), NACA2412 (yellow), and NACA4412 (green) foil profiles at Reynolds numbers from $Re = 10000$ to $Re = 10000000$.

When comparing the NACA4412 and NACA2412 foil profiles, it is observable that the NACA4412 produces more lift than the NACA2412 at lower AoA. The angle of zero lift is also less than for the NACA2412. However, the NACA2412 exhibits more symmetrical behavior due to having less maximum camber. The NACA4412 seems to have a rounder and gentler stall behavior, while the NACA2412 seems to have a more consistent Cl/Cd ratio at $Re > 1.0e06$, suggesting that it is more suited for higher speeds than the NACA4412. Between these two candidates, the NACA4412 foil is deemed the better alternative for the application. Regarding the rear wing, the only physical difference between the profiles is the maximum thickness. This results in a compromise where opting for more rear lift comes at the expense of increasing drag. The NACA0012, in addition to providing more lift, also provides lift over a more extensive AoA range, while the NACA009 offers less drag. NACA0012 is hence favorable in terms of ease of use, and a thicker profile is also easier to manufacture. The NACA0012 profile is therefore decided to be used as the rear wing.

An experiment was conducted to understand how to tune the design parameters to achieve a functional design. It was executed by varying each respective design parameter while keeping the others constant. The objective of this experiment was to be able to graphically visualize each parameter's polar impact on the hydrodynamic behavior of the hydrofoil and then summarize the findings to aid in optimizing the design. When the desired hydrofoil response is known, the resulting table can be referenced to identify how each parameter needs to be tuned to obtain the desired behavior. The results should be in accordance with the theory described in the literature. The investigation was conducted with the following method;

In the following sections, it is important to be aware of the difference between Angle of Attack (AoA) and Angle of Incidence (AoI), as these terms are used frequently. In this section, AoA refers to the angle of the complete hydrofoil with respect to the relative fluid flow, while AoI refers to the angle at which a wing is fixed to the fuselage.

1. Make an initial model based on parameters known from other brands that will serve as a baseline model for reference in the experiment.
2. Keep all parameters as baseline and only increase the front wing AoI from 0°to 3°to 6°.
3. Keep all parameters as baseline and only decrease the rear wing AoI from 0°to -3°to -6°.
4. Keep all parameters as baseline and only increase the front wing area by a scaling factor of 1.25 and 1.5 while maintaining the aspect ratio.
5. Keep all parameters as baseline and only increase the rear wing area by a scaling factor of 1.25 and 1.5 while maintaining the aspect ratio.
6. Keep all parameters as baseline and only increase the front wing aspect ratio to 6.75 and 9 while maintaining the plan area.
7. Keep all parameters as baseline and only increase rear wing aspect ratio to 8 and 10 while maintaining the plan area.
8. Keep all parameters as baseline and only increase the fuselage length from 600mm to 700mm to 800mm, effectively increasing the moment arm of the rear wing.
9. Keep all parameters as baseline and only move the CG in the longitudinal x-direction from 0 to -100mm to -200mm.
10. Keep all parameters as baseline and only move the CG in the vertical z-direction from 1630mm to 1000mm to 500mm to 0mm

The baseline model will be based on wing sizes, fuselage length, and mast length that are in accordance with early hydroplaning and lift at relatively low speed. Regarding the front wing, the span is decided to be 680mm and the chord length to be 150mm. Using a simple rectangular plan form, this equates to an area of $1020cm^2$ and an aspect ratio of 4.53. By convention, the leading edge of the front wing is referenced to x = 0, where aft will be the positive x-direction, and forward is the negative x-direction. Regarding the rear wing, the span is decided to be 360mm and the chord length to be 70mm. Using a simple rectangular plan form, this equates to an area of $252cm^2$ and an aspect ratio of 5.14. The mast length is decided to be 700mm as this is in the recommended size range for progressing beginners. The distance between the front wing's leading edge and the rear wing's leading edge is set to 600mm for the baseline model. This baseline model will be used as the reference and will have the light green curve in all of the following plots.

Xflr5 has several analysis options for 3D models. In this study, the "Type 2 (fixed lift)" analysis is the most relevant. When conducting this type of analysis, the total lift force is equal to the weight of the total hydrofoil and rider system. The analysis of the model cycles through a specified range of AoA and the corresponding hydrodynamic coefficients and necessary velocities to maintain equilibrium for each respective AoA is obtained. This analysis is dependent on the Reynolds number of the fluid, which is expressed as follows;

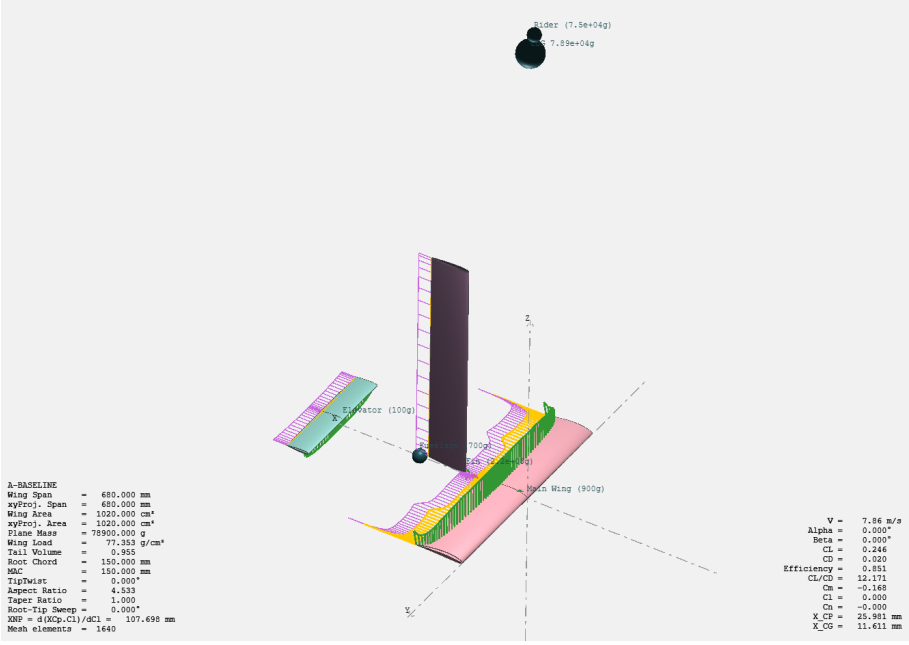

Figure 2.12: The baseline model defined in Xflr5 to be used as the reference in the experiment. The green, yellow and pink regions illustrate the distribution and magnitude of the lift, parasitic drag, and induced drag, respectively, at AoA = 0. The largest sphere at the top of the figure represents the location of the CG.

$$Re = \frac{\rho V l}{\mu} = \frac{V l}{\nu} \tag{2.13}$$

When setting up the analysis, the properties of the fluid need to be defined. In this analysis a water temperature of 20°is assumed, which has a corresponding fluid density of $998.2 kg/m^3$ and a kinematic viscosity of $1.0 \times 10^{-6} m^2/s$ from values provided by IAPWS [7].

The most essential plot when defining the parameters for a functional hydrofoil design is the $C_m - \alpha$ plot. With this plot, it can be visualized at which attitudes the hydrofoil will maintain pitch stability, if any stability at all. It is required that the slope of the $C_m - \alpha$ curve is negative to achieve stability, and a steeper slope implies a more stable design. The AoA at the point where the curve crosses the $C_m = 0$ line is known as the zero-moment angle. At this pitch angle, the forces will be in equilibrium, and the hydrofoil experiences no moment about the center of gravity. It is desirable that the zero-moment angle is close to zero so that the board will be parallel with the water and experience a restoring moment about this angle when disturbed. C_m is defined so that a positive value corresponds with a moment that pitches the nose of the hydrofoil up, while a negative value corresponds with a moment that pitches the nose down, as described earlier.

The $C_m - \alpha$ plot is complemented with the $C_m - V$ plot. It was earlier described how leveled glide is obtained when lift equals weight and that this occurs at different velocities for respective AoA. This implies that the zero-moment angle corresponds to a specific speed, which will then be the design cruise speed. It is necessary that the cruise speed is compatible with the product requirements and the needs of the end user.

Another important plot is the $C_L/C_D - \alpha$ plot. From this plot, it can be determined at which AoA the hydrofoil will experience the most lift while being the least compromised by drag, and hence is the most efficient. Ideally, the maximum lift/drag ratio would coincide with a zero-moment angle of AoA = 0, but compromises need to be made. The $C_L/C_D - \alpha$ plot is complemented by the $C_L/C_D - V$ plot where the corresponding velocity for a respective lift/drag ratio can be found.

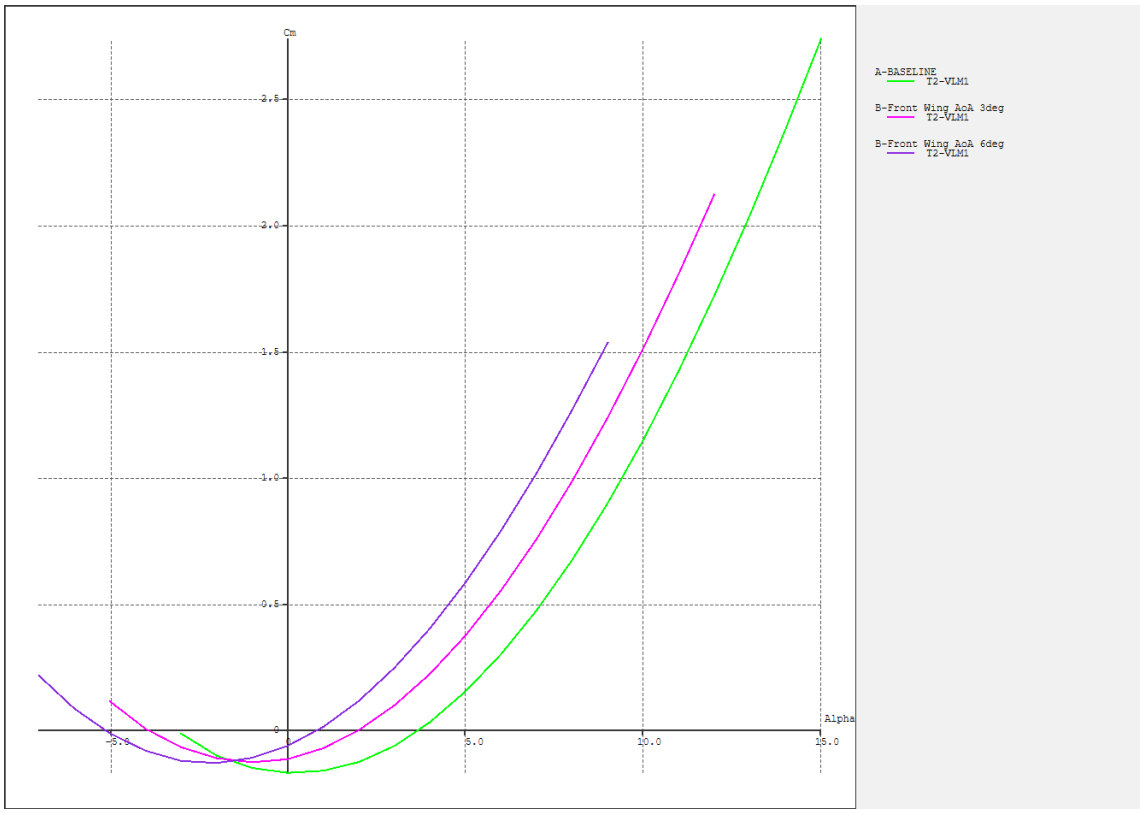

Figure 2.13: The $C_m - \alpha$ plot showing the effect of varying the front wing angle of incidence at constant lift.

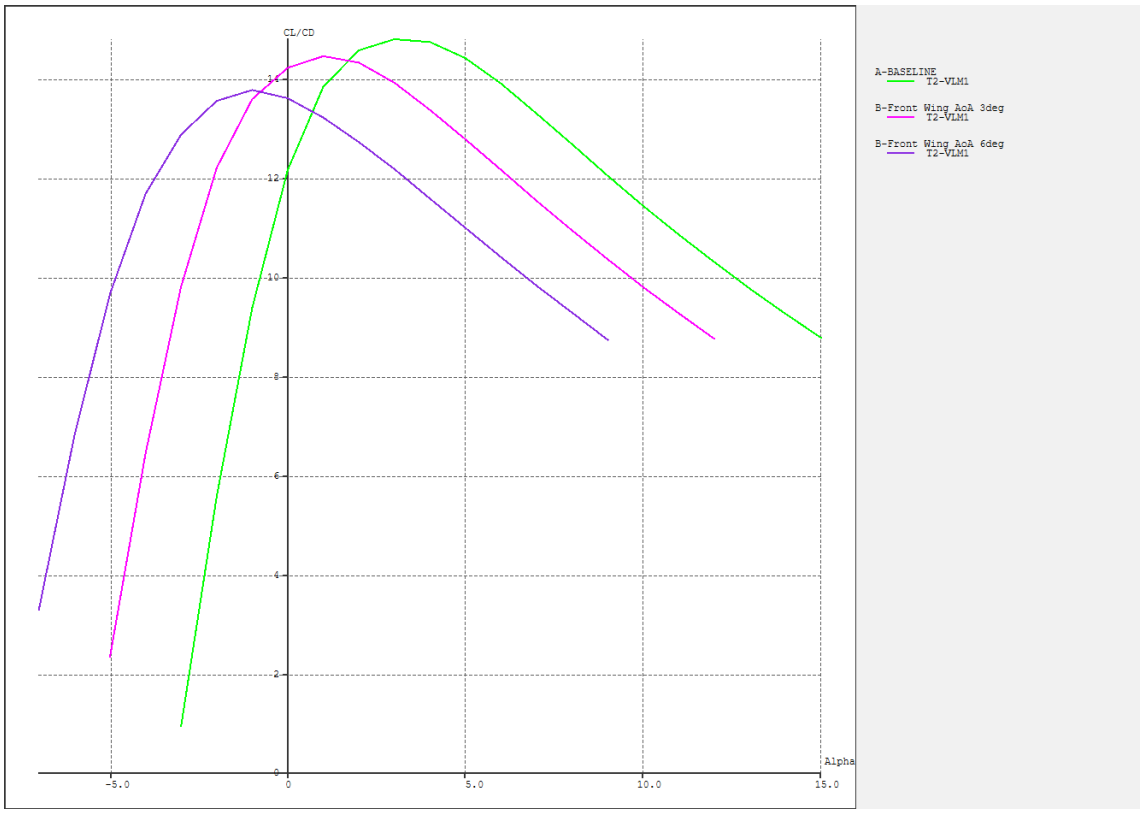

Figure 2.14: The $C_L/C_D - \alpha$ plot showing the effect of varying the front wing angle of incidence at constant lift.

2.4 Hydrodynamic Results and Discussion

2.4.1 Design Parameter Relevance and Function

$C_m - \alpha$ and $C_L/C_D - \alpha$ plots where produced from the Xflr5 simulations to show graphically the effect of changing the design parameters. The plots were analyzed and the key effects of changing each parameter has been summarized in table 2.1 and table 2.2. These tables will be consulted on how the parameters needs to be changed to achieve a final optimized design. The respective plots for each individual parameter is found in Appendix B and Appendix C.

Table 2.1: The effect of varying hydrodynamic design parameters on the $C_m - \alpha$ relationship.

Parameter change	Visual effect on the $C_m - \alpha$ plot	Practical effect
Increase front wing AoI	The curve is shifted to the left.	The zero-moment angle is achieved at a lower AoA.
Decrease rear wing AoI	The curve is shifted up and to the right.	The zero-moment angle is achieved at higher AoA.
Increase front wing area	The curve becomes less parabolic.	The hydrofoil becomes less stable. The zero-moment angle is achieved at lower AoA. The range of stability expands.
Increase rear wing area	The curve is shifted up and to the right.	The zero-moment angle is achieved at higher AoA.
Increase front wing AR	The curve becomes more parabolic.	The hydrofoil becomes more stable. The zero-moment angle is achieved at higher AoA. The range of stability narrows.
Increase rear wing AR	The curve is slightly shifted up and to the right.	The zero-moment angle is achieved at higher AoA.
Increase fuselage length	The curve is slightly shifted up and to the right.	The zero-moment angle is achieved at higher AoA.
Move CG forward	The curve is shifted down and to the right.	The range of pitch stability is increased. More responsive counter moment. The AoA of zero moment remains the same.
Move CG lower	The curve becomes more linear.	The moment about the zero-moment angle changes more linearly with respect to AoA.

Table 2.2: The effect of varying hydrodynamic design parameters on the $C_L/C_D - \alpha$ relationship.

Parameter change	Visual effect on the $C_L/C_D - \alpha$ plot	Practical effect
Increase front wing AoI	The curve is shifted to the left and the maximum is lower.	The maximum lift/drag ratio is lower and is achieved at lower AoA. The no lift angles appear at lower AoA.
Decrease rear wing AoI	The curve is shifted to the right and the peak is lower	The maximum lift/drag ratio is lower and is achieved at higher AoA. The no lift angles appear at higher AoA.
Increase front wing area	The curve is shifted to the left and the peak is higher.	The maximum lift/drag ratio is higher and is achieved at lower AoA.
Increase rear wing area	The curve is shifted to the right and the peak is lower.	The maximum lift/drag ratio is lower and is achieved at higher AoA. The AoA range of lift narrows.
Increase front wing AR	The peak is higher. The right side of the curve cuts at higher AoA.	The lift/drag ratio is increased for all AoA. Stall is experienced at lower AoA.
Increase rear wing AR	The curve is shifted down. The left side of the curve cuts at lower AoA.	The lift/drag ratio is decreased for all AoA. The angle of zero-lift is lower.
Increase fuselage length	Approximately no effect.	The lift/drag ratio remains the same.
Move CG forward	No effect. The lift/drag ratio remains the same	The lift/drag ratio remains the same.
Move CG lower	Approximately no effect.	The lift/drag ratio remains the same.

2.4.2 Discussion of the Hydrodynamic Design Parameters

An interesting finding from this experiment is that the curves in the $C_m - \alpha$ plot are of parabolic nature. This is apparently due to the elevated center of gravity, away from the axis where the neutral point and center of pressure are found. This shows a fundamental difference between the pitch stability of hydrofoils in water sports and the pitch stability of airplanes. For airplanes, the CG is close to the axis of CoP and hence has an approximately linear curve. Due to this fact, the neutral point for an aircraft can be approximated by positioning the CG at a longitudinal position where the curve becomes horizontal, and hence C_m has a constant value regardless of AoA. This seems not to be the case regarding these types of hydrofoils which complicates the design process. Figure 2.15 shows the effect of lowering the CG.

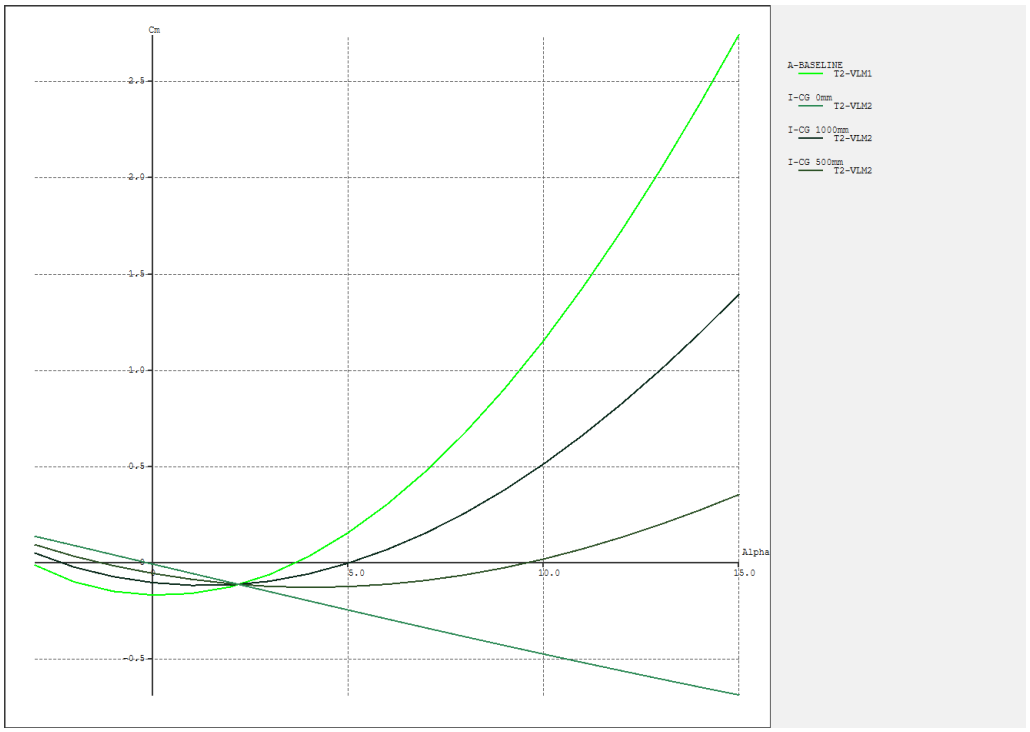

Figure 2.15: The $C_m - \alpha$ plot showing the effect of lowering the centre of gravity.

Regarding the rear wing, it appears that decreasing the AoI (to negative angles), increasing the area, increasing the fuselage length, and increasing the aspect ratio have largely the same effect on the $C_m - \alpha$ plot. However, the most drastic effect on increasing the C_m values is a result of changing the angle of incidence, and the most drastic effect on shifting the curve is a result of scaling the area. All these parameters effectively increase the moment produced by the rear wing, and such a result should be expected. This is also in accordance with the $C_L/C_D - \alpha$ plot. All the parameters except increasing fuselage length increase the rear wing's down-force, reducing the hydrofoil's total resultant lift. Since decreasing the AoI of the rear wing creates more drag, the maximum lift/drag ratio is expected to be at a higher AoA. AoI has the largest effect on changing the peak value and position of the $C_L/C_D - \alpha$ curve.

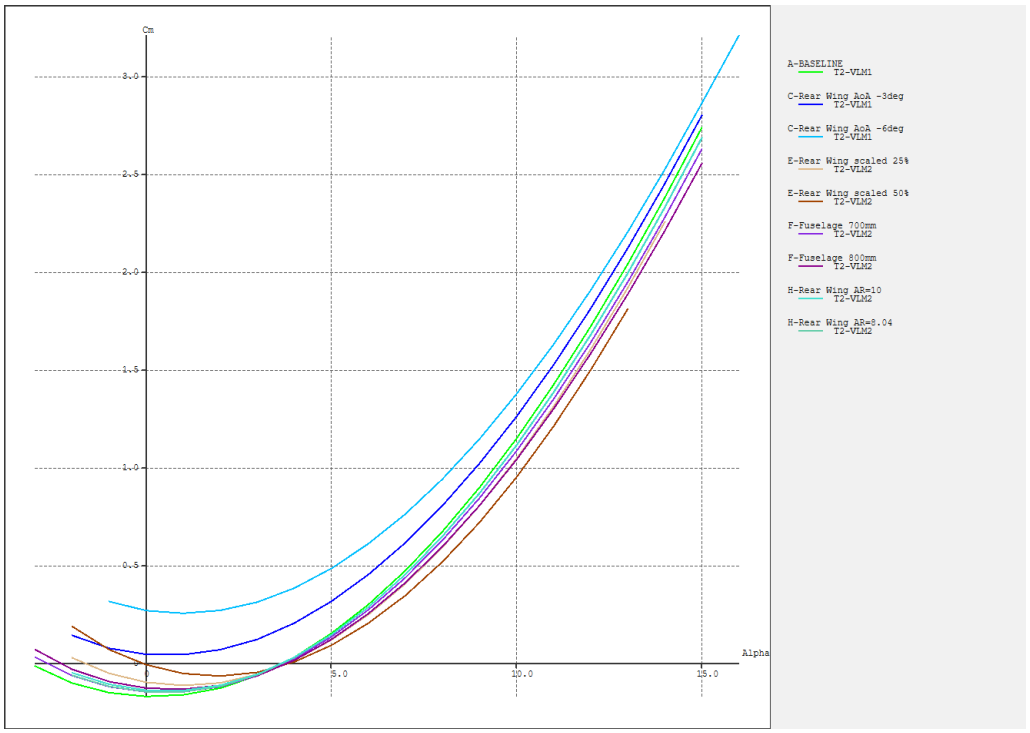

Figure 2.16: The $C_m - \alpha$ plot showing the effect of changing parameters related to the rear wing.

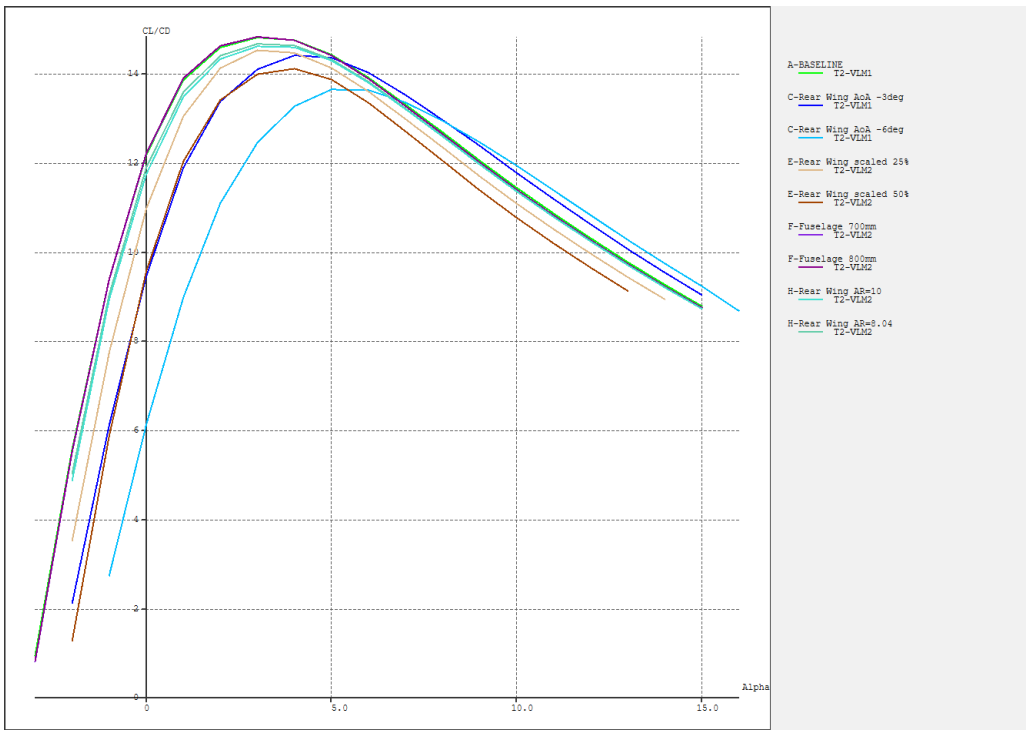

Figure 2.17: The $C_L/C_D - \alpha$ plot showing the effect of changing parameters related to the rear wing.

Regarding the front wing, increasing the AoI causes the curve in both the $C_m - \alpha$ and $C_L/C_D - \alpha$ plot to shift to the left. Since increasing front wing AoI increases the lift produced at any given hydrofoil AoA, the zero-moment angle will correlate with a lower AoA. Since increasing the AoI also increases drag, the peak in the $C_L/C_D - \alpha$ plot will be lower. An interesting observation is that changing the AoI of the front wing does not change the range of lift-producing AoAs for the hydrofoil. This implies that the entire operational AoA range of the hydrofoil is shifted towards lower AoA when the front wing AoI is increased. Front wing AoI can hence be regarded as a major design parameter.

Considering the increase in front wing area and the increase in front wing aspect ratio, they seem to essentially have the opposite effect on the $C_m - \alpha$ plot. When the area is increased, the curve becomes less parabolic, while when the AR is increased, the curve becomes more parabolic. Increasing the area effectively increases the range of pitch stable AoAs while increasing AR narrows this range. A more parabolic curve implies that the slope is steeper; hence, the restoring moment will be greater when the hydrofoil is subjected to pitch disturbances. Regarding aircraft dynamics that deal with linear curves, a steep slope is synonymous with more pitch stability since the greater the deviation is from the zero-moment angle, the larger the restoring moment becomes. While this is also true for hydrofoils in board sports, pitch stability is apparently more complex due to the parabolic nature of the moment coefficient. Compromises need to be made between the range of stability and the strength of the restoring moment.

The hydrofoil will have two zero-moment angles, one asymptotically stable to the left and one marginally stable to the right in the $C_m - \alpha$ plot. The AoA of marginal stability determines the highest AoA at which the hydrofoil is operational. At higher AoA, $C_m > 0$, and the slope is positive, a combination of conditions that will make the hydrofoil unstable and pitch its nose up uncontrollably. It is not to say that this is always an undesirable behavior. Some experienced riders can use this fact to their advantage and make the hydrofoil shoot up and out of the water to perform freestyle tricks, but for the general less experienced rider, it can be assumed that predictable pitch stability is more desired.

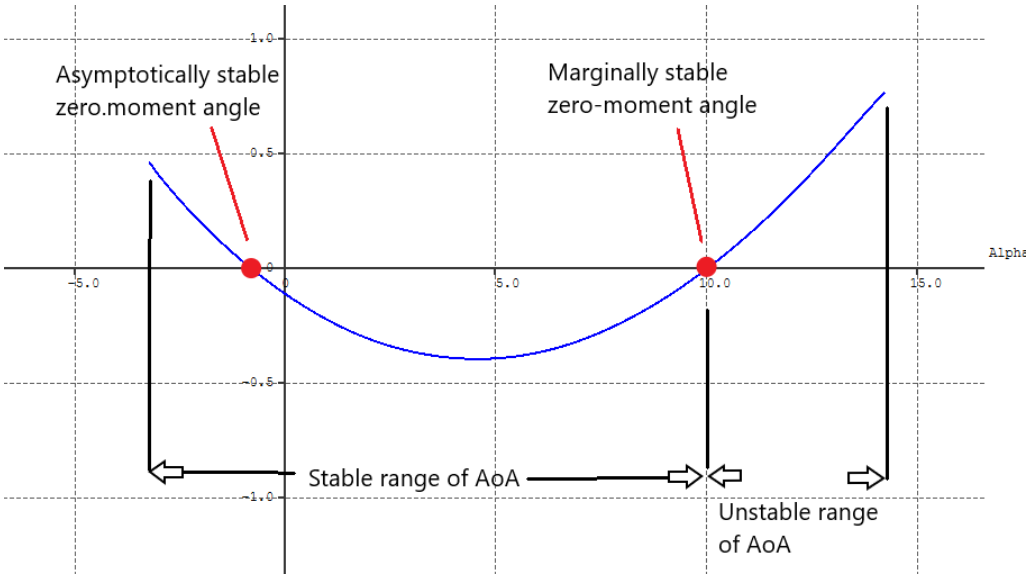

Figure 2.18: A $C_m - \alpha$ plot illustrating the stable and unstable regions of AoA.

Regarding the $C_L/C_D - \alpha$ plot, increasing the front wing area results in a better lift/drag ratio with the peak at slightly higher AoA, meaning that the increase in lift is more significant than the parasitic drag that follows a greater surface area. The lift/drag ratio is greatly improved when increasing the front wing AR. The peak is, however, achieved at approximately the same AoA regardless of this increase. This correlates with literature, where it is described that the induced drag is reduced when the wingtips are further apart. However, a higher aspect ratio results in the graph cutting at a lower AoA, which implies that the hydrofoil will experience stall at a lower AoA. This is further supported by the literature.

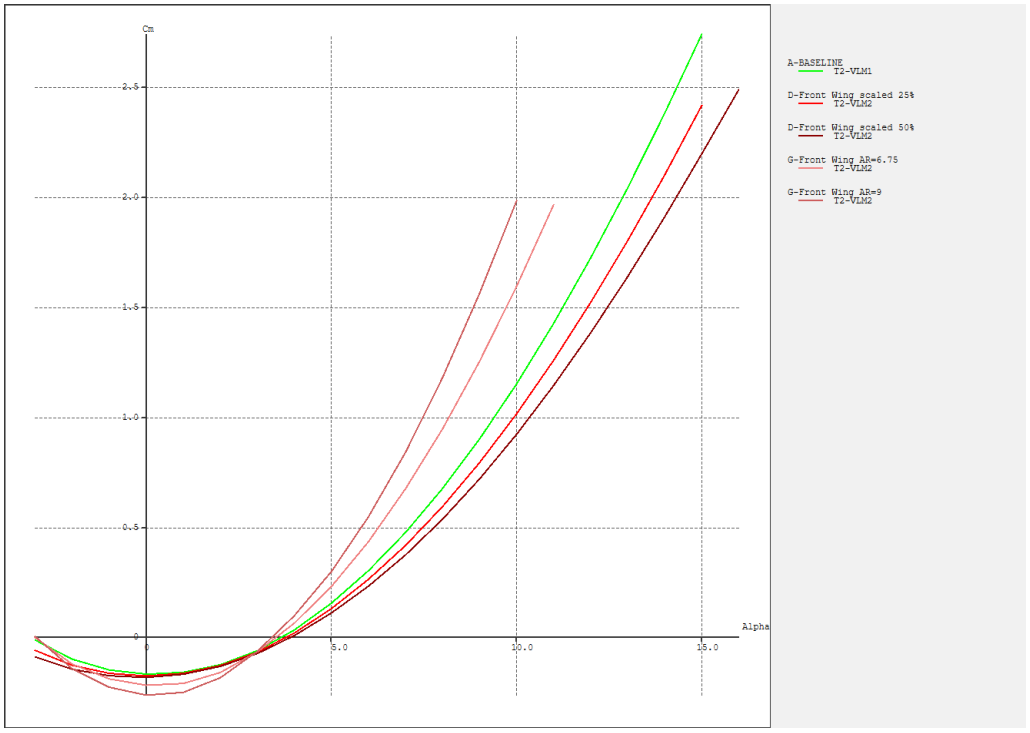

Figure 2.19: The $C_m - \alpha$ plot showing the effect of increasing front wing area and aspect ratio respectively.

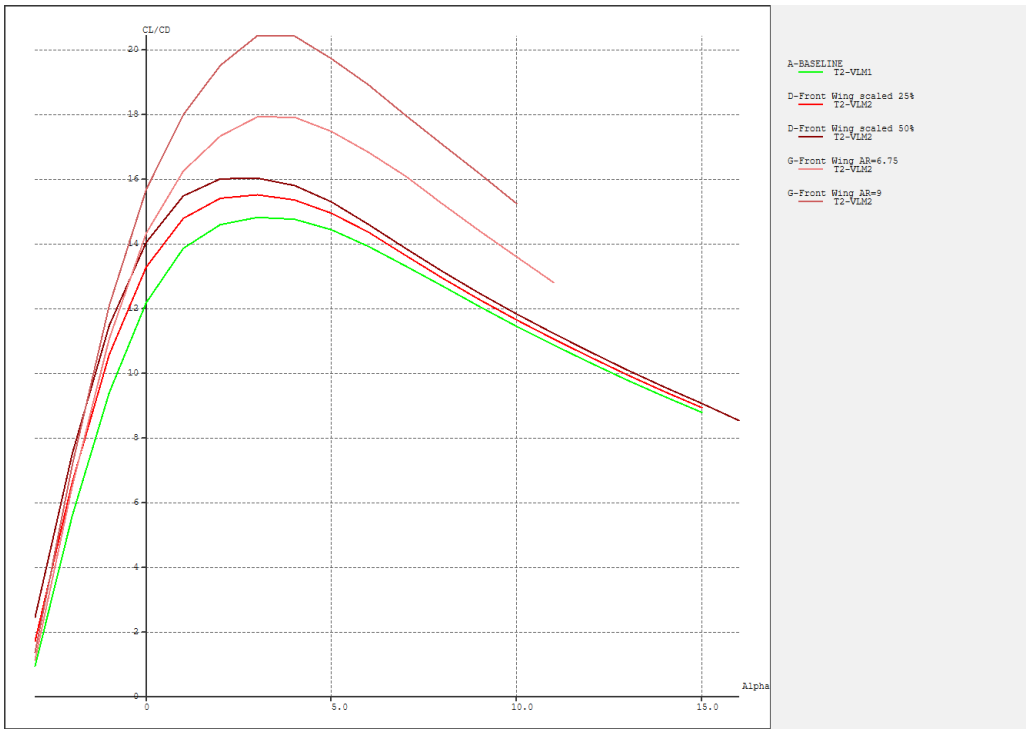

Figure 2.20: The $C_L/C_D - \alpha$ plot showing the effect of increasing front wing area and aspect ratio, respectively.

2.4.3 Tuning the Design Parameters

The light green curve corresponds to the baseline reference model in all the produced Xflr5 plots. When looking at the light green $C_m - \alpha$ plot corresponding to the reference model, it is clear that the associated parameters would make for a poor hydrofoil design. Firstly, the curve does not have a section with a negative slope that crosses the x-axis and hence does not have stable, positive moment coefficients or a stable zero-moment angle. The stable region is narrow, from only -3°to 3.6°, and the curve is relatively flat in the stable region. When optimizing the design, the goal is to manipulate the curve so that;

- The curve crosses the x-axis near the origin of the plot so that the zero-moment angle is close to AoA = 0, which is desirable at cruise speed.
- Expand the range of stable AoA so that the hydrofoil will be forgiving to disturbances.
- Have sufficient negative slope in the stable region for responsiveness to disturbances.
- The cruise speed that corresponds to the zero-moment angle should be between 6m/s and 9m/s, which is suitable for less experienced riders.
- The peak of the lift/drag ratio should be at reasonable AoA close to the zero-moment angle.

From the results tables 2.1 and 2.2, it is shown that the $C_m - \alpha$ curve can be manipulated with the following steps to obtain the desired stability response;

1. Move the curve to the right by decreasing rear wing AoI (this will, however, also move the curve up); Increase rear wing area; Increase fuselage length; Increase rear wing AR.
2. Move the curve down by moving the CG forward.
3. Shift the range of stable AoA to the left by increasing front wing AoI.

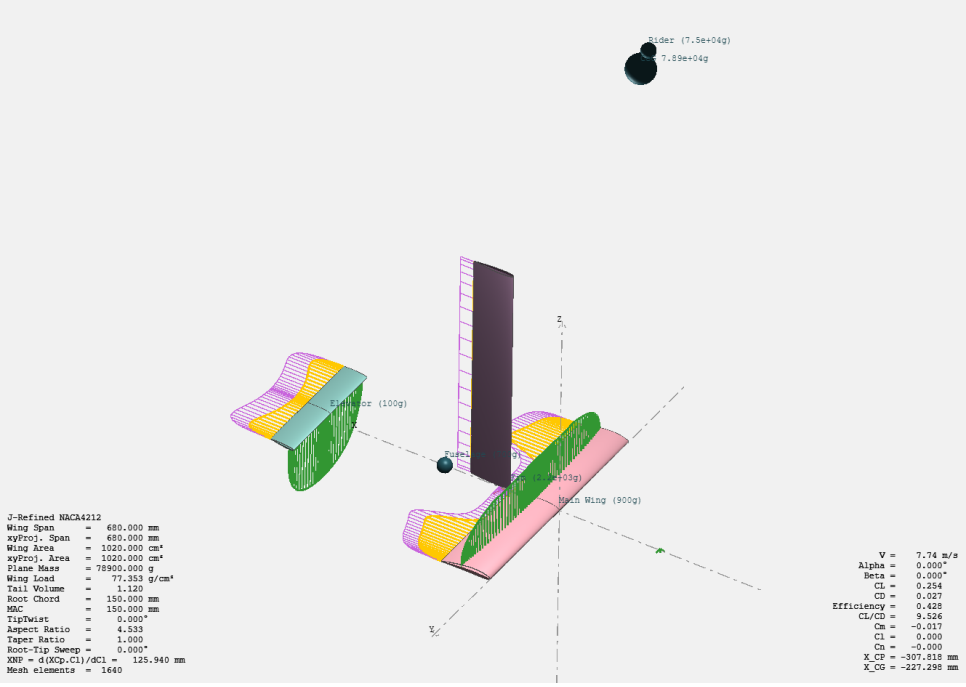

Figure 2.21: The optimized Xflr5 model with the final design parameters to be used as the basis for the CAD model. The green, yellow and pink regions illustrate the distribution and magnitude of the lift, parasitic drag, and induced drag, respectively, at AoA = 0.

By changing the parameters with an iterative approach, the following functional designs were obtained;

Table 2.3: The hydrodynamic design parameters that correspond with the three functional design tunings, compared with the reference design.

Design Tuning	Blue	Red	Pink	Green (reference)
Longitudinal position of rider CG	-250mm	-300mm	-400mm	0mm
Front Wing AoI	2deg	2deg	2deg	0deg
Rear Wing AoI	-6deg	-4deg	-4deg	0deg
Front Wing Area	1020cm^2	1020cm^2	1020cm^2	1020cm^2
Rear Wing Area	252cm^2	396cm^2	396cm^2	252cm^2
Front Wing AR	4.53	4.53	4.53	4.53
Rear Wing AR	5.14	5.11	5.11	5.14
Fuselage length	700mm	620mm	700mm	600mm
Operating speed	7.90m/s	8.16m/s	8.45m/s	Not stable

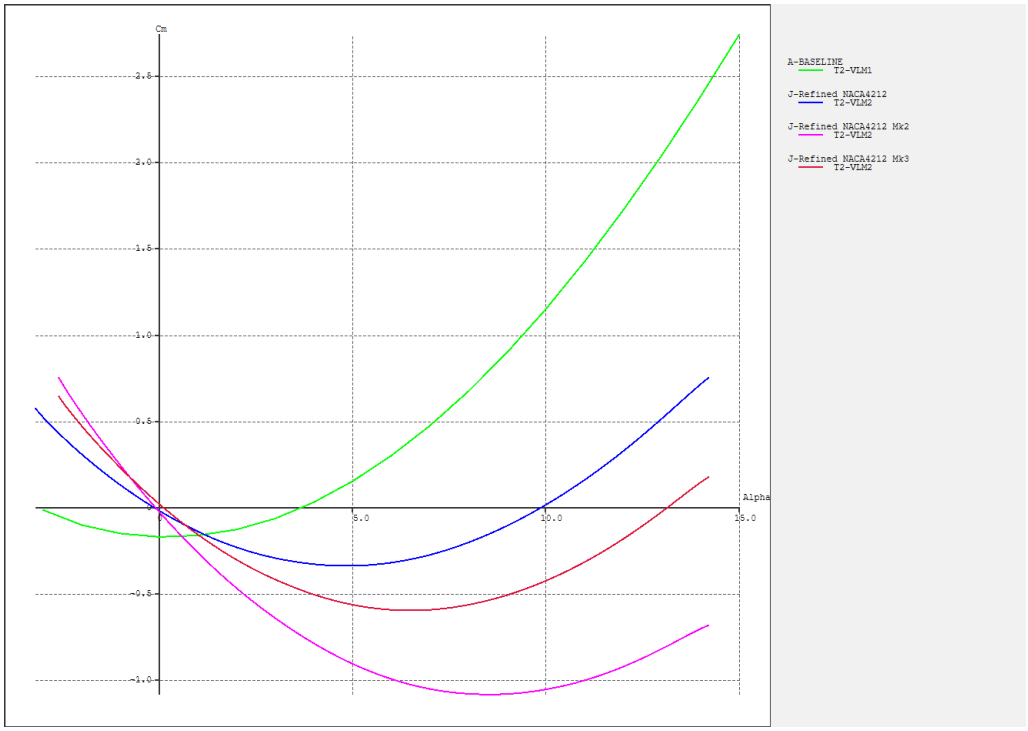

Figure 2.22: The three functional designs compared with the reference design in a $C_m - \alpha$ plot.

From the $C_m - \alpha$ plot in figure 2.22, it is observable that all the functional designs cross the x-axis at approximately AoA = 0°. This slight difference will although imply a small difference in theoretical operating speed of almost 2km/h, which is visible in the $C_M - V$ plot in figure 2.24. It is observable that the pink design is stable in the entire region up to the critical angle of stall at AoA = 14°, while the red design becomes unstable at AoA = 13°, and the blue design at AoA = 10°. The pink design also has the steepest slope of the three and can be deemed the most stable design. The drawback with this design is that the rider needs to position the CG far forward, resulting in a wide stance on the board where most of the weight needs to be kept at the front foot. This stance can feel unnatural and lead to muscle fatigue, which is a highly undesirable product property. The pink design was the first one developed. The parameters were optimized from this design to facilitate that the rider CG could be positioned further back, which led to the red and blue designs. From the red and blue curves, it is observable that moving the CG aft is compromised by less range of stability and a more mellow slope of the curve.

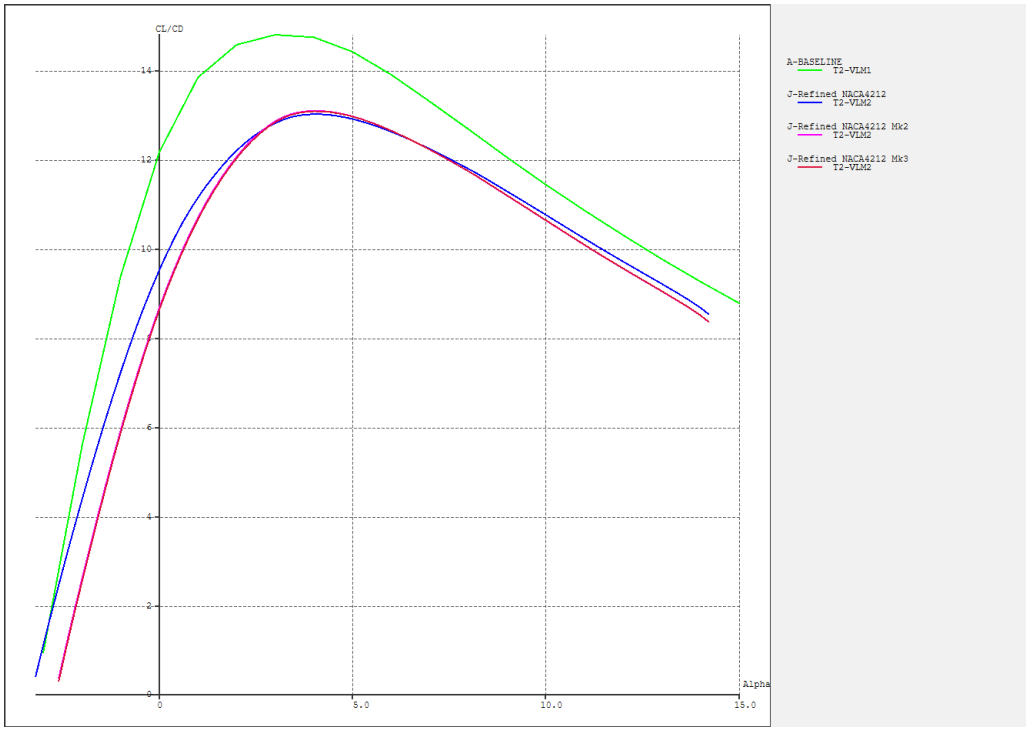

Figure 2.23: The three functional designs compared with the reference design in a $C_L/C_D - \alpha$ plot.

Regarding the $C_L/C_D - \alpha$ plot in figure 2.23, it is observable that the functional designs have a poorer lift/drag ratio compared with the reference design. This is mainly due to an increase in form drag following greater wing AoI. The blue design has a better lift/drag ratio about the zero-moment angle than the red and pink designs, which has approximately the same curve. The blue design, in addition, also produces lift at lower AoA then the other designs. Choosing the final design parameters will be based on what is deemed the best compromise between the factors mentioned earlier.

It is concluded that the blue design parameters are the best compromise as it offers the most comfortable rider position with an adequate pitch stability range and a more efficient design. These parameter values will be used further in the design process and development of the hydrofoil CAD model. In addition, the leading edge of the mast is moved forward to 160mm from the leading edge of the front wing. This seemingly has no apparent hydrodynamic effect while having the positive effect of being able to use a shorter board.

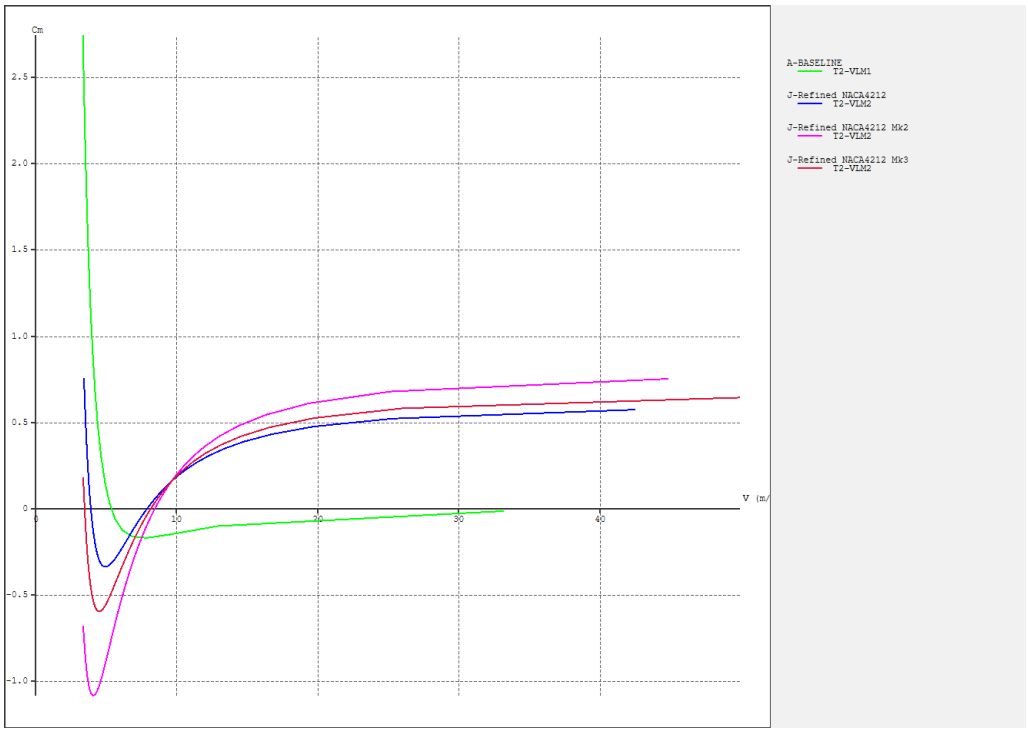

Figure 2.24: The three functional designs compared with the reference design in a $C_m - V$ plot.

2.4.4 Discussion of Dihedral and Stability Modes

A useful functionality in Xflr5 is the ability to conduct stability analysis. This type of analysis documents the response to different disturbance modes in the longitudinal and lateral directions and can be visualized in root loci plots as complex eigenvalues. The position of the eigenvalues on the negative part of the real axis determines the degree of stability, while the position on the imaginary axis accounts for the oscillatory frequency of the mode. It was explained earlier that anhedral/dihedral aid in lateral stability. An experiment was conducted where the front wing of the optimized model was modified with a progressive -15° anhedral and 15° dihedral. This had marginal effect on the $C_m - \alpha$ and $C_L/C_D - \alpha$ plot, and the effect is likely due to the slightly decreased projected wing plan area. This lack of influence on pitch stability is further supported by the root locus plot for the longitudinal modes, where the phugoid and long period mode are virtually the same for all models, while the short period mode is about 4% less stable for the dihedral design, which is deemed insignificant. Regarding the lateral modes, there are significant differences between the designs, as expected from theory. The Dutch roll mode is 41% more stable for the anhedral front wing compared with the flat front wing, which again is 41% more stable compared with the dihedral front wing. There is a slight percentage difference of 4% between the models regarding the roll damping mode and no significant difference regarding the spiral mode. In figure 2.25 and 2.26, the blue points represent the flat wing, the black points represent anhedral, and the brown points represent dihedral. Anhedral has clear advantages in terms of lateral stability, but it is decided not to incorporate this aspect and rather keep the geometry flat for ease of manufacturing.

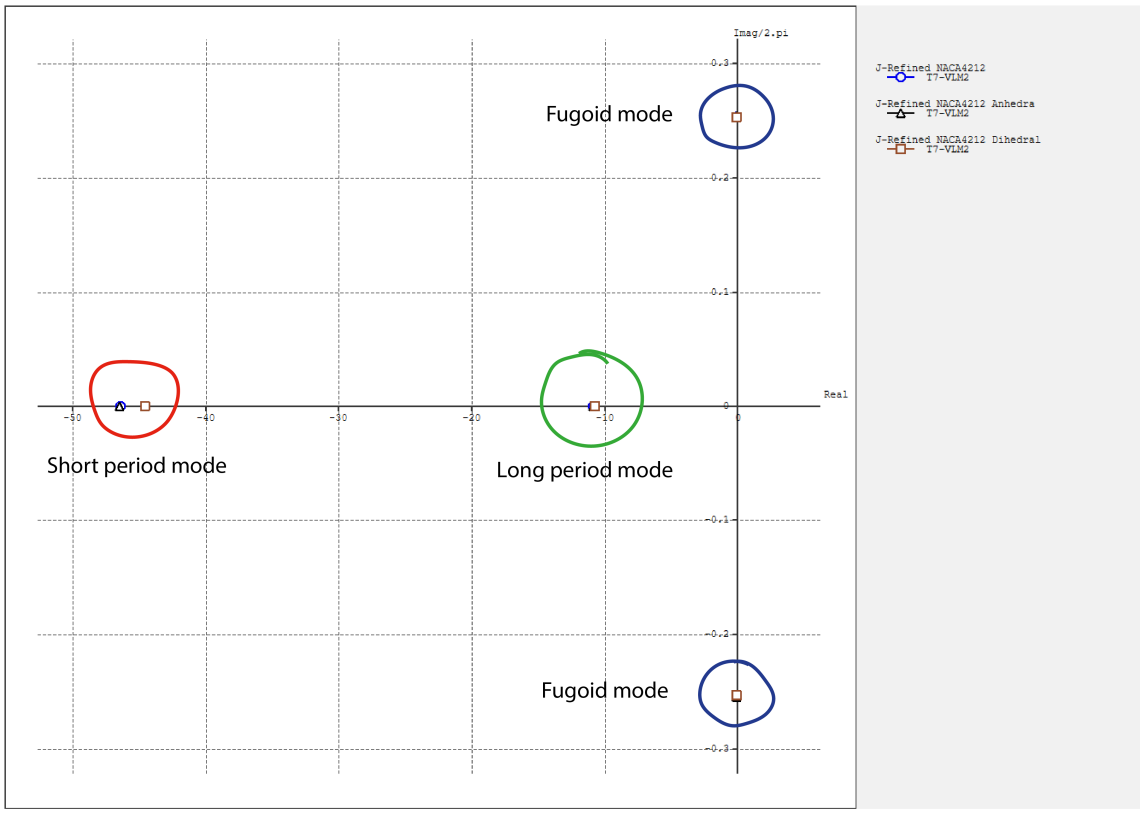

Figure 2.25: The root locus plot of the eigenvalues for the longitudinal stability modes.

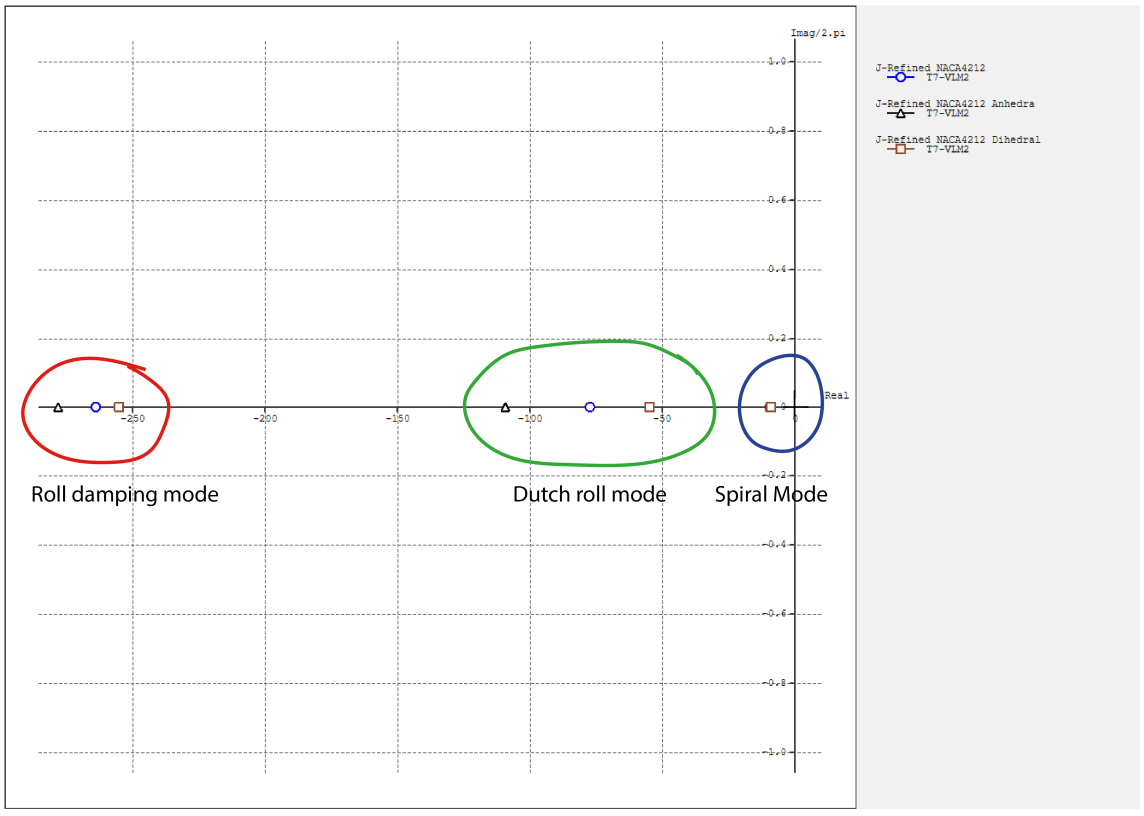

Figure 2.26: The root locus plot of the eigenvalues for the lateral stability modes.

Chapter 3

Material Selection & the Structural Design Concept

3.1 Introduction

Choosing materials for the various parts of the hydrofoil assembly must follow the hydrofoil's structural requirements. It is desired that the compliance and weight of the hydrofoil should be minimized while also keeping costs down. This will maximize the responsiveness and establish predictable control of the hydrofoil. In other words, it is desirable to use materials that maximize the specific stiffness of the structural parts without the risk of failure. This chapter will investigate metallic and composite materials known to be used by established brands along with their respective manufacturing methods. In addition, some (for this application) non-traditional short-fiber composites will also be investigated. As with the hydrodynamic design, the structural design and materials will be chosen based on less complex manufacturing methods that require less worker input and production equipment. Manufacturing methods will also influence the limitations of the structural design. The manufacturing methods will determine which geometric features are possible to implement without incurring unreasonable manufacturing costs. At the end of this chapter, a structural design concept will be proposed that is designed with specific materials and manufacturing methods in mind.

3.2 Material Comparison

3.2.1 Metallic Materials

The advantage of producing parts in metal is that the processes generally can be highly automated and that the material cost is lower compared to composites. The following manufacturing methods could be used in realtionto the respective parts of the hydrofoil. The mast can be conveniently designed with a constant cross-section; hence, extrusion would be the most natural way of manufacturing this part, as many brands currently do. Advantages of extrusion are excellent surface finish, thigh tolerances, and that the part can be designed with thin walls and material in strategic locations to take advantage of inertial stiffness in a similar fashion to I-beams, which reduces mass while maintaining high stiffness. Aluminum 6063 is more suited for extrusion than aluminum 6061 [31]. Due to this fact, and since the young's modulus is about the same, aluminum 6063 is the more favorable alternative at a lower material cost, as long as there is no risk of yielding. The process is suitable for high production volumes, but the initial tooling cost can be expensive.

The fuselage, mounting plate, and wings generally have several features and more complex geometry. Hence, casting and CNC-machining are suitable manufacturing methods. Die casting offers a quality surface finish and tight tolerances and can be favorable for large production volumes. However, the initial tooling cost can be expensive, and post-machining of certain features is likely required. Sand casting is deemed unfavorable as an alternative due to the poor surface finish, which will significantly impact drag while otherwise being an inexpensive process. CNC machining offers excellent surface finish and tolerances. The process is favorable for smaller production runs and has the advantage that all features can be created with a single machine. It also makes testing and redesigns faster and easier if necessary since there is no need to redesign and manufacture a mold.

3.2.2 Fabric Composite Materials

The parts mentioned above can also be constructed using a composite sandwich method with an inner core material wrapped in a fiber composite skin. For such a method, the core can be formed by subtractive manufacturing. Various CNC processes are suitable as such. A 3-axis CNC router can create parts of 3D complexity but may require reorientation if several curved surfaces are present. By utilizing a 4-axis machine, the core parts can be made in a single step with minimal post-processing. If the core material is foam, then hot-wire cutting can be suitable. A 4-axis CNC hot wire machine can create 3D geometries but is limited compared to CNC routing as it can only achieve curved geometry in one plane and projected linear lines in the two other planes. A significant advantage of CNC hot wire cutting is that the initial cost is low since the machinery is inexpensive and that the process is quicker than CNC machining.

There are many processes for making composite parts with traditional fabrics, each with its advantages and disadvantages. The processes have in common that they are quite labor intensive, and the part design and choice of manufacturing technique at large influence the degree of manual labor required. When it is desired to keep manufacturing costs low, it is highly beneficial to make choices that minimize manual labor involvement. The manufacturing processes can be divided into those involving dry fiber reinforcements where resin is added and processes where the fibers are already pre-impregnated with resin.

The simplest form of composite parts manufacturing is the hand layup process. This process essentially only requires dry fiber reinforcement that is then applied to the core material or a mold and wetted out with matrix material by hand with no consumables involved. The drawbacks of the hand layup method are that there tend to be pinholes on the surface, and it is hard to control the amount of matrix material used. Vacuum resin infusion, on the other hand, is a more complicated process that requires additional steps and several consumables. In this process, a vacuum pump is used to draw resin from a reservoir through the laminate. Advantages of vacuum resin infusion include a better and more consistent fiber-to-resin ratio than a hand layup, with few pinholes. The disadvantage of vacuum resin infusion is that the setup process is rather complicated, which

risks the part being flawed during production. The setup process is also quite time-consuming. Regarding prepreg, the manufacturing process is similar to vacuum resin infusion, as vacuum here also is required. However, there is no need to wet out the layup as the fibers are already impregnated with the matrix material. This has the advantage that the ideal ratio of fibers to matrix is already predetermined, which maximizes strength and reduces the chance of imperfections. The drawback of this method is that it requires a mold or vacuum bag to apply pressure, as well as an autoclave for curing. The prepreg fabrics are also expensive and need a freezer for storage.

3.2.3 Chopped Fibre Composite Materials

Both thermoplastics and thermosets can be reinforced with chopped fiber materials. Adding chopped fibers to resins and plastics improves the mechanical properties of the materials while still maintaining a low weight. An advantage of chopped fibers is that the material is cheaper and easier to produce than large continuous fabrics. Chopped fiber composites are well suited for manufacturing through various molding methods. Molding generally requires less manual input by workers than layup manufacturing processes and can be highly automated in many cases. Due to the use of molds and the formability of the chopped materials, parts of great complexity can be manufactured.

Polyamides (PA), also known as nylons, are regarded as some of the most important engineering thermoplastics. These thermoplastics work well as the matrix material for glass particles, and the properties can be tailored to meet the specific needs of several engineering applications by controlling the polyamide crystallinity and amount of glass fibers included. Relative to other thermoplastics, glass-filled nylon offers the main characteristics of high mechanical strength, rigidity, and toughness. In addition, the material offers good fatigue strength, resistance to creep, and mechanical damping. These properties ensure that glass-filled polyamides perform well when exposed to high static loads and elevated service temperatures, compared with many other thermoplastics [27]. Regarding thermosets, composite bulk molding compound (BMC) is a viable material choice. Carbon fiber bulk molding compounds offer tensile strengths similar to aluminum while having a significantly lower density. This allows for the fabrication of lightweight and strong components that can replace metal parts. These compounds consist of a high volume fraction of carbon fibers of a certain length, combined with a pre-mixed epoxy resin system. These compounds are used to manufacture parts through compression molding at high pressure in permanent heated molds. Hence the resulting parts can have high geometric complexity and excellent tolerances and surface finish.

Forged carbon fiber is an inherently similar material to carbon BMC. Forged carbon fiber is made through compression molding of chopped carbon fiber tow, much like BMCs. These two processes differ in that BMCs are delivered pre-mixed with resin from the supplier, while forged carbon is made by loading a mold with the chopped carbon fiber tow and resin on the spot. It is, however, also possible to make forged carbon parts with chopped pre-preg tow if the mold can facilitate it. The advantages of forged carbon fiber are that the process requires minimum resources regarding mold design and is suitable for one-off or small batch production. On the other hand, it is possible to make forged carbon through injection molding for large production runs but will require more expensive and complex molds. Another advantage is that forged carbon fiber is inexpensive compared to other carbon materials. Compression-molded forged carbon fiber is, however, not much studied in the literature, and there is little detailed information about the mechanical properties and the manufacturing process.

Table 3.1: The mechanical properties of possible materials to be used for structural hydrofoil parts.

Material	**PA66 GF50[18]**	**Toray BMC[20]**	**Aluminum A380[1]**	**Aluminium 6061[1]**
Density [g/cm3]	1.61	1.48	2.76	2.70
Flexural Modulus [GPa]	9.0	68.9	71.0	68.9
Yield Strength [MPa]	115	256	159	276
Possions Ratio	0.33	0.3	0.33	0.33
Specific Stiffness	5.6	46.6	25.7	25.5
Specific Strength	71	173	58	102

3.3 Composite Theory

Carbon composites have a fundamental role in established hydrofoil part design. These are advanced materials that require knowledge to analyze and simulate, and it is thus of interest to have the fundamental theory and design considerations in place.

3.3.1 Micromechanics of Lamina

As the name implies, unidirectional fabrics have all the fibers oriented in a single direction. This kind of fabric is not woven in an interlacing manner but has the tows stitched together. This eliminates crimp and maintains maximum strength and stiffness of the fibers. In the experimental study conducted by S. Eksi and K. Genel, it was concluded that the elastic modulus in the 1-direction of the UD carbon fiber samples was 1.87 times greater than the elastic modulus for the plain weave carbon fiber samples, while the ultimate tensile strength was 2.43 times greater for the UD samples compared with the plain weave samples [14]. Another benefit of UD fabrics is total control over the fiber direction of the individual plies in the laminate. Hence the strength and stiffness performance characteristics can be tailored to known load cases, or it is possible to layer the ply directions in a way that results in a quasi-isotropic laminate. The main drawback of UD fabrics is that they can fall apart easily due to the lack of interlacing and difficulty reorienting the fibers if not placed correctly. It is also relatively more fragile when machine than woven fabrics. It is often common practice to use a woven fabric as the top and bottom layer of the layup to improve machinability, durability, and aesthetics [36].

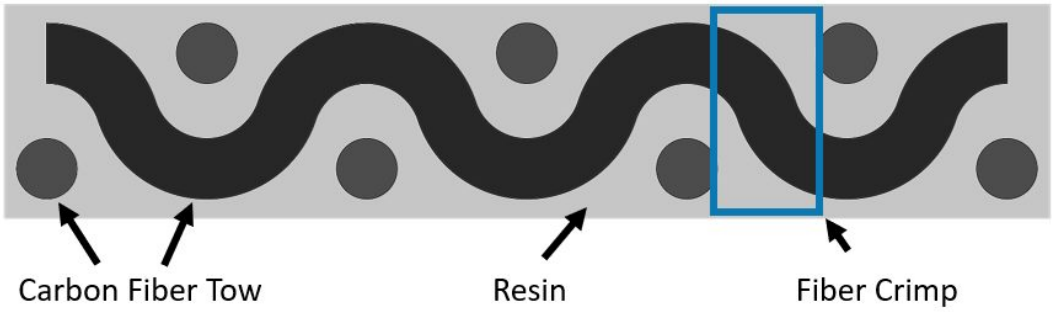

Figure 3.1: Illustration of composite weave crimp [36].

It is necessary to have insight into the mechanical properties of composite material to be able to simulate a part's behavior. Since a composite lamina is comprised of fiber reinforcements and a matrix that each has its respective mechanical properties, it is necessary to determine the resulting properties when combined. There are two common ways of determining the mechanical properties of an orthotropic lamina. One way is by collecting data through conducting macro mechanical experiments using test specimens, e.g. tensile testing. The other way is to estimate the mechanical properties with micromechanical models based on the properties of the constituents. In a prototyping application, it may be justified to use numerical models rather than more time-consuming test-data collection, even though the estimates are less accurate. The objective is to determine the moduli of the lamina in terms of the respective modulus and volume fraction of the constituents. The fiber volume fraction is an essential parameter for the stiffness of composite materials, and it is expressed with the following formula.

$$V_f = \frac{Volume\ of\ Fibres}{Total\ Volume\ of\ Composite\ Material} \tag{3.1}$$

$$V_m = 1 - V_f \tag{3.2}$$

The simplified numerical models are based on the following assumptions in table 3.2;

Table 3.2: Assumptions for the numerical approximations of the mechanical properties of composite laminae [3].

Lamina	Fibres	Matrix
Macroscopically homogeneous	Homogeneous	Homogeneous
Linearly elastic	Linearly elastic	Linearly elastic
Macroscopically orthotropic	Isotropic	Isotropic
Initially stress-free	Regularly spaced	Free of voids
	Perfectly aligned	
	Perfectly bonded	

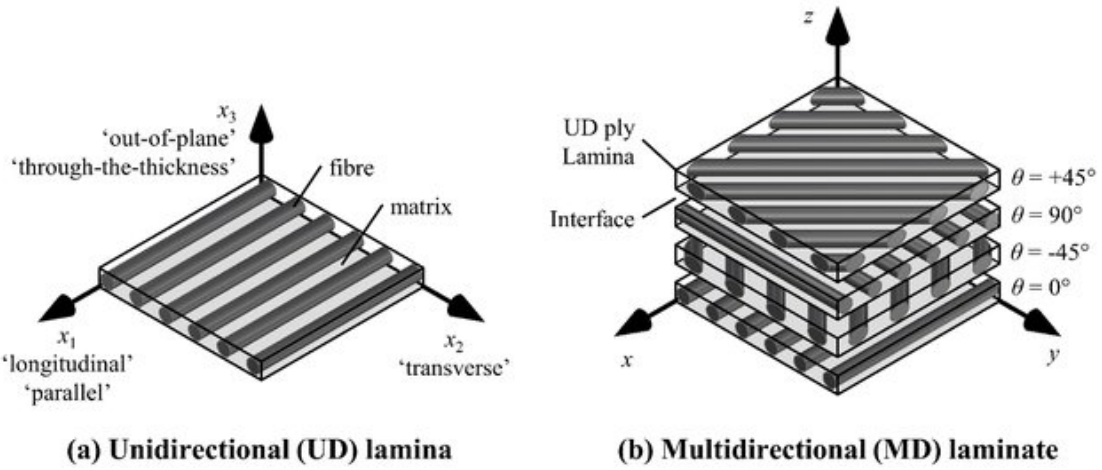

Figure 3.2: a) The principle directions of a UD lamina in the local coordinate system and b) the directions of UD laminas in a multidirectional laminate [21].

For determining the E_1 modulus of the composite in the fiber direction, i.e., the 1-direction, we assume that the strain is equal for both the fiber and the matrix in a representative volume element. This model is analogous to the load sharing of springs in parallel, and thus, we derive the rule of mixtures where the apparent Young's modulus is defined as [3];

$$E_1 = E_f V_f + E_m V_m \tag{3.3}$$

For determining the E_2 modulus of the composite in the transverse direction, i.e., the 2-direction, we assume that the stress is applied to both the fiber and the matrix in a representative volume element. This model is analogous to the load sharing of springs in series, and thus, we derive the rule of mixtures where the apparent Young's modulus is defined as [3];

$$E_2 = \frac{E_f E_m}{V_m E_f + V_f E_m} \tag{3.4}$$

The major Poisson's ratio ν_{12} can be estimated in a similar manner to the E1 modulus. It is based on the assumption that the fiber strains equal the matrix strains in the fiber direction, i.e., the 1-direction. Then the related transverse deformation must follow the same fashion [3];

$$\nu_{12} = \nu_m V_m + \nu_f V_f \tag{3.5}$$

3.3.2 Calculating Reinforcement and Resin

Since composite forging is a closed mold compression molding process, it is necessary to calculate the necessary amount of material to use. The final part volume equals the designed cavity between the mold tool pieces. This fact can be used to determine the amount of reinforcement material, given a desired final part density. The following equation describes how these entities are related [23];

$$V_{part} = \frac{m_{part}}{\rho} \tag{3.6}$$

In SolidWorks, the volume of a part can be computed. First, it is necessary to assign a density to the part in question; then, under section [Evaluate] -> [Mass Properties], the part volume will be shown along with other parameters. From the volume of the part and the assumed desired density of the final composite material, the mass of needed fiber is calculated with a rearrangement of the above equation [23];

$$m_{part} = \rho V_{part} \tag{3.7}$$

For forged components using chopped carbon fibre, the ideal density is assumed to be $\rho = 1.4g/cm^3$ and the optimal fibre to resin ratio is 60%/%40, (fibre/resin) by weight fraction, generally for this process. These assumptions lead to the following expression for calculating the mass of required dry fiber reinforcement [23];

$$m_{fibre} = 0.6m_{part} = 0.6\rho V_{part} \tag{3.8}$$

The amount of required resin is calculated by multiplying the required fiber mass by 1.25. This is not an exact science but rather a rule of thumb for complete wet out. The multiplication factor of 1.25 is assumed from an economic standpoint, and more resin can be mixed if desired. When assuming this rule, some resin will be squeezed out of the enclosure during the compression molding process. If more resin is needed during the lamination process, more can be mixed, given sufficient pot life [23];

$$m_r = 1.25m_f \tag{3.9}$$

3.3.3 Laminate design considerations

Some general design considerations have been compiled based on test results, experience, and analytical models. These rules can be regarded as best practices in typical composite applications. It is important to emphasize that these guidelines are general, and deviations from them are often necessary for some designs, but they present a solution for robust design in simple applications regarding layups and bolted connections. The following laminate guidelines were proposed by Christos Kassapoglou and summarised the essence of the laminate analyses presented in the book Design and Analysis of Composite Structures with Applications to Aerospace Structures [10].

1. The laminate layup should be symmetrical unless there is a reason to do otherwise. By having a symmetric layup, the B matrix is equal to zero, and bending coupling is avoided.
2. The laminate layup should be balanced, meaning that every ply should have a duplicate ply of the same thickness and material, but with an angle of opposite sign. By making the laminate balanced, the A16 and A26 terms in the matrix equal zero, eliminating extension/shear coupling.

3. Bending/twisting coupling should be avoided when possible. This can be achieved by only using UD plies in the 0 and 90 directions. Whenever this is not feasible, it is preferred that the D16 and D26 terms are small in comparison to the rest of the D matrix. This is achieved by grouping together $\pm\theta$ plies.

4. The 10% rule is a generalization that at least 10% of the fibers in a laminate should be oriented in each of the directions 0, 45, -45, and 90. This creates redundancy against secondary load cases that have not been analyzed in the design process and could lead to premature failure.

5. The number of UD plies oriented in the same direction right next to each other should be limited. If several plies oriented in the same direction are located right next to each other, a matrix crack will more easily grow through a larger laminate section. Fibers running in the same direction should therefore not exceed a thickness of 0.6-0.8mm.

6. Plies oriented in the 0 direction should be located as far away from the neutral axis as possible when it is desired to maximize bending stiffness, as this will maximize the D11 term.

7. Plies oriented in the 45/-45 direction should be located as far away from the neutral axis as possible when it is desired to maximize against panel buckling, as this will maximize the D66 term.

8. Fastener rule 1: The skin thickness / fastener diameter ratio should be less than $\frac{1}{3}$ to minimize the bending of fasteners.

9. Fastener rule 2: During out-of-plane loading, the skin thickness should be greater than $\frac{2}{3}$ of the countersunk dept to avoid pulling a fastener through the skin.

10. Fabric plies should be placed as the outermost layer in a laminate to provide damage resistance against impacts. This help to contain fiber splitting to the outermost layer.

11. A skin laminate should be dominated by 45/-45 plies for improved shear strength and stiffness.

12. Fastener rule 3: At least 40% of the fiber should be in the $\pm 45°$ directions for improved load transfer in bolted joints under axial load.

13. Fastener rule 4: The distance between fasteners should be at least 4-5 times the fastener diameter to limit stress concentration interactions. In this way, the stress distribution around one fastener does not overlap with its surrounding fasteners, and the by-pass load is fully developed. This limits stress concentration effects in designs where the requirement can be implemented.

14. Fastener rule 5: To minimize edge effects, a fastener should be located at a minimum distance of 2.5D + 1.3mm from an edge or flange. This will ensure that the stress distribution around the fastener resembles that of an infinite plate.

3.4 The Design Concept

The main goal of the hydrofoil concept is to keep manufacturing costs low while simultaneously being a lightweight and stiff design. This is done by developing a concept that requires little manual labor during manufacturing and utilizes inexpensive machinery and material with high specific modulus and specific strength. From table 3.1, it is seen that the carbon bulk molding compound has superior mechanical properties. The BMC has the lowest density, and the flexural modulus is equivalent to machined aluminum 6061-T6. Cast aluminum has a slightly higher modulus but at the expense of having the lowest yield strength.

Specific stiffness and specific strength are two useful metrics for evaluating materials. Since the design of the hydrofoil is stiffness driven, the specific stiffness metric is arguable the most critical parameter, as long as the strength is within acceptable limits for the load case. As stiffness depends on the features' geometry and not only the inherent modulus, a material with a lower elastic modulus can be justified by having a low material density. Even though the part will be bulkier for equivalent stiffness, the resulting weight can still be lower. This is expressed through specific stiffness to which the carbon BMC is superior.

Since carbon BMC requires advanced heated tooling, it is deemed unfavorable to use as a material in this project. However, forged carbon fiber does not require advanced tooling and has similar traits to carbon BMC in terms of material composition and manufacturing method. Little information is found about the mechanical properties of forged carbon fiber; hence, it is interesting to investigate if this material is suitable for use in certain hydrofoil parts. It is of interest to examine if forged CFRP shares similar mechanical properties to BMC. Since both forged CFRP and carbon BMC parts are created through compression molding, the design concept to be developed is manufacturable with both methods.

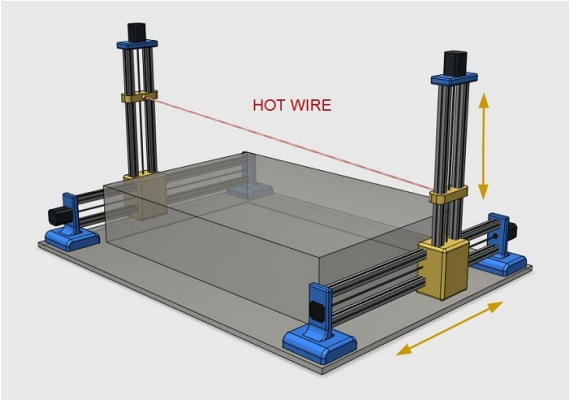

(a) An illustration of the 4-axis hot wire CNC-machine concept. Each respective end of the wire is able to be moved in the plane individually.

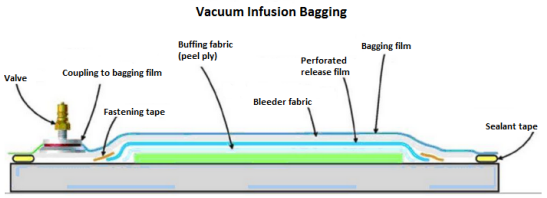

(b) An illustration of the vacuum resin infusion process. All the main components are labeled [29].

In this proposed design concept, the fuselage, mounting plate, and rear wing are deemed favorable to be manufactured with forged carbon fiber through compression molding due to the more complex geometry. Regarding the front wing and mast, they are deemed favorable to be manufactured with a foam core material wrapped in a carbon fiber skin. This is a traditional construction concept that has been proven by several hydrofoil brands. Due to the constant cross-section of the front wing and mast foil profiles, it is favorable to manufacture the cores with a 4-axis CNC hot-wire cutter. The skin can then be applied through a simple wet layup for cost savings or through vacuum resin infusion with an envelope bag for better surface finish and fiber/resin ratio. It is desirable to eliminate bolted connections between the structural parts of the design. Hence the proposed structural design will offer a solution for joining the fuselage, mast, and mounting plate into a single part. The solution is to incorporate flanges at the fuselage and the mast. The flanges are 100mm long and have the same NACA profile as the mast core. This way, the mast core, and flanges can be adhesivly bonded together. Then the fiber skin can be applied by overlapping the core and the two flanges to connect the individual parts into a single structural part rigidly.

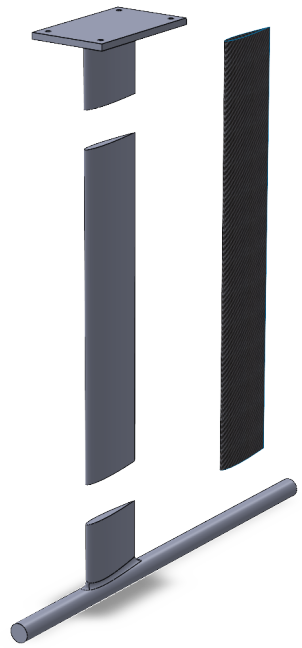

(a) Perspective view of the four parts in the structural hydrofoil assembly.

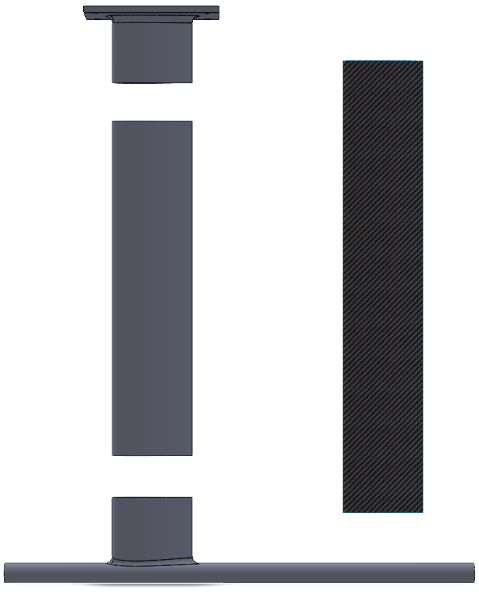

(b) Side view of the four parts in the structural hydrofoil assembly.

Chapter 4

Material Testing

4.1 Introduction

Forged carbon fiber manufactured through compression molding has been relatively little studied in the literature. Several factors will determine the mechanical properties of such a composite material, including the fiber length of the chopped tow, the mechanical properties of the fibers, the properties of the resin system, and the volume fraction of fibers. In Chapter 3 it was concluded that carbon fiber/epoxy BMC was the most favorable material for structural hydrofoil parts due to the high specific stiffness, strength, and ability to create complex geometries with minimal effort. Foam core fabric composites have superior specific stiffness and strength but are complex and labor-intensive to manufacture. Forged carbon fiber shares many of the aspects of BMCs. The main difference is that the forged carbon/epoxy compound is created on the spot at the time of molding. Because of this, there is a lot of freedom related to storage, the choice of epoxy pot life, and hence no need for curing in a heated mold. The carbon tow can also be sourced through unused trimmings for other parts, further reducing material cost and decreasing environmental impact. Due to this, if the mechanical properties of forged carbon fiber resemble that of carbon/epoxy BMC, then it would be a suitable material for low to medium production runs.

In this chapter, it is of interest to investigate the manufacturing process of forged carbon fiber with rudimentary manufacturing equipment and to establish the stiffness and strength of such a material. It is of interest to establish if forged carbon fibre is a viable material choice for use in structural hydrofoil parts.

4.2 Flexural Testing Theory

Flexural testing, also known as bend testing or transverse beam testing, are tests designed to evaluate the mechanical behavior of materials subjected to simple beam loading. The tests are well suited for relatively flexible materials. As a material bends, it is subjected to a complex combination of stresses, including tension, compression, and shear. Due to this fact, flexural testing often gives more realistic information about a material's response to loading scenarios encountered in the field. Many products are subjected to several different and often intricate load cases. Hydrofoils are no exception, and simple uniaxial tension and compression tests may not provide the most relevant information about the material's behavior in these scenarios [28]. Hence in this chapter, the material samples will be created and flexural tested with the primary goal of determining the elastic modulus and strength of the material.

In its simplest form, a flexural test is conducted by placing a test specimen on two support anvils and applying a load using one or two loading anvils to produce bending of the sample. The most common flexural tests are the 3-point and 4-point bend tests. In the 3-point test, the area of max stress is small and concentrated under the single loading anvil that applies a force at the midpoint of the specimen. The main advantage of this test is its simplicity. A 4-point test, on the other hand, equips two loading anvils that are equidistant from the midpoint of the sample. In this test, constant stress exists between the load rollers at the sample's inner span. An advantage of this test is that the sample is not experiencing shear stress at the inner span, whereas a sample subjected to 3-point bending will experience maximum shear at the loading point [28]. It is decided that the test specimens in this chapter shall be tested with 4-point bending since there is less need to account for shear stress and since the induced stress from bending will be constant between the load rollers.

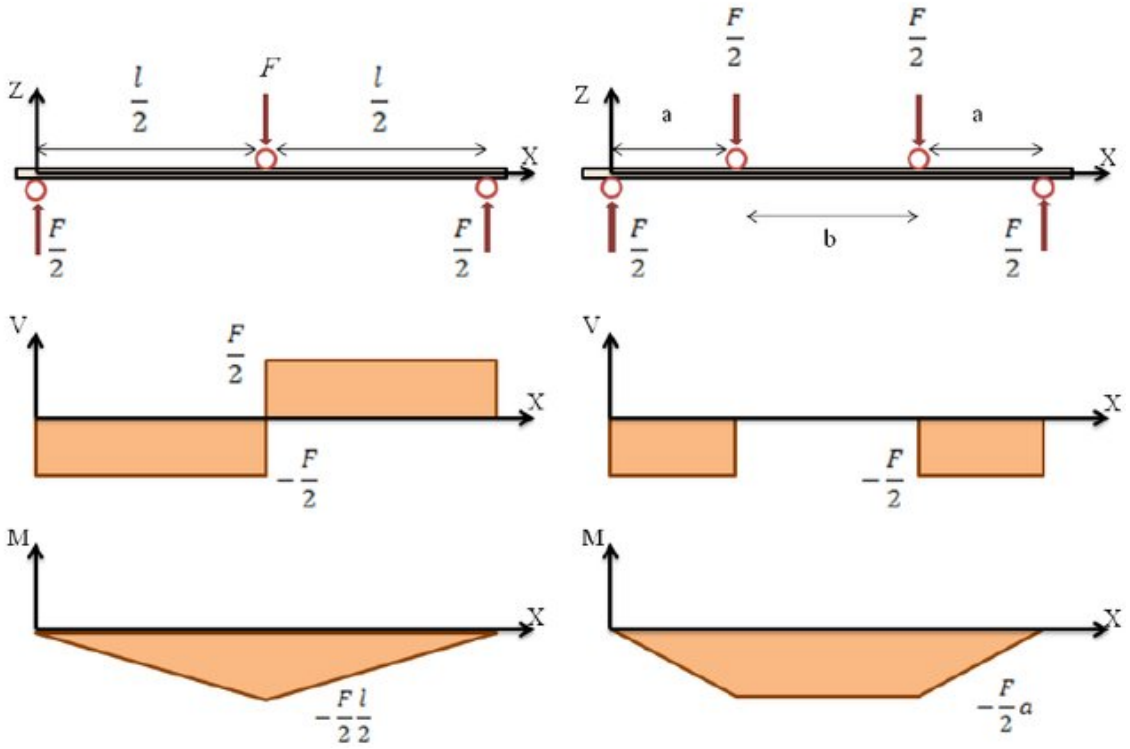

Figure 4.1: Shear (top)and moment (bottom) diagrams for the three-point and a four-point flexural test setup [6].

4.2.1 General Equations

The expression below describes the cross-sectional stresses in a member subjected to a bending moment about the axis normal to the member's span. The stresses in the beam cross-section are a linear function of the y-coordinate for beams with a symmetric cross-section about the xy-plane. In this particular case, the bending is defined about the z-axis [12];

$$\sigma(x, y) = \frac{M_z(x)}{I_z} y \tag{4.1}$$

Where $M_z(x)$ is defined as the moment about the z-axis as a function of the location along the span x, and I_z is the second moment of area about the z-axis. I_z can be determined by the following integral [12];

$$I_z = \int_A y^2 dA \tag{4.2}$$

For a rectangular cross-section, such as specified for a sample following the ISO standard for flexural testing, the integral equates to the following expression;

$$I_z = \frac{bh^3}{12} \tag{4.3}$$

Where b is the width of the beam cross-section and h is the height of the beam cross-section.

4.2.2 3-point Bending Equations

The maximum deflection of a sample subjected to a 3-point flexural test is described by the following equation, which has both one term for bending and one for shear;

$$\delta = \frac{FL^3}{48EI} + \frac{FL}{4\kappa Gbh} \tag{4.4}$$

The first term represents the deformation due to bending and the second term represents the deformation due to shear [25].

The maximum moment M_{max} is found at the middle of the beam span, at $x = \frac{L}{2}$ such that;

$$M_{max} = \frac{FL}{4} \tag{4.5}$$

The stresses in the rectangular beam cross-section of a test sample, subjected to a point load in the middle of the span length, are expressed as the following;

$$\sigma = \frac{3FL}{bh^3} y \tag{4.6}$$

Since the stress is a function of y, the maximum tensile stress is found at $y = \frac{1}{2}h$ on the bottom side of the sample, while the maximum compressive stress is found at $y = -\frac{1}{2}h$ on the top side of the sample, such that the maximum stress can be expressed as;

$$\sigma_{max} = \pm \frac{3FL}{2bh^2} \tag{4.7}$$

4.2.3 4-point Bending Equations

The following equation describes the maximum deflection of a sample subjected to a 4-point flexural test;

$$\delta_{max} = \frac{Fa}{48EI}(3L^2 - 4a^2) \tag{4.8}$$

Where L is the length of the support span, a is the length of each outer span, and EI is the stiffness. The following equation expresses the moment for 4-point bending. It is dependent on if the location is either outside or inside the loading span of the sample length;

$$M(x) = \frac{1}{2}(Fx) \tag{4.9}$$

when $0 < x < a$, and

$$M(x) = \frac{1}{2}(FL - Fx) \tag{4.10}$$

when $L - a < x < L$.

The sample will experience pure bending between the loading points, and hence the moment is constant along this span region. The maximum moment M_{max} can be computed at $x = a$;

$$M_{max} = \frac{1}{2}Fa \tag{4.11}$$

This leads to the following expression for maximum stress;

$$\sigma_{max} = \pm\frac{3Fa}{bh^2} = \pm\frac{FL}{bh^2} \tag{4.12}$$

The last part of the above equation is only valid when the inner loading span is one-third of the total support span, and hence, $b = a = \frac{1}{3}L$. Due to the separate loads in the 4-point flexural test setup, it is possible to apply strain gauges to the middle section of the test specimen to record the strains experienced. The strain can, however, be calculated with the following expression, which eliminates the need for complicated setups involving strain gauges;

$$\epsilon = \frac{h}{2}\kappa = \frac{h}{2}\frac{M}{EI} \tag{4.13}$$

where κ is the curvature.

4.3 Method - Investigation of Mold Design Forged CFRP Properties

From the ISO 14125 standard for flexural testing of composite materials, the appropriate specimen dimensions for flexural testing of forged carbon fiber were identified in accordance with a class II material. This class includes plastics reinforced with mats, continuous matting, and fabrics, as well as mixed formats (e.g. SMC, BMC, DMC, GMT) [35]. Forged carbon fiber is presumed to suit this class due to the short fiber similarity to other molding compounds. This ISO standard will serve as a guideline for the flexural testing, but liberties will be taken as seen fit.

Table 4.1: ISO 14125 standard class II test specimen dimensions.

Material	Specimen length (l)	Outer span (L)	Width (b)	Thickness (h)
Class II	80	64	15	4

In addition to creating test specimens for flexural testing, it is also in this chapter of interest to gain knowledge about the manufacturing method for making compression molded parts from forged CFRP. Hence, three iterations of the test specimen molds will be created, each based on the previous in an attempt to find best practices in mold design. The molds will be designed in SolidWorks. Due to time restrictions and manufacturing constraints, the molds will be additively manufactured on a FFF 3D printer.

Regarding the forged CFRP material, the effect of two parameters on the resulting stiffness and strength are of interest to be investigated. That is the effect of longer vs. shorter fiber length and the effect of loading the equivalent of a wet layup into the mold vs. pre-mixing the fiber and resin before loading it into the mold. Hence, three batches of test specimens will be produced with slight variations in the manufacturing conditions. The conditions of the different batches are summarized in the table below.

Table 4.2: The mold design, fiber length, and production method for each of the respective batches.

	Mold Design	**Fibre Length**	**Pre-mix**
Batch 1	1 Iteration	25mm	No
Batch 2	2 Iteration	12mm	Yes
Batch 3	3 Iteration	12mm	No

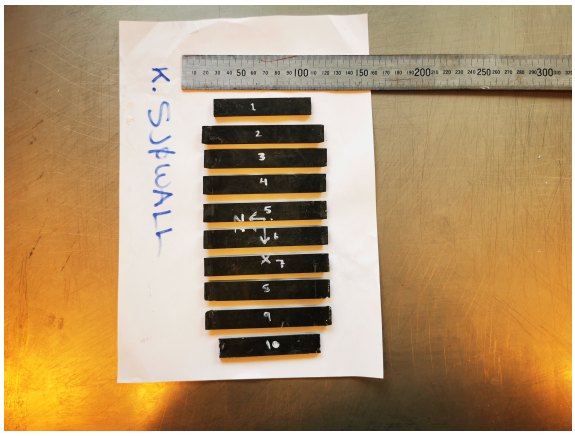

(a) Test specimens from the first batch. Specimen 1 and 10 are cut to final dimensions.

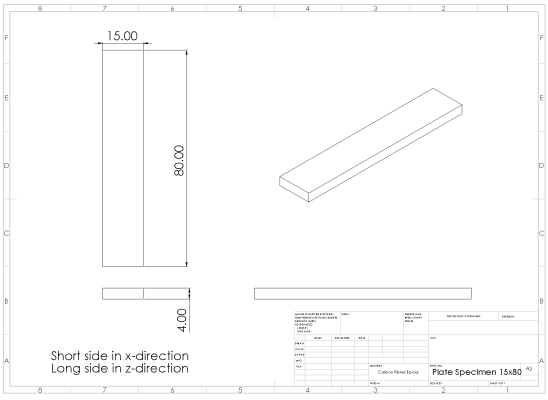

(b) Machine drawing of the test specimens.

Figure 4.2: Batch 1 test specimens.

4.3.1 The First Iteration of the Forging Process

The mold was designed in a two-piece configuration, incorporating a piston concept to contain the material within the mold when applying pressure. Hence the core part of the mold protrudes 5mm, while the cavity part of the mold has a 9mm void to account for the final plate thickness of 4mm. This way, the volume of the final part is known, and the amount of required fiber can be calculated. The CFRP plate itself was designed to be 162mm x 92mm. The plate has a 45-degree chamfer on all edges to serve as the draft angle. This plate chamfer was projected to the cavity side of the mold. However, this solution causes the remaining mold depth to have parallel walls, which may be undesirable. A 2mm chamfer feature was added to all external corners for easier separation of the two mold halves. Two holes were also incorporated into the design of the cavity to allow for push extraction of the final part. The two mold pieces were additively manufactured with PLA as the filament material on a Prusa MK3S 3D printer, with a 15% infill density and 0.15mm layer height.

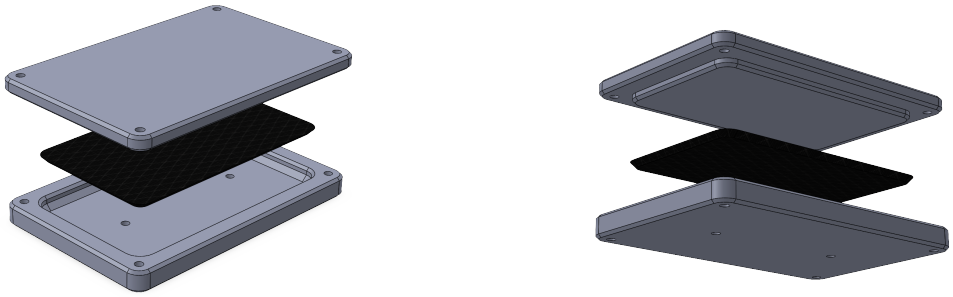

(a) Exploded view of the first iteration of the test specimen mold, seen from the topside.

(b) Exploded view of the first iteration of the test specimen mold, seen from the bottom side.

Figure 4.3: Exploded views of the first mold.

In SolidWorks the volume of the CFRP plate was found to be $63.6cm^3$ with an estimated weight of $88.96g$, when assuming a final density of $\rho = 1.4g/cm^3$. When using equation 3.8, the amount of needed fiber reinforcement for the test plate equates to;

$$m_f = 0.6\rho V_{part} = 0.6 * 1.4g/cm^3 * 63.6cm^3 = 53.4g$$

Using equation 3.9, the amount of needed resin for a test plate equates to;

$$m_r = 1.25m_f = 1.25 * 53.4g = 66.2g$$

The Epocote RIMR 135/RIMR 137 epoxy/hardener infusion resin system (see Appendix G) was used as the matrix material in the molding process. This system is mixed with a ratio of 100:30 parts by weight. For simplicity and redundancy, 70g epoxy and 21g hardener were mixed, which is more resing than needed. The reinforcement was of standard modulus type carbon fiber tow, cut to 25mm pieces.

The layup process was executed as follows. Firstly the two mold halves and all the bolts were covered in release wax. The extraction holes in the mold were also closed with wax to prevent resin from curing in them. Then the surface of the mold cavity was wet out with epoxy. A portion of fiber reinforcement was loaded into the mold cavity and wetted out with resin. This step is repeated several times, with more fiber being loaded into the mold and wetted out until all the reinforcement is placed inside the mold cavity. The concept of this process resembles a simple wet layup with continuous reinforcement fabrics.

The two mold halves were then lightly bolted together at the corners using M5 bolts, and clamps were applied in the middle to supply pressure. The bolts and clamps were progressively tightened over time to allow the excess resin to flow out of the mold. It is vital not to tighten the mold

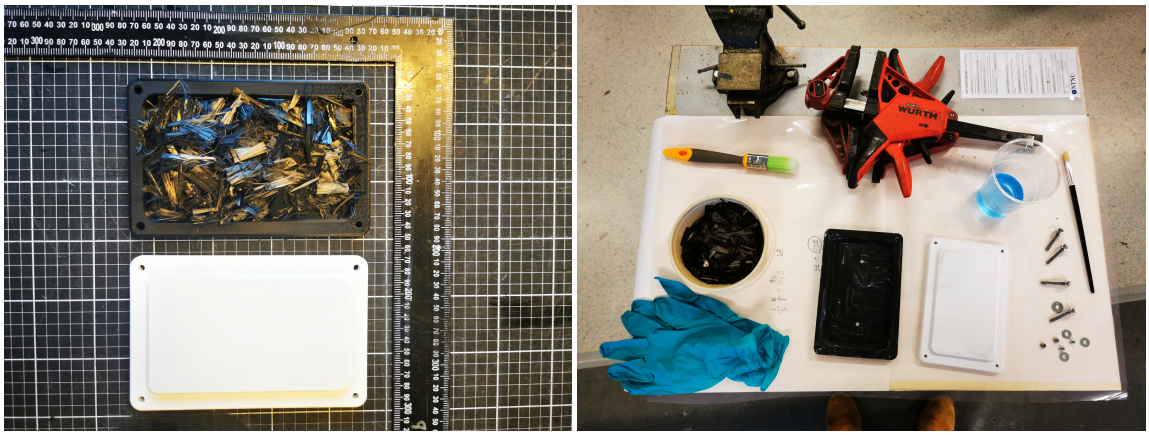

(a) The first iteration of the test specimen mold loaded with dry carbon fibre.

(b) The equipment and consumables used for the first forging.

Figure 4.4: Manufacturing the first batch of test specimens.

too quickly as this could result in hydraulic locking. Ultimately, the two mold halves should be completely flush with each other. The CFRP plate was left to cure for 30 hours and was then post-cured at 50°C for 4 hours. Note that post-cure temperature was limited due to the low Tg of PLA used as the mold material.

After curing, the two mold halves were separated using hand tools. The excessive cured resin had to be chipped away at the edges before it was possible to wedge the mold halves apart. However, the plate was stuck to the cavity side of the mold and proved hard to extract. It was visible that fiber/epoxy flash had penetrated the gap between the mold halves during the tightening process. This flash had right angles and effectively locked the part in place. Another factor is the grooves in the PLA mold as a result of the fused filament 3D printing process. These grooves create surface roughness and enable spaces for the epoxy to solidify. These problems can be countered by a draft angle running the entire depth of the cavity, a deeper piston design so that the fiber is better contained, a tighter tolerance between the mold halves, and sanding of the mold surfaces to remove the grooves.

The extraction problem was solved by putting the mold in the oven at 90°C, which exceeds the Tg of the PLA material. Once heated, the mold cavity could be bent using pliers and the CFRP plate extracted. However, this rendered the mold warped and unusable for another batch. The flash was then trimmed off using a Dremel, which proved highly effective due to the low abrasion resistance of carbon fiber. From table 4.6 it is observable that the final measured weight after post-machining is close to the SolidWorks estimate. However, since some of the material has been removed, the density of the final CRPF plate likely deviates from the assumed density $\rho = 1.4 g/cm^3$.

Table 4.3: The dimensions of the test specimens from the first batch.

Batch 1	**Thickness [mm]**	**Width [mm]**	**Length [mm]**
Sample 1	3.96 ±0.36	14.58	80.55
Sample 2	4.00 ±0.30	14.80	79.54
Sample 3	4.07 ±0.26	14.95	80.71
Sample 4	4.17 ±0.29	15.01	80.68
Sample 5	4.15 ±0.20	15.03	81.15
Sample 6	4.09 ±0.17	15.00	81.58
Sample 7	3.96 ±0.20	14.96	81.43
Sample 8	3.91 ±0.22	15.02	81.59
Sample 9	4.04 ±0.16	15.01	81.34
Sample 10	4.14 ±0.17	14.91	80.46
AVERAGE	**4.05 ±0.21**	**14.93**	**80.90**

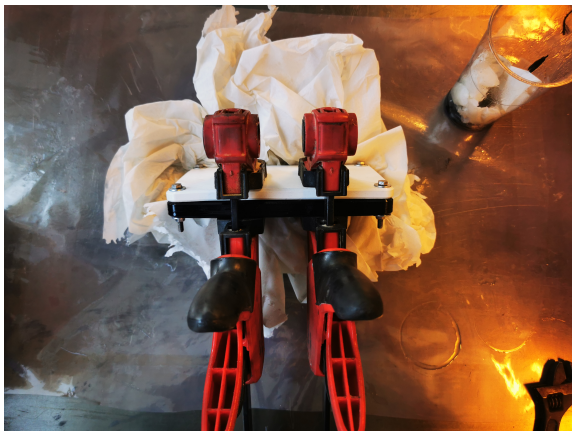

(a) The mold bolted and clamped shut.

(b) The mold bolted and clamped together.

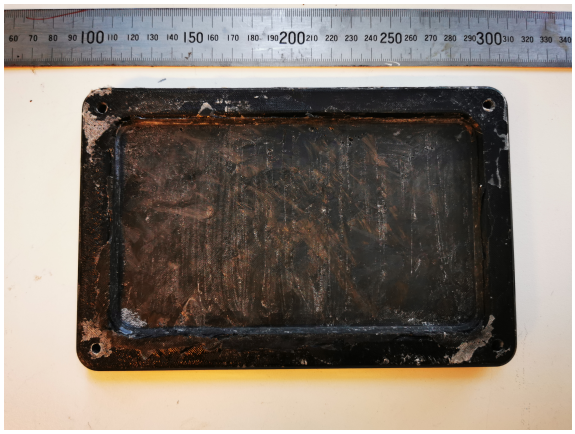

(c) The forged CFRP test specimen plate in the mold cavity.

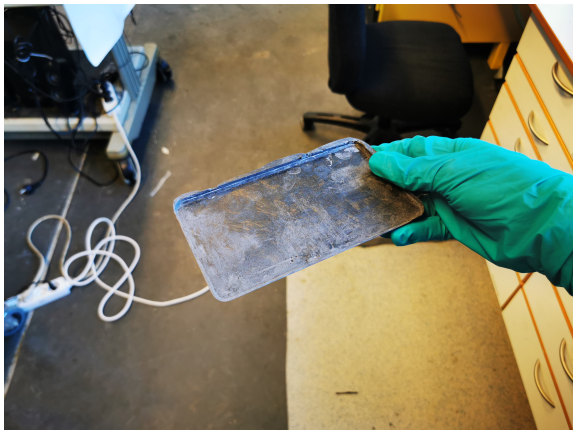

(d) The forged CFRP test specimen plate was removed from the mold.

Figure 4.5: Manufacturing the first batch of test specimens.

A water jet was used to cut the processed plate into test specimens of the desired dimensions. From the CFRP plate, it was possible to create 10 test specimens. The dimensions of the specimens were measured with a digital caliper to investigate the specimens' variability. The samples were also inspected visually in order to detect defects. Three thickness measurements were recorded along the length of each specimen; one measurement at the midpoint and one at either end of the specimens. Since the samples are water jet cut, the thickness is the dimension that will vary the most, while the width and length will be fairly consistent. One measurement is recorded of the respective lengths and widths of the samples. The mean values and deviations for the midpoint measurements were calculated, and the data was summarized in table 4.3. The caliper was zeroed in between measurements.

4.3.2 The second Iteration of the Forging Process

Another test plate was created to investigate the effects of fiber length and pre-mixing fiber and resin on the resulting composite material. Several changes were made to overcome the lack of the first iteration regarding the mold design. The reiteration had two main design goals in mind. It was observed in the first batch of specimens that the variance in thickness was relatively high, and this variance should ideally be as close to zero as possible. The other primary design goal was to make extracting the forged CFRP plate easier and not have to destroy the mold.

The new iteration of the mold was made larger than the previous one. The cavity dimensions were increased to facilitate a larger composite plate of 210mm x 120mm compared to the dimensions 162mm x 92mm of the first plate iteration. The motivation behind this decision was to allow more padding at the edges to be cut away, as it was hypothesized that the areas near the edges were more prone to molding imperfections or damage during extraction. The depth of the mold cavity was increased from 9mm to 15mm. This feature was changed in an attempt to keep all the material inside the mold cavity, as it was observed that the first plate had developed flash between the mold halves making extraction more difficult. The draft angle was changed to a continuous 10°.

The last feature added to the new iteration of the mold was related to clamping. The first iteration only had four bolt holes located at the corners of the mold, and in the second iteration, the number of bolt holes was increased to eight. The new design also incorporated bolt holes at the midpoints in addition to the bolt holes at the corners. This was implemented to allow for more uniform clamping pressure along the edges of the mold, which might make the resulting plate more uniform. Since the mold dimensions were made larger, the deflection between the bolts would be more extensive than in the previous mold if only four corner bolts were incorporated. In addition, the hole diameter was increased to facilitate M6 bolts compared to M5 bolts used in the previous iteration.

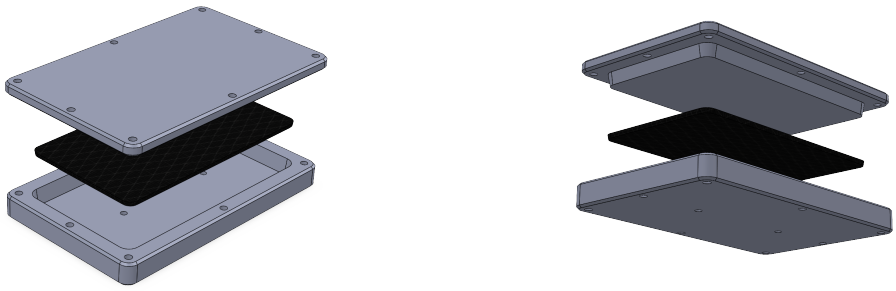

(a) Exploded view of the second iteration of the test specimen mold, seen from the topside.

(b) Exploded view of the second iteration of the test specimen mold, seen from the bottom side.

Figure 4.6: Exploded views of the second mold.

In SolidWorks the volume of the CFRP plate was found to be $94.6cm^3$ with an estimated weight of $132.5g$, when assuming a final density of $\rho = 1.4g/cm^3$. When using equation 3.8, the amount of needed fiber reinforcement for the test plate equates to;

$$m_f = 0.6\rho V_{part} = 0.6 * 1.4g/cm^3 * 94.6cm^3 = 79.5g$$

Using equation 3.9, the amount of needed resin for a test plate equates to;

$$m_r = 1.25m_f = 1.25 * 79.5g = 99.4g$$

The forging process was executed slightly differently than in the previous iteration. In this iteration, the required fiber mass was measured and put in a container. Double the amount of the calculated needed resin was mixed and kept in a cup. The fiber was then gradually mixed into the resin and wetted out. The final mixture was placed in a vacuum chamber for degassing and afterward compressed together. The mixed compound was spread out evenly in the mold cavity before the bolts and clamps were applied. Two blocks of wood and acrylic were placed between the mold and the clamps to apply even pressure. The bolts and the clamps were progressively tightened to facilitate excess resin to flow out until the two mold halves were eventually closed shut. The epoxy resin was then allowed to cure for 30 hours. With the new iteration of the mold design, the part extraction went smoother than in the previous iteration, and no significant difficulties were encountered. The plate was then post-cured at 90°C for 4 hours.

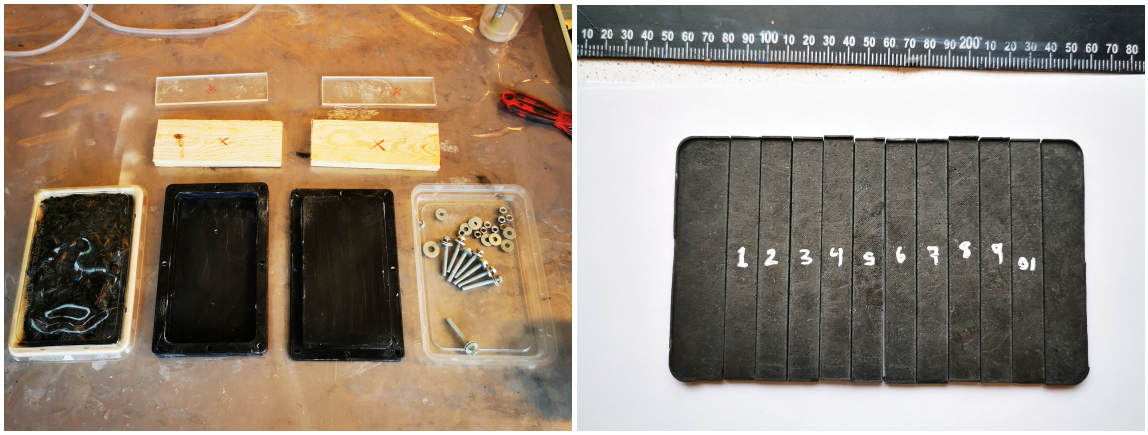

(a) The materials used for the second batch of test specimens.

(b) The batch 2 test specimens after being cut with the water jet..

Figure 4.7: The second mold iteration and the respective test samples.

The composite plate was cut using a water jet, and the new specimens of the new batch were measured in the same fashion as the first batch. From the measurements, it can be concluded that the variance in sample thickness has decreased. However, all the samples have a greater thickness than was initially intended. This indicates that the mold was not completely shut. A likely explanation is that due to the increased surface area of the plate, the clamps failed to apply enough pressure to compress the material sufficiently. This theory is further supported by the measured weight of the final plate. The weight after extraction is substantially higher than the SolidWorks estimate, as seen in table 4.6. Since the mass of fiber is known, this suggests that the final part contains more epoxy resin than intended and hence has a lower fiber volume fraction.

Table 4.4: The dimensions of the test specimens from the second batch.

Batch 2	**Thickness [mm]**	**Width [mm]**	**Length [mm]**
Sample 1	5.35 ±0.08	15.04	81.25
Sample 2	5.22 ±0.12	15.02	81.69
Sample 3	5.22 ±0.11	15.12	81.54
Sample 4	5.66 ±0.16	15.06	81.54
Sample 5	5.52 ±0.03	15.05	81.88
Sample 6	5.22 ±0.09	15.05	81.91
Sample 7	5.32 ±0.09	15.09	81.39
Sample 8	5.52 ±0.07	15.03	81.45
Sample 9	5.60 ±0.12	15.06	81.55
Sample 10	5.40 ±0.03	15.04	81.74
AVERAGE	**5.40 ±0.18**	**15.06**	**81.59**

4.3.3 The third Iteration of the Forging Process

In the third iteration, the properties of shorter fiber specimens manufactured as a wet layup were to be investigated. Hence the manufacturing process is the same as for the first CFRP plate. Since the previous mold design proved effective at extracting the cured plate, the third mold design essentially is a copy of this concept. The only substantial difference is regarding the size of the CFRP plate to be molded. Since the specimens from the second batch were thicker than intended, it is reasonable to believe that there was a failure to apply enough pressure. The third plate's area dimensions were reduced to 180mm x 100mm to increase the pressure. The second change was to remove the extraction holes from the core half, as the holes gave no aid in extracting the plate as first intended. Other than this, no changes were made to the mold's design.

In SolidWorks the volume of the CFRP plate was found to be $72.4cm^3$ with an estimated weight of $101.3g$, when assuming a final density of $\rho = 1.4g/cm^3$. When using equation 3.8, the amount of needed fiber reinforcement for the test plate equates to;

$$m_f = 0.6\rho V_{part} = 0.6 * 1.4g/cm^3 * 72.4cm^3 = 60.8g$$

Using equation 3.9, the amount of needed resin for a test plate equates to;

$$m_r = 1.25m_f = 1.25 * 60.8g = 76g$$

The mold was loaded in the same fashion as the first iteration, and wooden blocks were used to distribute the clamping pressure more evenly. As with the previous mold iteration, there were no significant difficulties in the extraction process. With the new mold design, the thickness of the plate was closer to the desired dimension but still a little thicker. However, each respective specimen had decent consistency regarding thickness, as seen from the standard deviation. This suggests that this iteration was quite successful at applying more pressure. However, two of the ten intended samples were lost during water jet cutting.

Table 4.5: The dimensions of the test specimens from the third batch.

Batch 3	**Thickness [mm]**	**Width [mm]**	**Length [mm]**
Sample 1	4.20 ±0.13	14.85	80.85
Sample 2	4.06 ±0.14	14.85	80.07
Sample 3	4.07 ±0.14	14.89	80.62
Sample 4	4.35 ±0.09	14.86	81.82
Sample 5	4.26 ±0.10	14.79	81.78
Sample 6	4.36 ±0.14	14.87	80.50
Sample 7	4.07 ±0.16	14.86	81.35
Sample 8	4.04 ±0.15	14.87	81.44
AVERAGE	**4.18 ±0.18**	**14.86**	**81.05**

Table 4.6: The mass and average density of the batches.

	SolidWorks Mass	**Final Mass**	**Average Density**
Batch 1	89.0g	88.4g	1.35 ±0.036$g/cm3$
Batch 2	132.5g	159.5g	1.24 ±0.018$g/cm3$
Batch 3	101.3g	98.7g	1.31 ±0.017$g/cm3$

4.3.4 Flexural Test Set-up

The main objective of the flexural testing was to obtain the flexural modulus Ef and to use this as input in an Abaqus simulation. In addition, it is desirable to record the peak stress, stress at failure, and the associated failure mode. The machine used for the mechanical testing was an MTS Criterion Model 42 with a 5kN load cell. The fixture consisted of a support module with a span of 60mm and a load module with a span of 20mm. The loading rate was defined as a movement of the machine crosshead by 2mm/min.

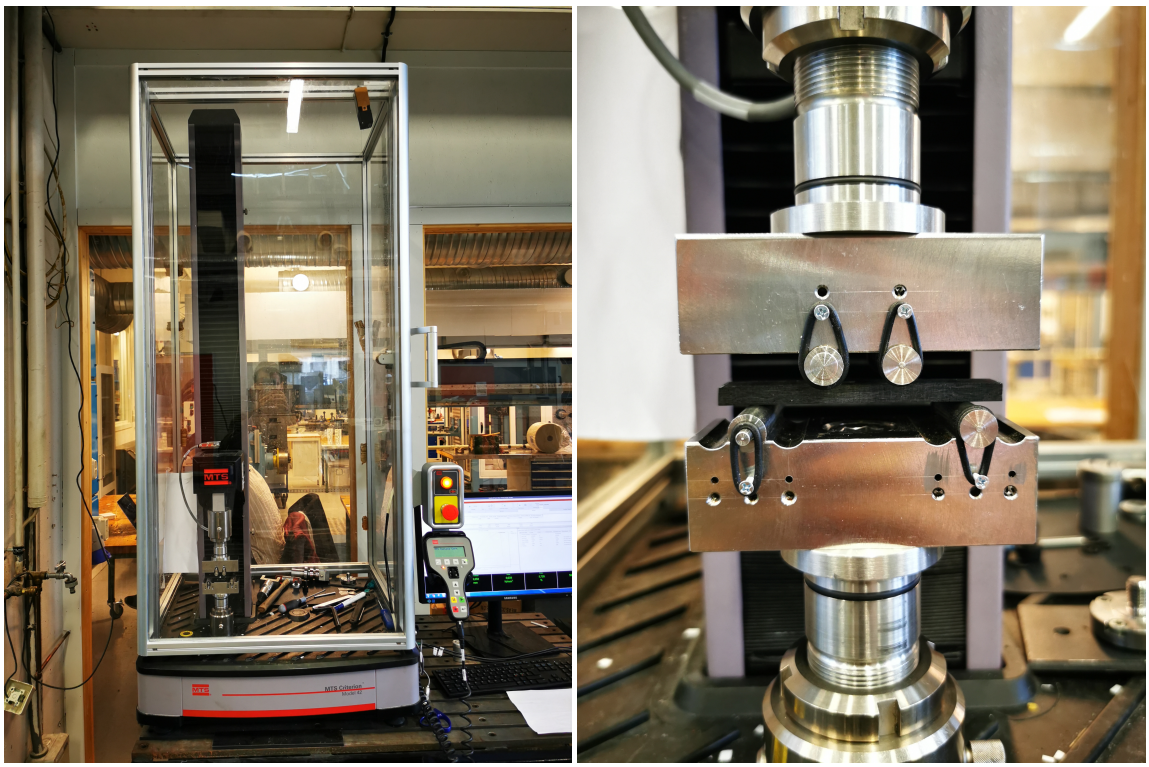

(a) The MTS machine used for material testing.

(b) The modules used for flexural testing.

Figure 4.8: The flexural test setup.

Table 4.7: Information about the flexural test setup.

Test Method	**4-Point Flexural Test**
Machine	MTS Criterion Model 42 5kN
Driving mechanism	Electromechanical
Support roller dimension	5 mm
Load roller dimension	5 mm
Support span	60 mm
Load span	20 mm
Specimen overhang	10 mm
Test speed	2 mm/min
Sampling rate	10 Hz
Sample length	80 mm

4.4 Material Test Results

Material testing was conducted to determine the elastic modulus and strength of the forged CFRP composite material and to use this value further in mechanical simulations to determine if the material is fit for structural hydrofoil parts. Three different batches were tested, each with slight variations, to gain insight into the significance of fiber length and material batch manufacturing. The samples from the first batch were made from 25mm fibers and had an average density of 1.35g/cm3. The samples from the second batch were made from 12mm fibers and had an average density of 1.24g/cm3. The samples from the last batch were also made from 12mm fibers but had an average density of 1.31g/cm3.

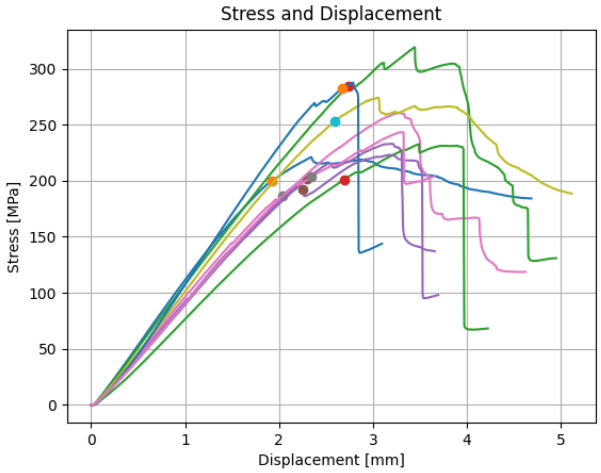

Figure 4.9: Stress-displacement results for samples in the first batch.

The specimens from the first batch were observed to be quite ductile, and all the specimens began to deviate substantially from linear-elastic behavior before reaching their ultimate strength. These specimens also tend to show behavior in correlation with gradual fracture propagation, as seen by the jagged nature of the stress-displacement curves. Since it is not apparent exactly where on the curve fracture commences, an off-set yield criterion was used to generalize the onset of fracture and hence the yield strength of the samples. There also seems to be little consistency in elastic modulus and stiffness among the samples. The cross-head displacement is generally between 1.9mm and 2.8mm at the yield criterion but also close to 4mm for ultimate failure in some specimens.

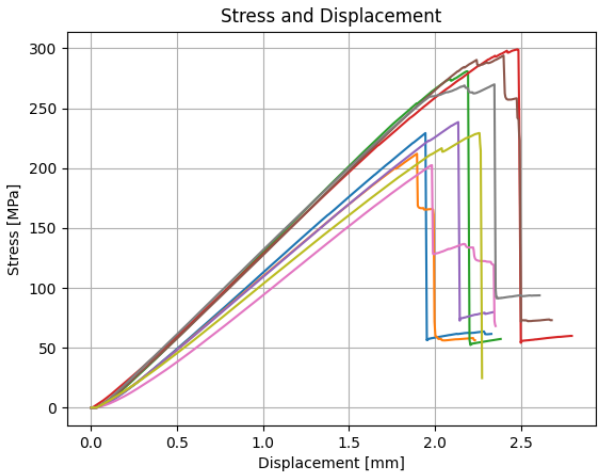

Figure 4.10: Stress-displacement results for samples in the second batch.

On the contrary, the specimens from the second batch were observed to be brittle. The behavior was approximately linear elastic until sudden failure for all the specimens. The trend clearly shows that fracture occurs abruptly following a drastic reduction in strength. For this batch, it can be approximated that the onset of fracture occurs close to the ultimate failure stress. Hence max stress is used as the criterion of failure for these samples. The four strongest samples seem to have a large correlation between elastic modulus and some variation in strength. In comparison, the weaker samples seem to show more variability in elastic modulus but about the same variation in strength as the stronger samples. The cross-head displacement is generally between 1.9mm and 2.5mm, suggesting that the first batch is tougher and capable of enduring more strain than the second batch.

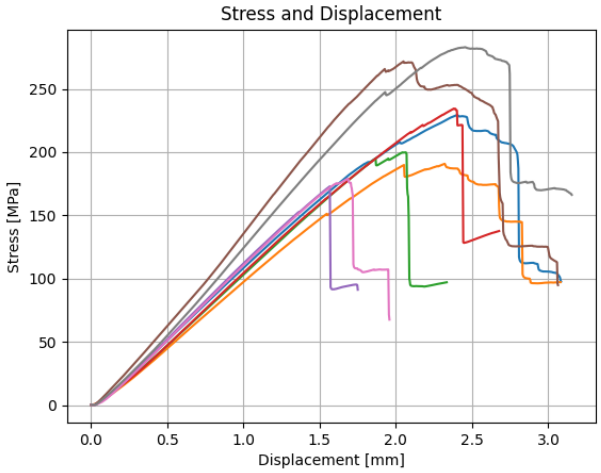

Figure 4.11: Stress-displacement results for samples in the third batch.

The third batch of specimens' responses seemingly falls between the first and second batch. The stress-displacement curve is less rounded than the first batch but more rounded than the second batch. Regarding failure, there seem to be quite significant variations between the samples. About half the samples fail abruptly, while the other half show more ductile behavior. In general, there does not seem to be a substantial amount of yielding before fracture; hence, the maximum stress is used as the failure criterion for the samples, as with the second batch. The elastic modulus seems to be relatively consistent between the weaker samples but with significant variations in strength. The stronger samples, however, have a substantially larger elastic modulus. There are large variations in cross-head displacement at ultimate failure compared with the two other batches, indicating more variability.

From the strength values of the individual test specimens in each batch, the respective characteristic strength of each batch was computed. The characteristic strength is a conservative and statistically determined strength value based on the strength of the sample pool. The characteristic strength represents the load at which only 5% of the samples will fail. In other words, the confidence is that 95% of random material samples will be stronger than this value. The characteristic strength is based on the sample mean, standard deviation, and z-value, which represents the degree of confidence. In the case of 95% confidence the z-value = 1.645 and in the case of 97.5% confidence the z-value = 1.960. The characteristic strength is calculated with the following equation;

$$p_{0.50} = Mean - 1.645SD \tag{4.14}$$

In this relationship, the characteristic strength is based on the variability of the population. The characteristic strength will be low if the variability and hence the standard deviation is large. For materials with extensive heterogeneity or inherently brittle materials, there may be a large scatter between the measurements, which can statistically lead to unreasonably low or even negative characteristic strength values. Therefore, evaluating the results analytically and not just by statistical means is crucial [26].

The following tables show the normal distribution of strength for each of the batches with 95% and 97.5% confidence bounds. Source code inspired by [26].

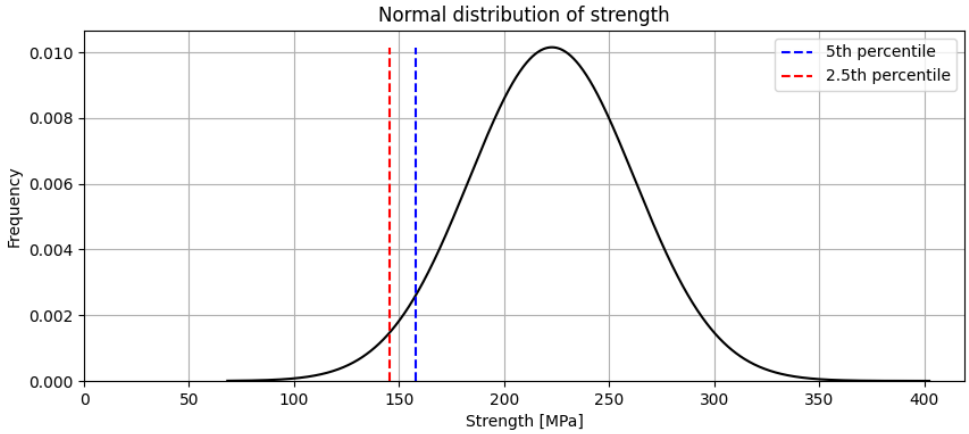

Figure 4.12: Normal distribution of strength for the batch 1 samples. The blue line shows the 5th percentile, and the red line shows the 2.5th percentile.

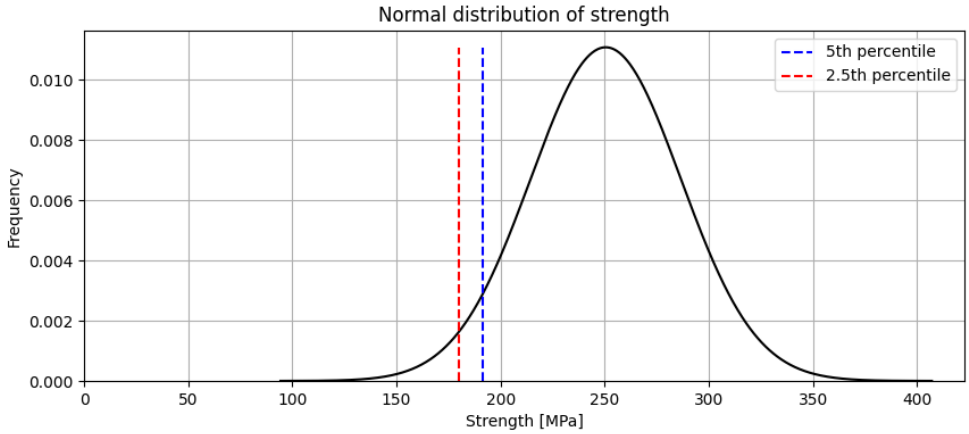

Figure 4.13: Normal distribution of strength for the batch 2 samples. The blue line shows the 5th percentile, and the red line shows the 2.5th percentile.

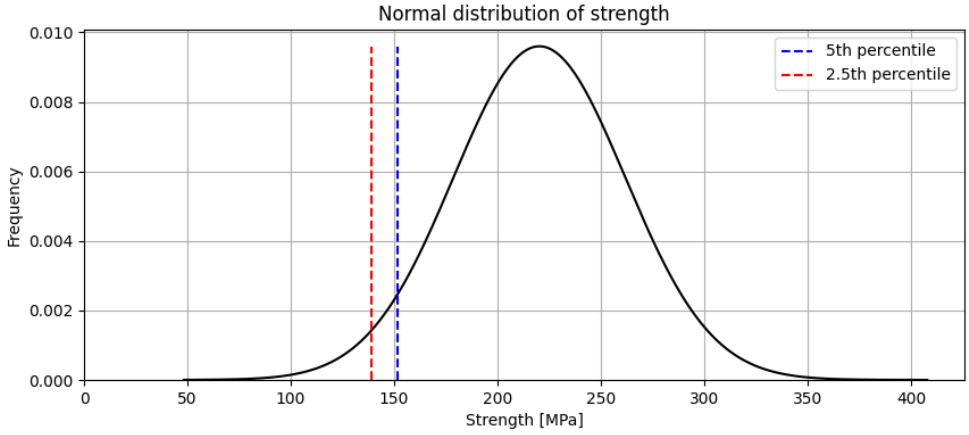

Figure 4.14: Normal distribution of strength for the batch 3 samples. The blue line shows the 5th percentile, and the red line shows the 2.5th percentile.

The analysis of the elastic modulus is based on the mean value rather than a characteristic value. The following tables give the mean value of the elastic modulus along with the standard deviations for each batch. Source code inspired by [26].

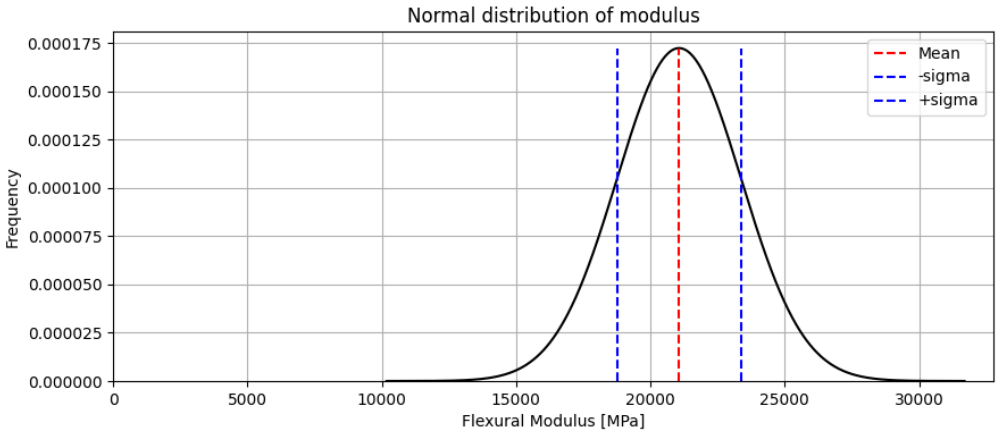

Figure 4.15: Normal distribution of elastic modulus for the batch 1 samples. The blue lines show the standard deviation, and the red line shows the mean value.

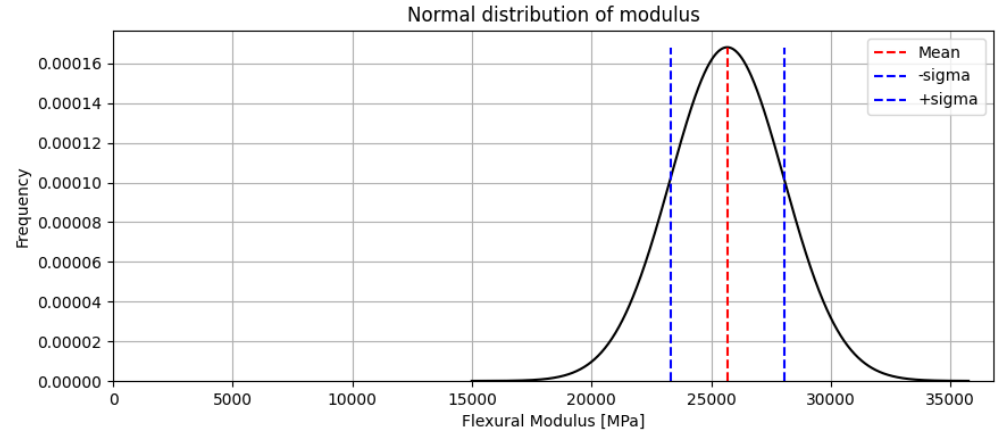

Figure 4.16: Normal distribution of elastic modulus for the batch 2 samples. The blue lines show the standard deviation, and the red line shows the mean value.

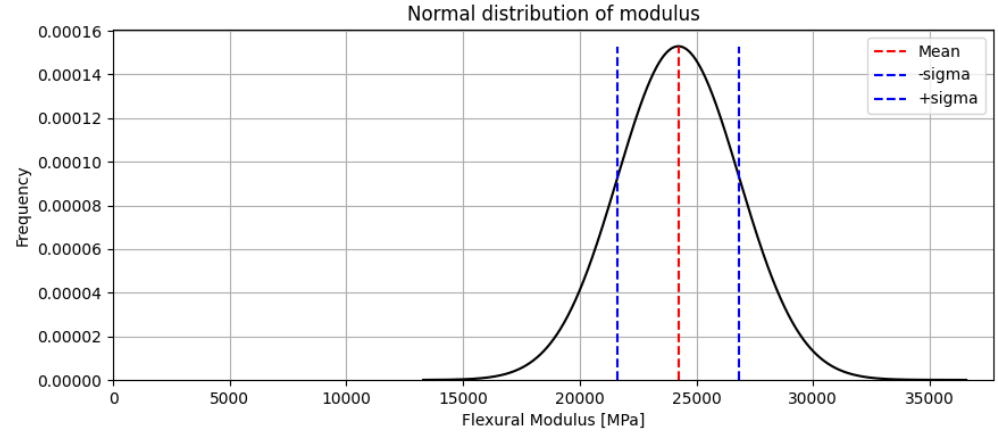

Figure 4.17: Normal distribution of elastic modulus for the batch 3 samples. The blue lines show the standard deviation, and the red line shows the mean value.

The data from the material testing was analysed and summarized in table 4.8 containing strength parameters and table 4.9 containing modulus parameters. From the strength table, it is observed that batch 2 has the highest mean strength. Batch 1 and 3 have about the same mean strength, which is significantly lower than the mean of batch 2. The standard deviations are comparable between all the batches, but batch 2 has slightly less variability. It then follows that the coefficient of variation (COV) is less for batch 2. Regarding the characteristic strength at the 5th percentile, batch 2 is significantly stronger than the others. Batch 1 also has slightly better characteristic strength than batch 3. Hence the characteristic strength of batch 1 is 4.1% stronger than batch 3, and batch 2 is 26.0% stronger than batch 3.

Table 4.8: Strength statistics for all three batches.

Strength	**Batch 1**	**Batch 2**	**Batch 3**
Min [MPa]	186.16	202.43	172.95
Max [MPa]	284.44	299.05	283.00
Mean [MPa]	222.71	250.52	220.16
Standard deviation [MPa]	39.30	36.02	41.56
COV [%]	17.64	14.38	18.88
5th Percentile [MPa]	158.07	191.27	151.79
2.5th Percentile [MPa]	145.69	179.92	138.70

The modulus table shows that batch 2 has the highest mean elastic modulus, closely followed by batch 3. Batch 1 has, however, a substantially lower mean modulus than the other two. The standard deviations are comparable between all the batches, but batch 3 has a slightly higher standard deviation. The coefficient of variation is hence also comparable between all the batches, with batch 3 having the lowest COV. In the case of the elastic modulus, we are more concerned with the mean value rather than a characteristic value. Hence the values for the standard deviation $\pm\sigma$ are reported in table 4.9 rather than percentile values. Regarding the mean elastic modulus, batch 3 is 15.0% more rigid than batch 1, while batch 2 is 22% more rigid than batch 1.

Table 4.9: Elastic modulus statistics for all three batches.

Elastic Modulus	**Batch 1**	**Batch 2**	**Batch 3**
Min [MPa]	17122.33	22111.49	21120.25
Max [MPa]	24748.57	28639.19	28738.33
Mean [MPa]	21067.61	25670.92	24227.44
Standard deviation [MPa]	2313.95	2372.73	2608.43
COV [%]	10.98	9.24	10.77
Mean - σ	18753.66	23298.19	21619.01
Mean + σ	23381.56	28043.66	26835.87

4.5 Discussion of the Obtained Properties

From the results tables, it is clear that the specimens in batch 2 have superior mechanical properties compared to the other material batches both in terms of strength and stiffness. It is also evident that even though the constituents of the batches are the same, the resulting mechanical properties and material behaviors are quite different. It is important to note that even though the constituents of all the batches are the same, it is not meaningful to compare them as the same material. Instead, this study should discuss how different parameters influence the resulting properties of the material and then how to use this knowledge to create a forged CFRP material with mechanical properties suitable for a given application.

From the results, it is clear that there, in general are significant variations in the resulting properties of the CFRP material at different locations. This is likely due to the differences in local composition on a macro-scale. Between different locations, there will be variations in local fiber orientation and local fiber volume fraction, as seen from the density variation between the samples in a batch. There will also be regions with resin-dominated areas that create boundaries between the fiber tow areas. It can be hypothesized that fracture likely initiates at resin boundaries between carbon tows at the tensile side of the specimens during bending.

With this hypothesis of resin-rich boundaries in mind, it makes sense that the pre-mixed specimens show better strength and stiffness properties. When pre-mixing fiber and resin, the fibers become more evenly distributed in the matrix and lose more of the initial tow structure. This results in a material with more consistency and less variation between different sections in the material. Hence the resulting forged CFRP material is more homogeneous when viewed from a macro-scale. When the material is more homogeneous, there will be a more favorable load sharing between fibers and matrix, analogous to springs connected in parallel. On the contrary, when the fibers are not pre-mixed, they maintain more of their initial tow structure. The tows can then be separated by matrix at specific locations where the stiffness will be more analogous with springs in series.

This load-sharing hypothesis can support the fact that the pre-mixed material with shorter fibers has the greatest elastic modulus. The longer fiber wet-layed CFRP material will be the least homogeneous, giving rise to more substantial matrix boundaries, and hence have the lowest elastic modulus but is able to endure more strain, as seen from the results. The material created in batch 3 was also made with a wet layup but with a shorter fiber length. This material is also substantially stiffer than the material in batch 1, which might suggest that shorter fibers are more favorable for stiffness when creating forged CFRP. However, this was the least strong material with the most inconsistencies and variabilities, indicating that it might be the least homogenous.

Interestingly, the forged CFRP material from batch 2 has the lowest density and, thereby, the lowest volume fraction of fibers. It is hence counterintuitive that this material should have the greatest elastic modulus when viewed with the theory of composite micromechanics explained in Chapter 3, as the elastic modulus should increase with fiber volume fraction and material density. This theory is, however, intended for the analysis of UD laminas. It shows, however, that material homogeneity seemingly has a more significant impact on the resulting elastic modulus than the fiber volume fraction in the case of forged CFRP with the manufacturing equipment available in this study.

Regarding strength, the second batch is also the best. The strength values between batch 1 and batch 3 are seemingly quite comparable. However, due to the ductile nature of the first batch, a yield criterion was used to determine the strength, while for the third batch, maximum strength at failure was used. If maximum strength had been used as the failure criterion for the first batch as well, then this would be substantially stronger than batch 3. Again this supports the argument that even though the constituents are of the same material, the resulting composite properties are highly different. The longer fibers make for a ductile yet tough material compared to the shorter fiber materials that are of a more brittle nature. Also, it can be noted that brittleness seems to increase with decreasing fiber volume fraction, but it is hard to conclude that this is the case due to a large number of other variables between the material batches.

All the resulting material properties must be seen through the lens of the manufacturing equipment used to make samples. The molds used in this investigation are rudimentary compared to professional molds for commercial applications. As with the samples, the molds also have local inconsistencies. This is an inherent problem when creating engineering parts with personal 3D printers. It is difficult to control the outcome of tolerances, dimensions, and the effect of print warping, especially on larger printed parts. This will, in turn, affect the quality and tolerances of the test specimens. This was seen by the variation of thickness in the samples. In all the batches, the specimens are consistently thicker at one end than at the other end. Unevenness in the molds can also result in differences in locally applied molding pressure and hence differences in local material density.

A more consistent and controlled manufacturing process can likely reduce the significant variations in mechanical properties between the samples. This can be achieved through stiffer, more solid molds, e.g., made from steel or aluminum. A gauged hydraulic press would also be beneficial as it would allow the ability to control the applied pressure and ensure that it is even between batches. This, in turn, will give tighter tolerances and more consistent dimensions. With controllable hydraulic pressure and stiff molds, the density of the parts can reliably be ensured, and hence the desired fiber volume fraction be achieved.

It is difficult to predict the potential properties of forged CFRP manufactured under more controlled conditions. It is, however, fair to assume better properties and more material consistency with more sophisticated manufacturing equipment. When studying batch 3, it is clear that the potential strength and stiffness are higher than what has now been statistically determined. When looking only at the four strongest samples, the modulus is highly consistent and averages about 28000MPa. It should therefore be possible to achieve such properties more consistently with better means of production. Hypothetically if all the samples in this batch were consistently showing properties in this range, then the characteristic strength would also increase significantly since the variation in the data would be less. Using a random number generator with the lower bound being 270MPa and the upper bound being 300MPa, the characteristic 5th percentile strength of such a scenario equates to 273MPa. This is substantially more than what was achieved in this investigation. It supports the claim that forged CFRP could be used as a structural material. Further investigation of the fiber volume fraction would also be interesting, as the literature states that this should result in more fiber-dominated mechanical properties. It would also be interesting to obtain properties from longer fiber specimens made through the pre-mixing process to better understand the effect of mixing and fiber length.

Due to the composite fiber-matrix structure of the forged CFRP, modeling is not as straightforward as with isotropic materials. In addition, due to the random fiber orientations, there is even a lack of analytical methods for determining the mechanical properties of such materials. For parts made with features of thin cross-sections, the fiber direction will mainly be in the plane/orientation, which is normal to the direction of the applied pressure. This is quite evident when looking at the structure of the specimens. For thicker parts, the fiber direction will be in the plane/orientation, which is normal to the direction of the applied pressure at the surfaces, while further from the surface, the fibers will be free to assume other orientations as well. The possible fiber orientations away from the surfaces will also be influenced by the relationship between the fiber length and part section thickness. Hence thin structures can assumingly be regarded as transversely isotropic with axial symmetry about an axis that coincides with the direction of the applied pressure. Thicker sections can likely largely be modeled as isotropic, at least when bulk and with part cross-sections that are much larger than the fiber length [11].

The simplest way to model forged CFRP is to assume that the material is homogeneous and isotropic. These assumptions are inherently wrong, but the model can still yield valuable insights into the general stiffness response of a part subjected to external loads. The isotropic assumption does not consider the fiber orientations and material flow in the parts due to compression molding, as the fibers will tend to align with mold surfaces. It also neglects the effect of lamination. Hence, at least for relatively thin parts, the through-thickness properties are different from the in-plane properties, and the stress results will not be meaningful. With this in mind, the most useful application of isotropic modeling will be to analyze thin structures with in-plane loading [11].

A more accurate model can be achieved if it is assumed that the material is transversely isotropic. With this method, the material can be modeled with in-plane properties where there is a high degree of fiber alignment and with out-of-plane properties normal to the fiber alignments. Hence the material can be viewed as having a locally quasi-isotropic layup structure due to the random fiber orientations in the plane. The out-of-plane properties can be viewed as matrix-dominated transverse properties due to the resemblance to a traditional laminate on a micro-scale. It is not a perfect model, but it better predicts the out-of-plane stiffness and strengths compared with an isotropic model. The model is mainly acceptable for thin structures as the fiber alignment is more prominent. However, for thicker parts or parts of a more complex shape, the fiber alignments will be less obvious [11].

4.6 Conclusion of Testing

In this chapter, three batches of test specimens were created to determine the elastic modulus and strength of forged CFRP through 4-point flexural testing. The material created in batch 2 showed the best mechanical properties and consistency between samples. In the next chapter, the mean elastic modulus and the 5th percentile characteristic strength of batch 2 will be used in a finite element analysis. It is hypothesized that this material can achieve even better mechanical performance with better manufacturing tools. Using the obtained properties will, however, yield a conservative analysis. In addition, the second batch was made by pre-mixing the fiber reinforcement and resin. This has an added benefit from a manufacturing point of view. When making several parts, it saves time to prepare a larger batch of a mixed compound and then fill several molds rather than conducting the layup procedure as done in the two other test batches. This will also result in more consistency between parts. Hence, this technique will be used when prototyping the final parts.

Chapter 5

FEA & Prototype Development

5.1 Introduction

Computer Aided Engineering (CAE) is a generalized set of simulation-based tools for verifying and optimizing various engineering problems. One of these tools is Finite Element Analysis (FEA), a technique for simulating physical phenomena such as mechanical loading, heat transfer, fluid dynamics, and multiphysics problems. By using FEA, the need for time-consuming physical prototyping and testing can be reduced as the simulations provide information about the system's response similar to what is to be expected in real-world scenarios. FEA is based on numerical methods for solving mathematical problems, which is applied through the Finite Element Method (FEM) [24].

The design concept proposed earlier in Chapter 3 will be investigated in this chapter. It is desired to verify that this concept is a viable solution as a structural hydrofoil design with the forged CFRP material obtained in Chapter 4. The overall FEA process consists of three different stages. First is the pre-processing stage, where part geometries, physical properties, interactions, and the external load case will be defined. This stage also includes the often iterative process of creating the mesh. Next is the solution stage, where an appropriate mathematical formulation that represents the physical problem is defined and solved by the computer. The last stage is the post-processing stage, where the results are presented for review [30]. If it is concluded that the design does not meet the product requirements, then changes can be made either to the design geometry or physical properties, i.e., the selected materials, in order to achieve a functional product. In the end, physical prototypes of the proposed design will be developed.

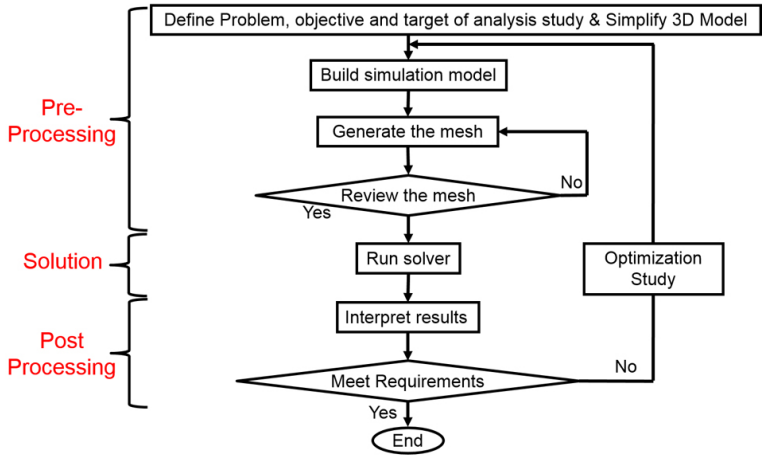

Figure 5.1: A flowchart illustrating the process of conducting a finite element analysis.

5.2 Theory - The Load Case

A hydrofoil is subjected to dynamic and changing loading conditions. As a design constraint, it is desired to analyze the structure at a maximum static load case. In this analysis, the possible loads are constrained by the geometry of the hydrofoil assembly. It is only possible that the load is applied on the board by the rider, and the most severe load case during regular operation happens when the CG of the rider is located at the extremities of the board furthest away from the mast. The CG of the rider is the furthest forward on the board at high speed. Assuming a standard board width of 600mm, the most extensive moments will occur if the rider's weight is applied at the very edge of the board. This scenario could be encountered during a powerful carve at high speed. It is a rather extreme load case that likely will not occur, but it is a useful scenario for a conservative analysis with large forces. By idealizing this scenario into a static load case, it can be analyzed using free body diagrams.

The forces and moments need to be balanced when assuming constant velocity and no acceleration. Assuming a rider weight of 750N applied as a point load located 250mm forward of the front wing as discussed in Chapter 2 and half a board width from the center axis will give rise to the following reaction forces and moments in figure **??** 5.2. The boundary conditions can be determined by analyzing the free body diagram of the hydrofoil. When assuming constant lift, there will be no change in AoA or motion in the y-direction; hence U2 is constrained at both ends of the fuselage. The way that best captures the bending of the fuselage is by modeling it as a simply supported beam; hence U1 is constrained only at the front of the fuselage, while it is free to move in this U1 at the rear end. It is necessary to constrain U3 at both ends of the fuselage to prevent rigid body motion in the form of translation in the z-direction or rotation about the y-axis. It is necessary to constrain UR1 at some node of the structure to prevent rigid body motion in the form of rotation about the x-axis. This can be done in several ways, giving rise to different reaction forces and moments. It is decided that this DOF will be constrained at both ends of the fuselage due to the resistance of the wings that should keep the hydrofoil roll stable.

(a) Beam model of the hydrofoil showing the load and reaction forces in the xy-plane side view.

(b) Beam model of the hydrofoil showing the load and reaction forces in the yz-plane front view.

Figure 5.2: Free body diagram representations of the hydrofoil.

Table 5.1: The resulting maximum moments, shear force, and axial force in the different parts.

	Moment	**Shear Force**	**Axial Force**
Mounting Plate	400Nm bending	750N	N/A
Fuselage	190Nm bending / 230Nm torque	1020N	N/A
Mast	400Nm bending	N/A	750N

The following simplified structural models are created, including the associated moment, shear, and axial diagrams when using these constraints. It is observable that the most extensive bending moment will occur in the mounting plate at the connection between the mast and the board and along the mast, which experiences a constant bending moment in this model. A significant moment also occurs at the connection between the mast and the fuselage. The fuselage is also subjected to torsion due to the offset in the rider's center of gravity with the x-axis. The most significant shear force is experienced along the front section of the fuselage, forward of the mast. The board does also experience a significant shear force, but this part is outside the scope of this thesis and will be regarded as infinitely stiff from here on. The mast is the only component that will experience an axial force equivalent to the rider's weight. The values of the forces and moments are summarized in 5.1. This is a 3D structural problem that has been divided by superposition for analysis, as seen in the figures. Hence the resulting moments and forces in the table are the total when combining the superposition. In side view, the y-coordinate of the load is neglected, and in front view, the x-coordinate of the load is neglected.

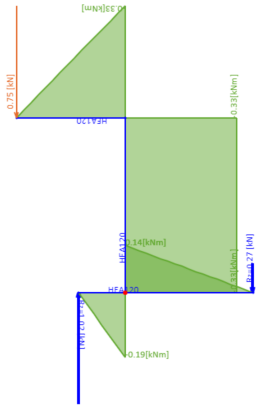

(a) Moment diagrams in side view.

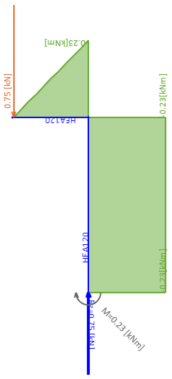

(b) Moment diagrams in front view.

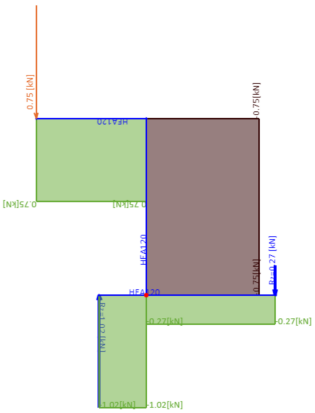

(a) Shear and axial diagrams in side view.

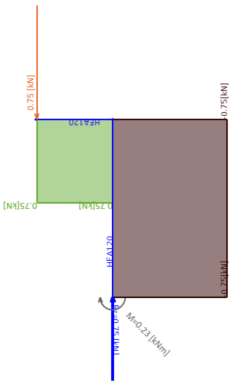

(b) Shear and axial diagrams in front view.

Figure 5.4: Diagrams of the internal forces in the structure of the hydrofoil.

5.3 Method - Abaqus/CAE Simulations

5.3.1 Objective

In this chapter, the main objective is to investigate if the proposed design concept in Chapter 3 with the properties of forged CFRP concluded in Chapter 4 is a viable choice as a structural hydrofoil design. For comparison, the structural concept will also be simulated with the other more common materials, glass fiber reinforced polyamide, BMC, and aluminum 6061. The simplified models indicate the reaction forces in the structure, but it is desirable to conduct a finite element analysis to gain a deeper insight into the deformations and stresses of the design. The structure is quite complex, consisting of geometry that needs to be partitioned in order to be adequately meshed. In addition, the structure consists of several different material sections. All these sections will need to interact the right way and be meshed in such a manner that the model solves with representative results. Of primary interest is verifying that the structure's stresses are within acceptable limits, so mechanical failure will not occur. It is also of interest to check the deformation, as the structural parts are desired to have adequate stiffness.

5.3.2 Parts

The model geometry to be analyzed was created in SolidWorks and was then imported into Abaqus. The imported model consists of 4 parts joined in an assembly.

- The mounting plate: Modeled with forged CFRP; polyamide/glass fiber; BMC; aluminum 6061
- The mast core: Modeled with PVC foam
- The mast skin: Modeled with a carbon/epoxy laminate
- The fuselage: Modeled with forged CFRP; polyamide/glass fiber; BMC; aluminum 6061

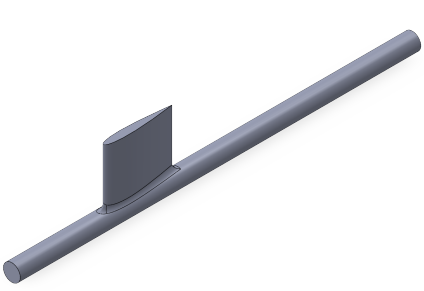

(a) SolidWorks model of the fuselage.

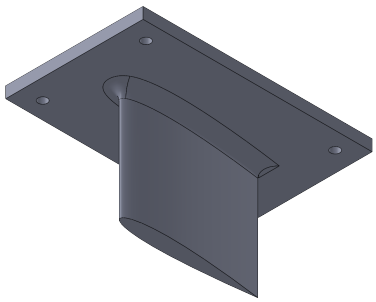

(b) SolidWorks model of the mounting plate.

(c) SolidWorks model of the mast core.

(d) SolidWorks model of the mast fiber skin.

Figure 5.5: Solidworks models.

The concept behind the design is that the mounting plate, mast core, and fuselage are manufactured individually and then joined together by a carbon epoxy laminate as a skin. The mounting plate and fuselage incorporate a flange with the same NACA profile as the mast so that the skin can overlap effortlessly. The parts were exported from SolidWorks as STEP214-files and imported into Abaqus CAE. The mounting plate, fuselage, and mast core were imported as 3D deformable solids, while the mast skin was imported as a 3D deformable shell.

5.3.3 Properties

In the ***"Properties"*** module of Abaqus, the mechanical properties of the various parts were defined. In this analysis, a total of 5 different materials were defined; four isotropic materials and one composite lamina. Since Aluminium and BMC have almost exactly the same elastic modulus, the simulated responses will be about the same. Hence one shared model can be used for these two materials. The mechanical properties are summarized in table 5.2. Next different sections were defined and assigned. One section was defined for each of the parts in the model. The mounting plate, the mast core, and the fuselage are all defined as Solid, Homogeneous sections with the related materials for the respective parts. The mast skin was defined as a composite layup where all the plies have the UD/Epoxy mechanical properties.

The layup was defined as $[45/-45/0]_3$ with a ply thickness of 0.3mm. The laminate coordinate system was defined as having the normal direction, normal to the surface of the mast. The 1-direction was defined as the span-wise direction along the mast length; hence, the 2-direction was defined as the chord-wise direction along the surface of the profile. Since the composite layup is a skin surrounding a foam core, it can, in a sense, be regarded as a helical and balanced sandwich structure. The rationale behind this layup choice is that it closely represents a triaxial, stitched, non-crimp fabric repeated three times. A triaxial fabric has the benefits of providing both stiffness in the longitudinal direction and torsional stiffness. In addition, a triaxial fabric is more economical compared to an equivalent layup of UD plies in regards to manufacturing since the layer count is reduced by a factor of 3.

Abaqus does not incorporate built-in units. In this model, the SI(mm) unit convention is chosen, and all numeric values are consistent with this system.

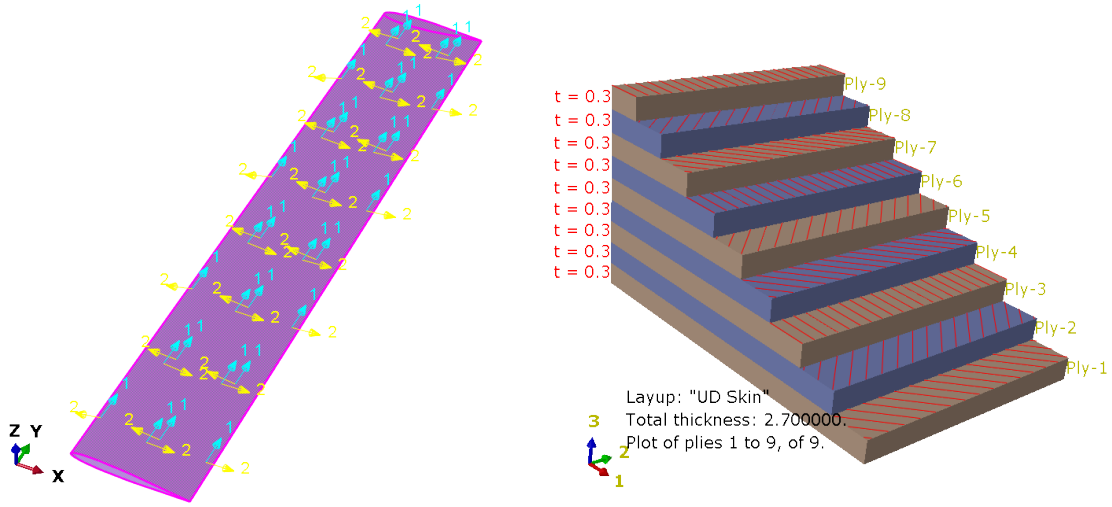

(a) The local coordinate system of the 0°plies with the longitudinal running the length of the mast and the transverse direction tangent with the surface.

(b) The directions of the respective plies in the skin laminate.

Figure 5.6: The modeling of the fiber skin laminate.

Table 5.2: The mechanical properties of the materials used in this analysis. The failure stress is given for tensile loading. For UD/Epoxy, the tensile failure stress in the 1-direction, 2-direction, and 12-direction of shear are given, respectively.

Material	**Type**	**E / E1**	**E2**	**nu**	**G12**	**G13**	**G23**	**Failure Stress**
Forged CFRP	Isotropic	25670		0.3				191
Aluminium 6061-T6 [1]	Isotropic	68900		0.33				276
Toray MS-1H BMC [20]	Isotropic	68900		0.33				256
Tecamid GF50 [18]	Isotropic	9000		0.33				115
PVC Foam [16]	Isotropic	75		0.3				1.89
UD / Epoxy [8]	Lamina	135000	10000	0.3	5000	5000	5000	1500/ 50/ 70

5.3.4 Assembly and Interactions

In the ***"Assembly"*** module of Abaqus, the individual parts are joined together in a global coordinate system. In this module, the CAD geometries from the ***"Part"*** module are being referenced into CAE instances in the ***"Assembly"*** module. All the part instances were created with the dependent type. Dependent part instances are pointers to the original part geometries, while independent part instances are copies of the original CAD geometry. By creating independent part instances, it is possible to perform alterations without modifying the original part, such as partitions and virtual topology, but all duplicates of a part in an assembly will have to be meshed individually. The dependent type is chosen since partitions were desired to be made on the original parts and due to gained performance as fewer memory resources are utilized [9].

Since the hydrofoil consists of several parts joined together, it is necessary to define the interactions between them. The idea behind the design concept is that the fiber skin connects the mast core and the flanges of the mounting plate and fuselage into a single component. Hence, a tie constraint was used to connect these parts together. The fiber skin was picked as the master surface, while the mast core and flanges of the mounting plate and fuselage were picked as the slave surface. Three reference points were created where the load and boundary conditions were to be applied. These reference points are connected to surfaces on the model geometry with kinematic coupling. All the degrees of freedom are constrained in the kinematic couplings.

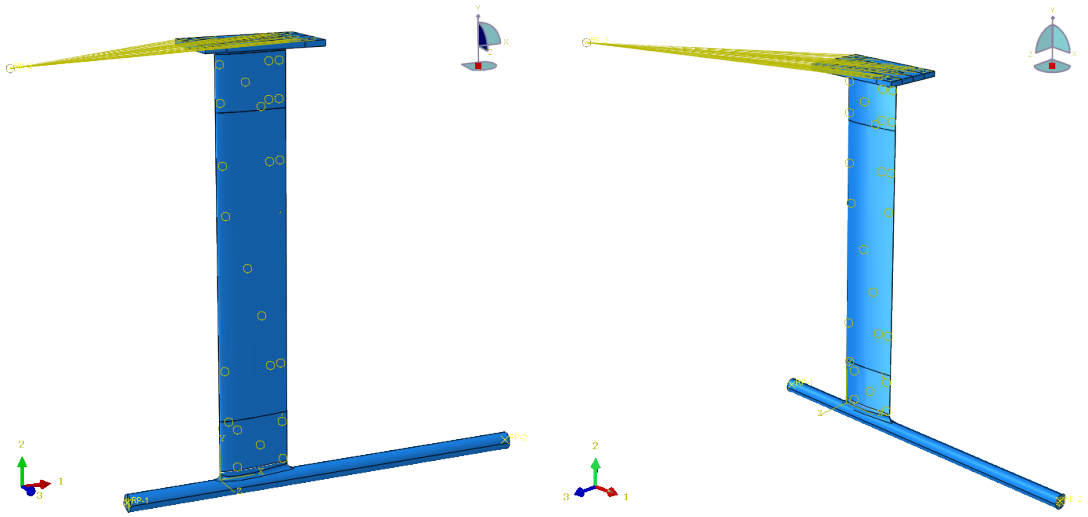

Figure 5.7: Defining the interactions between the parts in the assembly

5.3.5 Steps, Loads and Boundary Conditions

In Abaqus, steps are a convenient way of breaking down a model's loading history into individual segments. By default the step ***"Initial"*** is automatically created by Abaqus. In the case of the described load case for this hydrofoil model, it is only necessary to define one more step in addition to ***"Initial"***. A step of the type ***"Static"***, ***"General"*** was created after ***"Initial"*** to capture the applied load. A step can be broken down into increments to facilitate a non-linear solution path. In this way, a static load can be applied over a series of discrete time intervals rather than linearly over a single interval to help with convergence. In this loading step, the initial increment size was set to 0.2, while the minimum increment size was set to 1E-05 with a maximum of 100 increments. The equation solver uses the Direct method with the Full Newton technique. Since kinematic couplings exist in the model, the solver was set to account for non-linear geometry in the loading step.

In the ***"Load"*** module, the loads and boundary conditions were defined. The load was defined as a concentrated force vector with a magnitude of 750N in the negative y-direction. The load was applied at the reference point RP3, which has a kinematic coupling to the upper surface of the mounting plate. The concentrated force was applied at the load step. Regarding the boundary conditions, they were applied to the reference points RP1 and RP2 that have kinematic couplings to the surfaces at the front and the rear end of the fuselage, respectively. At the front of the fuselage, the constrained degrees of freedom were ***"U1, U2, U3, and UR1"***. At the rear of the fuselage, the constrained degrees of freedom were ***"U2, U3, and UR1"***. The boundary conditions were applied at the initial step and propagated to the load step.

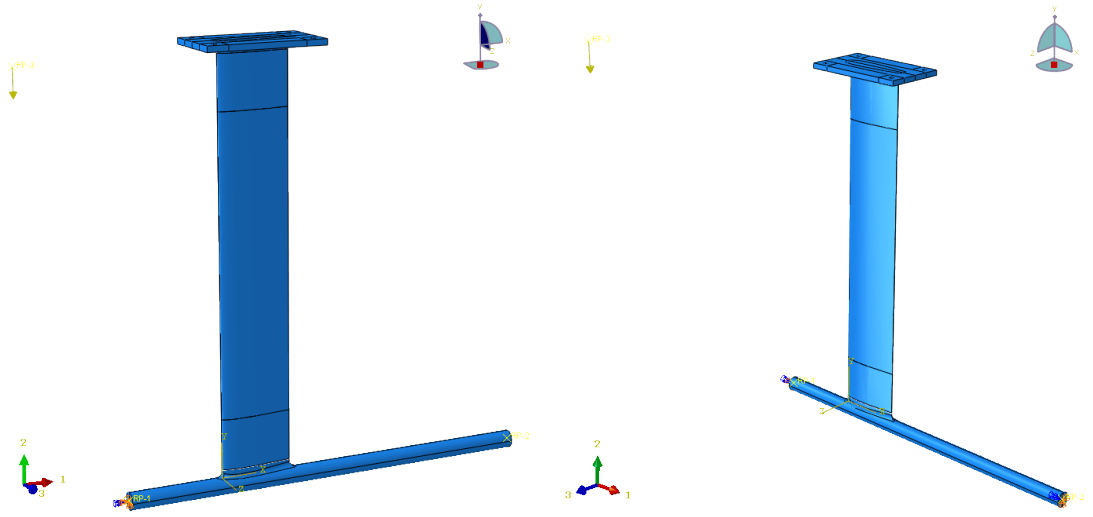

Figure 5.8: Defining the loads and boundary conditions.

5.3.6 Mesh and Partitioning

It is necessary to partition the parts into subdivisions known as cells to create a proper mesh for the model. The geometry of these cells will dictate which elements it is possible to use when meshing. Regarding 3D elements, it is most common to use hexahedral or tetrahedral elements. In general, it is wise to use hexahedral elements as they are less computationally expensive, making the model solve faster (for a given element size). On the other side, tetrahedral elements are geometrically versatile, making the meshing procedure easier to execute; hence, these elements are commonly used in automated meshing algorithms. Simple linear elements will have one node at each corner of the element. It is also possible to utilize quadratic elements that incorporate midpoint nodes in addition to the corner nodes to represent the geometry more accurately.

In Abaqus, the type of elements is identified by a unique code consisting of the element family and the number of nodes. With this classification system, a linear tetrahedral element will have the code C3D4, while a quadratic hexahedral element will have the code C3D20. The FEA solver computes displacements and then forces results at the nodes of the elements. On the contrary, stresses and strains are computed at integration points at the interior of an element. The element shape function interpolates the nodal results to obtain the stresses and strains at the integration points and how these values are represented through the element [17]. Abaqus offers the option to reduce the number of integration points to reduce the solver workload denoted by an R at the end of the element code. Meshing and partitioning is often iterative process to achieve the desired element type. In this model, it is desirable to use hexahedral C3D8R (reduced integration) elements, and the parts will be partitioned in an attempt to achieve this where possible. C3D20R elements would generally provide slightly more accurate results but are deemed too computationally expensive. As a second option, quadratic tetrahedral C3D10 elements will be used in cells with geometry too complex for hexahedral elements. This element type is favored over the linear C3D4 type, as they tend to be overly stiff.

To verify that it is reasonable to use linear hex elements where possible in the model, one job was submitted with linear elements, and one job was submitted with quadratic elements. The goal was to compare the computational time and the differences in stress and deformation results between the jobs. The properties in the model are forged CFRP, PVC foam, and UD fiber/epoxy. The two different meshes generated were defined in accordance with table 5.4 and 5.5. It is clear that the differences in results are minuscule between the element types, while the elapsed time is drastically lower when using linear elements. It is hence deemed favorable to use linear hexahedral elements where possible, as the computational time is more than 300% higher when using the quadratic equivalent.

Table 5.3: The solver time and results corresponding to linear and quadratic elements.

Type	**Wallclock Time [s]**	**Max Mises [MPa]**	**ΔU1 [mm]**	**ΔU2 [mm]**	**ΔU3 [mm]**
Linear	7284	215.469	12.529	69.979	84.087
Quadratic	29523	215.524	12.506	69.847	83.770

Table 5.4: The mesh as defined with mainly linear elements.

Part	**Element type**	**Global seed size**	**Edge seed size**	**Mesh technique**
Fuselage	C3D20R and C3D10	4	N/A	Sweep/ Free
Mounting Plate	C3D8R	4	N/A	Structured
Mast core	C3D8R	4	N/A	Structured
Mast skin	S8R	4	Double bias max: 4	Structured

Table 5.5: The mesh as defined with mainly quadratic elements.

Part	**Element type**	**Global seed size**	**Edge seed size**	**Mesh technique**
Fuselage	C3D20R and C3D10	4	N/A	Sweep/ Free
Mounting Plate	C3D20R	4	N/A	Structured
Mast core	C3D20R	4	N/A	Structured
Mast skin	S8R	4	Double bias max: 4	Structured

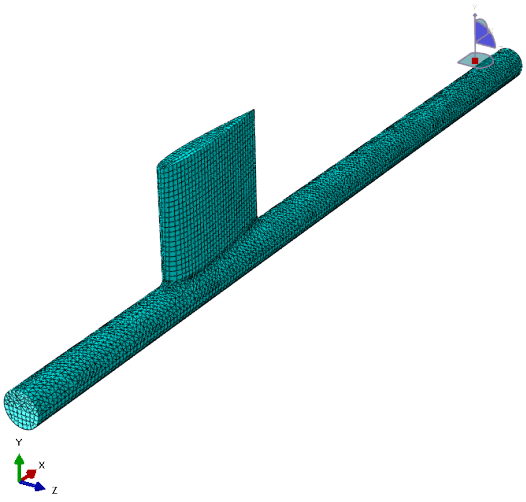

(a) The fuselage mesh.

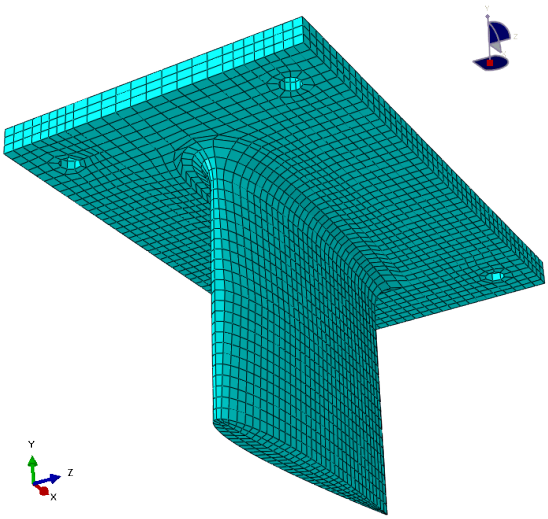

(b) The mounting plate mesh.

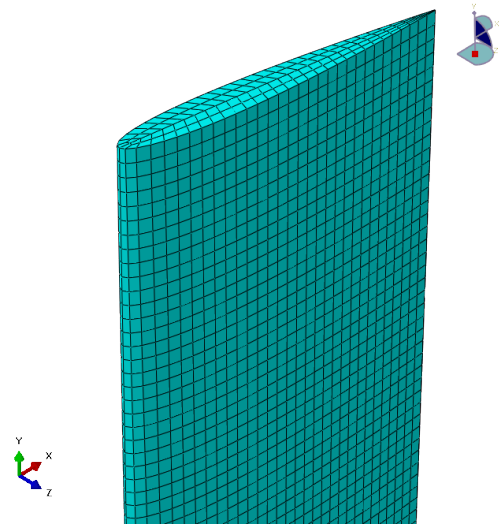

(c) The mast core mesh.

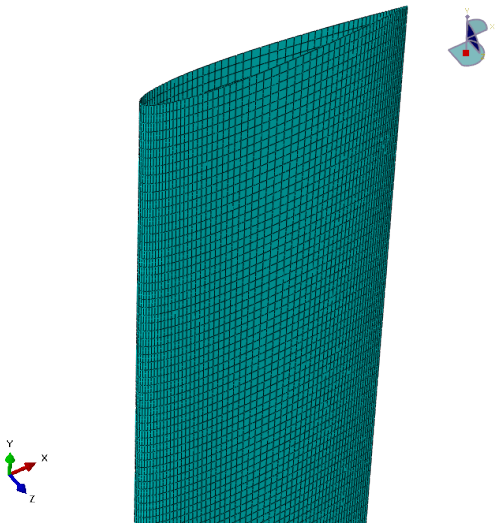

(d) The laminate skin mesh.

Figure 5.9: The parts with the mesh to be used in the analysis are predominantly created with quadratic elements.

5.4 FEA Results and Discussion

5.4.1 Stress Results

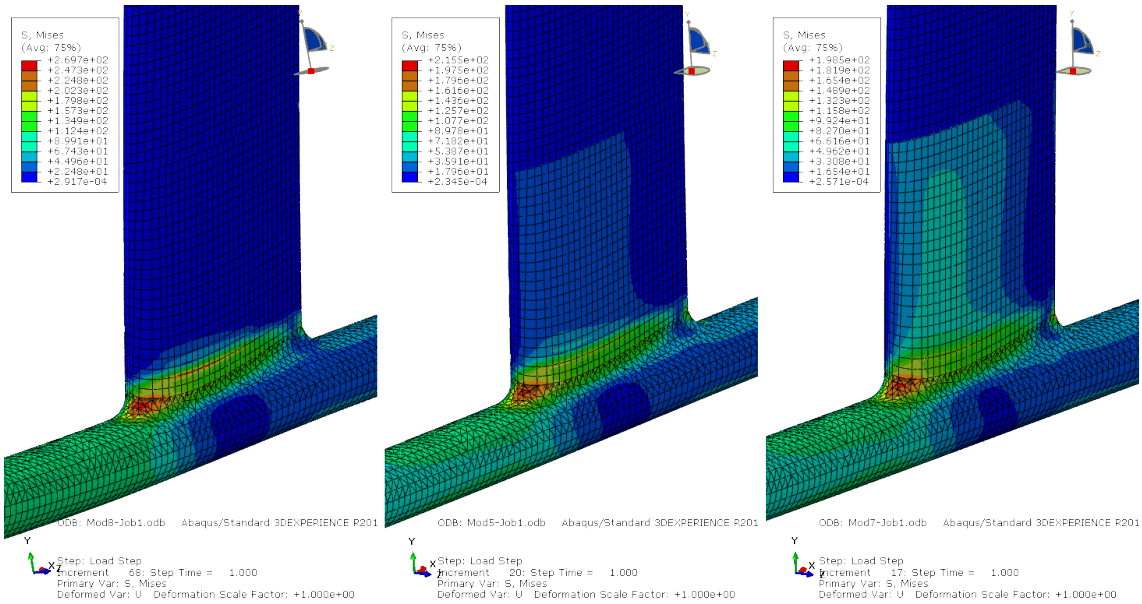

Figure 5.10: The stress distribution at the front of the fuselage flange. From left to right, glass-reinforced polyamide; forged CFRP; aluminum/BMC.

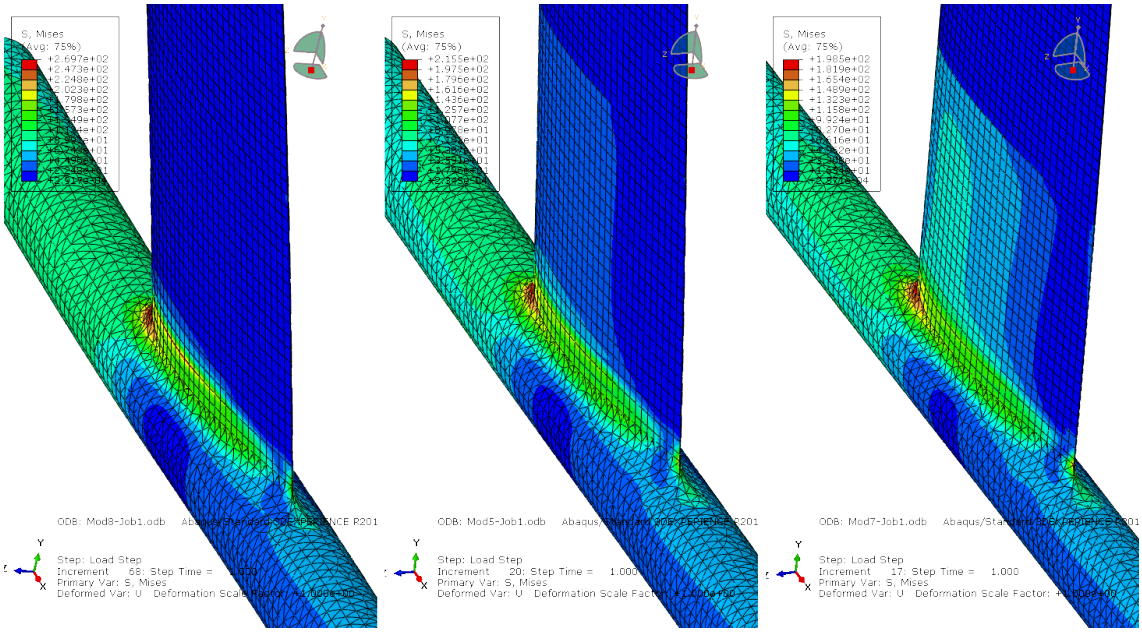

Figure 5.11: The stress distribution at the rear of the fuselage flange. From left to right, glass-reinforced polyamide; forged CFRP; aluminum/BMC.

As expected, stress is concentrated in an area at the front of the flange, where the flange transitions into the fuselage. Here the geometry changes in an internal corner and effectively creates a notch effect. This area is on the compression side. There is also a small stress concentration at the trailing edge of the flange before the fillet with the fuselage. It is to be expected that there should be elevated stresses in this thin, notched area. However, since the elements here are of a poor shape and the area is small and localized, the exact value is hard to determine, and the resulting

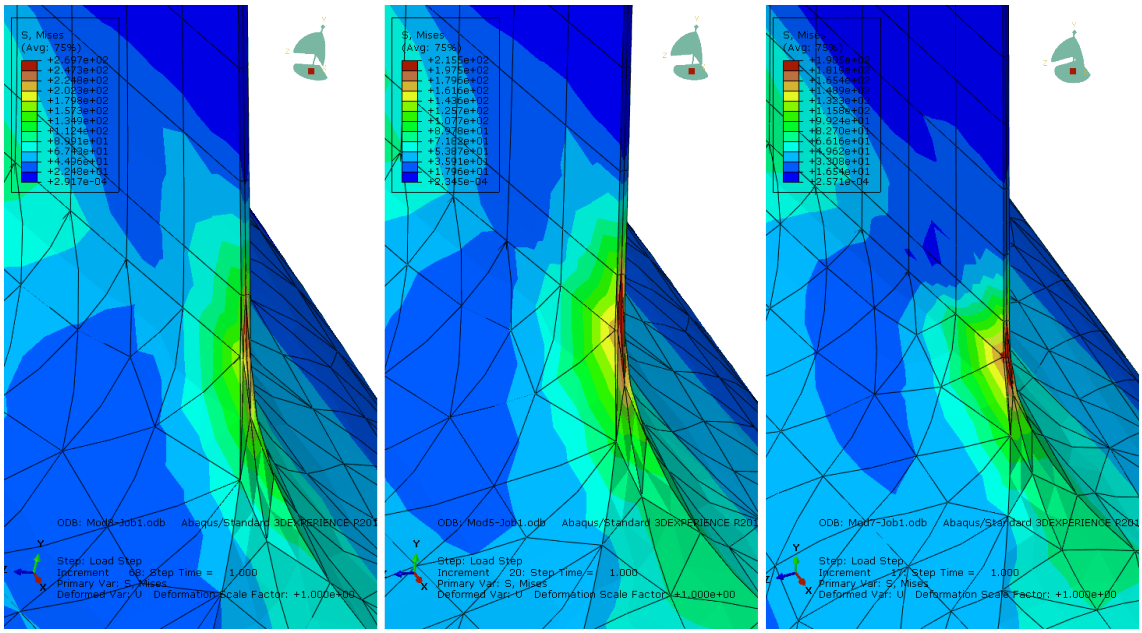

Figure 5.12: The stress concentration at the rear of the fuselage flange. From left to right glass/nylon; forged CFRP; aluminium/BMC.

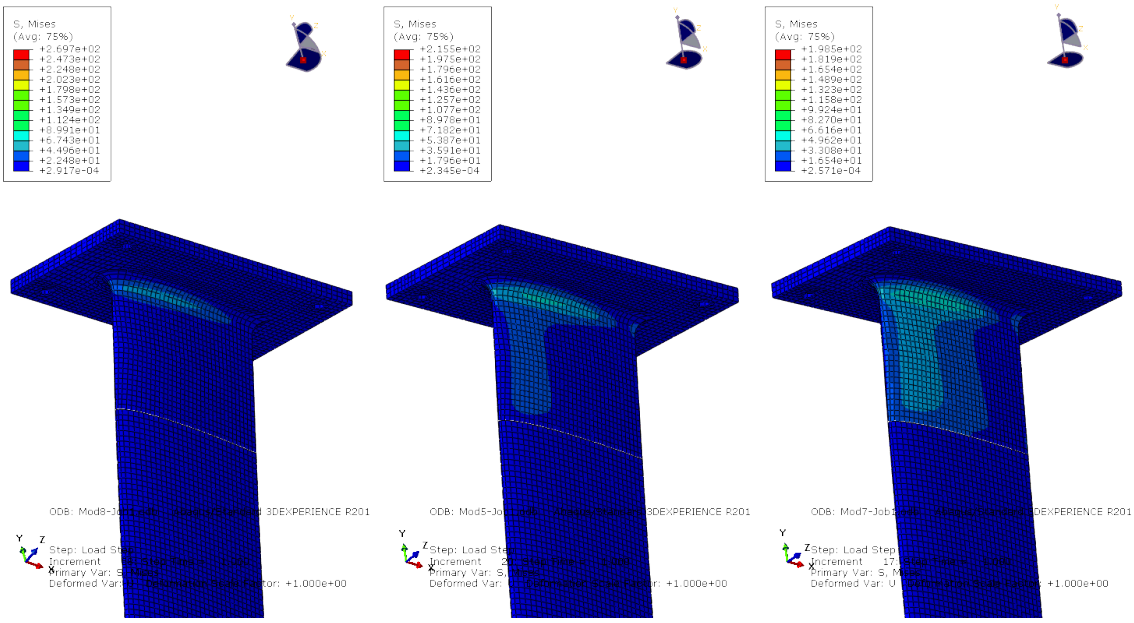

Figure 5.13: The stress distribution at the mounting plate and mast connection. From left to right glass/nylon; forged CFRP; aluminium/BMC.

stress values should be taken with a grain of salt. This region is thin, mainly in tension, and can possibly create the onset of fracture under cyclic fatigue loading. Also consistent with the load case theory is that the fuselage section in front of the mast experiences more stress than the rear part. This is due to the bending moment and the torsion being more significant at the front compared to the rear. Due to torsion, the shear stress will be greater at the surface than at the center of the fuselage cross-section. The results clearly show that the center experiences little stress, and the fuselage could be designed as a tube rather than a rod for weight saving (see figure 5.18). It is also clear that a band of stress is running along the fillet. Not only is this region affected by a change in geometric cross-section, but also an abrupt change in material stiffness since the laminate layup ends here. Regarding the mounting plate, the stresses are reasonably low and well

within safe margins. The mast foam core is almost not experiencing stress. The core is surrounded by the carbon/epoxy laminate, which has much greater stiffness, and hence it is the laminate that transfers the load instead of the core material. The mast core is, however, under a fair bit of strain at the trailing edge.

When comparing the different material models, the stress distributions are almost identical along the fuselage. However, the magnitudes differ with the softer materials experiencing more stress. The most significant difference is seen in the stress concentration at the front of the fillet. When comparing the Mises stress criterion, the max stress experienced by the forged CFRP model is 7.8% higher than the aluminum/BMC model, and the max stress experienced by the polyamide/glass model is 35.9% higher than the aluminum/BMC model.

When comparing the maximum experienced stress from the simulations with the yield strength of the respective materials, it is observable that only the aluminum/BMC model experience less stress than the strength of the material. The safety factor for these materials is 1.39 for aluminum and 1.29 for BMC. Even though these are considered low safety factors, they can be justified under the presumptions that this is an extreme load case that is unlikely to be encountered in a natural environment. When analyzing the forged CFRP model, the max stress is 12.8% higher than the allowable limit set by the characteristic strength of the material in Chapter 4. The safety factor is hence less than 1, and the chance of failure is deemed likely. When analyzing the polyamide/glass fibre model, the max stress is more than twice the allowable limit given by the yield strength of the material. The safety factor is hence well below 1, and the chance of failure is deemed very likely. Due to the high stress concentration and since the strength of forged CFRP is nearly within an acceptable safety factor, there will be an attempt to reiterate the geometric design of the fuselage flange to gain confidence that forged CFRP can be a viable material choice for this part.

5.4.2 Deformation Results

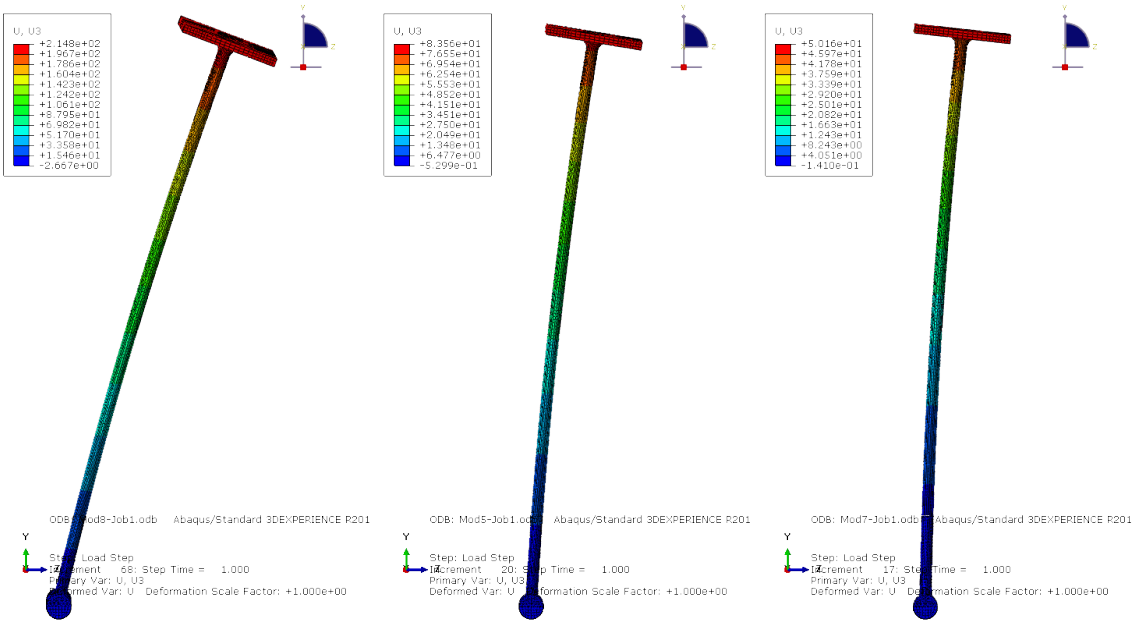

Figure 5.14: Deformation results in the U3-direction. From left to right glass/nylon; forged CFRP; aluminium/BMC.

Regarding the deformation of the hydrofoil, it is of most interest to analyze it in terms of individual deformations in the respective global coordinate directions. From figure 5.14 it is quite evident that the stiffness of the mounting plate and fuselage material largely influences the U3 deformation of the structure. The deformation in this direction mainly results from the load bending the mast and twisting the fuselage. Since all the models the has same core material properties and composite layup properties, it is clear that torsion in the fuselage can lead to large deforma-

tions with more flexible materials. Unsurprisingly, the polyamide/glass fiber model has the most considerable deflection as the elastic modulus is the lowest, followed by the forged CFRP, then the aluminum/BMC model. Regarding the deformation in the U3-direction, the polyamide/glass fiber model shows deformation of 215mm. This is equivalent to 30% of the mast length, which would make for an overly flexible and unresponsive design. The two other models, however, show acceptable results. The forged CFRP model has a deformation in the U3-direction of 83mm, while the aluminum/BMC model has a deformation of 50mm. When normalized over the mast length of 700mm, this equates to a deflection of 12% and 7%, respectively. Hence the aluminum/BMC model is about 66% stiffer than the forged CFRP model and about 330% stiffer than the polyamide/glass fiber model in this direction. The forged CFRP model has, however, adequate stiffness in itself.

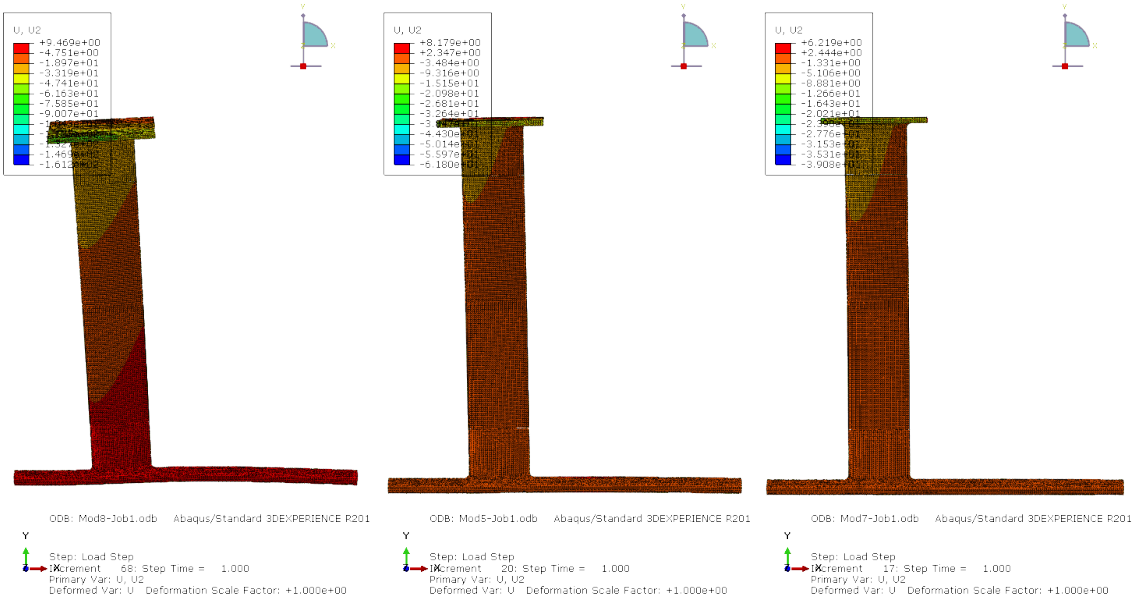

Figure 5.15: Deformation results in the U2-direction. From left to right glass/nylon; forged CFRP; aluminium/BMC.

Regarding the deformation in the U2 direction, the primary concern is determining how the fuselage will deflect in the xy-plane. The fuselage must be stiff in the U2 direction, as any deformation in this plane will alter the angle of attack of the front and rear wings. This will result in more unpredictable behavior and control issues of the hydrofoil. The maximum deflection of the horizontal region of the fuselage is 9.5mm, 3mm, and 1mm, respectively, for the polyamide/glass fiber, forged CFRP, and aluminum/BMC models. This is way too much regarding the result for polyamide/glass fiber. Such a deflection would cause noticeable changes in AoA for the rider. However, the results for the forged CFRP and aluminum/BMC models are quite acceptable, especially regarding aluminum/BMC. This suggests that the cross-sectional area of the fuselage is more than sufficient for these models and that the geometry can be altered as needed to obtain a more lightweight and hydro-dynamically efficient design.

Regarding the deformation in the U1-direction, the primary concern is the mast deflection in the cord-wise direction. Due to the geometry of the mast, with a long cord compared to the foil thickness, this will give rise to shear deformation of the mast. This, in turn, will cause high shear strain at the trailing edge, which is the most fragile part of the hydrofoil. The maximum deformation in the U1 direction at the top of the mast is 32mm, 12mm, and 6mm, respectively, for the polyamide/glass fiber, forged CFRP, and aluminum/BMC models. The results are within acceptable limits except for the polyamide/glass fiber model.

5.4.3 Fiber Layup Results

Table 5.6: The maximum and minimum stress in the 11-direction for each ply in the fiber skin laminate.

Stress 11-direction						
Model	**Glass reinforced polyamide**		**Forged CFRP**		**Aluminium / BMC**	
Ply No.	Max	Min	Max	Min	Max	Min
1 : 45°	355	-513	159	-191	83	-92
2 : -45°	475	-325	165	-197	63	-96
3 : 0°	662	-748	294	-359	145	-197
4 : 45°	240	-160	78	-100	57	-68
5 : -45°	116	-170	52	-76	45	-85
6 : 0°	277	-295	171	-223	159	-209
7 : 45°	176	-229	95	-97	65	-77
8 : -45°	173	-151	71	-80	60	-87
9 : 0°	370	-324	201	-244	188	-230

Table 5.7: The maximum and minimum stress in the 22-direction for each ply in the fiber skin laminate.

Stress 22-direction						
Model	**Glass reinforced polyamide**		**Forged CFRP**		**Aluminium / BMC**	
Ply No.	Max	Min	Max	Min	Max	Min
1 : 45°	47	-39	17	-22	7	-10
2 : -45°	26	-38	12	-16	6	-7
3 : 0°	21	-12	6	-5	6	-4
4 : 45°	15	-22	7	-9	4	-7
5 : -45°	9	-9	5	-5	5	-6
6 : 0°	14	-17	7	-8	6	-5
7 : 45°	10	-11	5	-6	5	-7
8 : -45°	22	-27	12	-12	6	-7
9 : 0°	25	-26	12	-13	7	-6

Table 5.8: The maximum and minimum stress in the 12-direction for each ply in the fiber skin laminate.

Stress 12-direction						
Model	**Glass reinforced polyamide**		**Forged CFRP**		**Aluminium / BMC**	
Ply No.	Max	Min	Max	Min	Max	Min
1 : 45°	47	-45	22	-20	12	-9
2 : -45°	39	-41	18	-19	9	-12
3 : 0°	3	-14	2	-4	1	-3
4 : 45°	29	-29	13	-14	9	-13
5 : -45°	23	-23	14	-11	13	-10
6 : 0°	3	-7	1	-3	2	-3
7 : 45°	20	-20	11	-15	11	-14
8 : -45°	21	-21	15	-12	14	-11
9 : 0°	14	-8	4	-3	3	-4

The stresses in the mast laminate layup should be analyzed ply by ply. This is because the stress results make more sense when viewed from the principle directions of each respective ply rather than for the entire laminate in the global coordinate system. The layup was defined as nine plies, as it was hypothesized that such a layup definition should approximately be equivalent to a triaxial laminate consisting of 3 layers. It is quite evident that when the hydrofoil parts are made with stiffer materials, the forces transferred by the laminate become less, as the other parts are more able to resist deformation. As seen in table 5.6 5.7 and 5.8 the stresses are several times

larger for the polyamide/glass fibre model than for the aluminium/BMC model regarding all of the different orientations. Regarding the forged CFRP model, the stresses are generally about 1.5-2 times greater than in the aluminum/BMC model. The stress distributions throughout the plies are, however, largely comparable between the different models.

The stresses in the 11-direction are by far the largest. This is due to the 11-direction being the longitudinal fiber direction and hence able to transfer more of the load. Most of the load is being transferred in this longitudinal direction; hence, it should be expected and desired that the largest stresses be found here. Regarding the transverse 22-direction and the in-plane shear in the 12-direction, the stresses are several magnitudes lower than for the longitudinal 11-direction, as is desired. For forged CFRP and aluminum/BMC, the stresses are well within acceptable limits in all the orientations. However, the transverse and shear stress is on the larger side for some of the plies in the layup for the polyamide/ glass fiber model. The largest stresses were sometimes probed at the very edge of the laminate near constrained nodes. These large stress results are hence not representative of the general stress throughout some of the plies. This is likely due to some modeling constraints and not a concern for the integrity of the laminate. If a stiffer and stronger mast is desired, adding one more tri-axial layer to the layup is justifiable without incurring significantly more expenses, apart from slightly higher material cost.

5.4.4 Reiteration of the Design

From the stress results, it can be concluded that the design is suitable for aluminum and BMC as the mounting plate and fuselage material. Regarding polyamide/glass fiber, the large deflections indicate that the material is not suitable for the proposed structural design concept. In addition, failure is likely imminent due to the low safety factor. Forged CFRP, however, has adequate stiffness. The stress concentrations are on the higher side but close to being within an acceptable limit. There will therefore be an attempt to improve the design to facilitate the use of forged CFRP with the properties found in Chapter 4. The mounting plate had a stress distribution within acceptable limits, so no geometrical changes need to be made to this part. However, the geometry of the fuselage needs to be reiterated to achieve an acceptable safety factor.

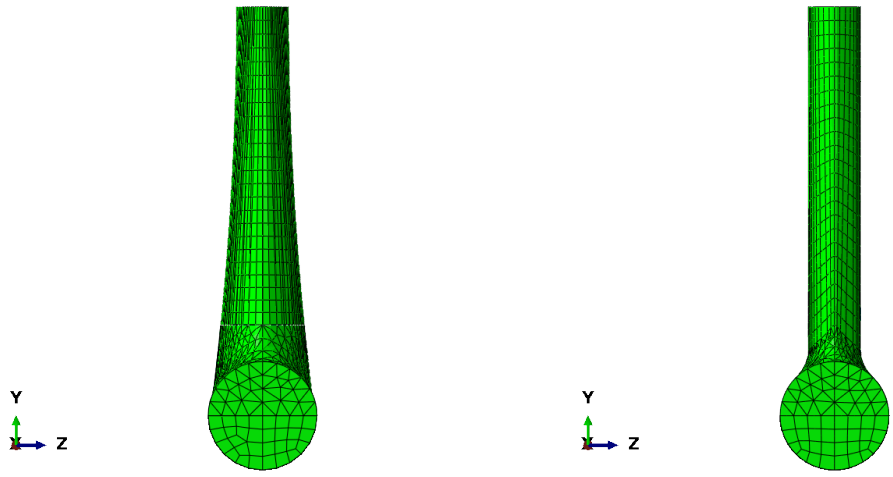

Figure 5.16: Front view of the second fuselage design (to the left) compared with first fuselage design (to the right).

The transition in the cross-section between the horizontal section of the fuselage and the flange can, in a sense, be regarded as a notch. Hence one way to reduce the stress concentrations is by increasing the radius in the transition between the cross-sections. The goal of the new design was to maintain the NACA0012 profile along the flange while simultaneously striving to minimize the notch effect. Again SolidWorks was used to design the new iteration based on the previous design.

The new geometry was achieved through surface modeling. By creating lofted surfaces between two

scaled NACA0012 profile sketches and using guide curves, it was possible to achieve a smoother transition between the fuselage and flange compared to the previous more abrupt geometry change. A NACA0012 sketch was created at the mid-plane of the circular fuselage. This sketch was scaled so that the maximum width of the profile sketch equaled the diameter of the circular fuselage cross-section to maximize cross-sectional utilization. The sketch was scaled about the chord x-coordinate of maximum thickness so that this coordinate correlates between the two lofted sketches.

Guide curves were implemented in the xy-plane and yz-plane to add curvature to the loft. The curves are of constant curvature and run between the respective leading and trailing edges on the xy-plane and between the points of max thickness on the yz-plane. The guide curves are tangent with the vertical axis at the upper sketch of the loft for seamless integration with the mast parts. There was implemented an R12 fillet along the entire flange profile and an R30 fillet at the trailing edge for an even smoother transition.

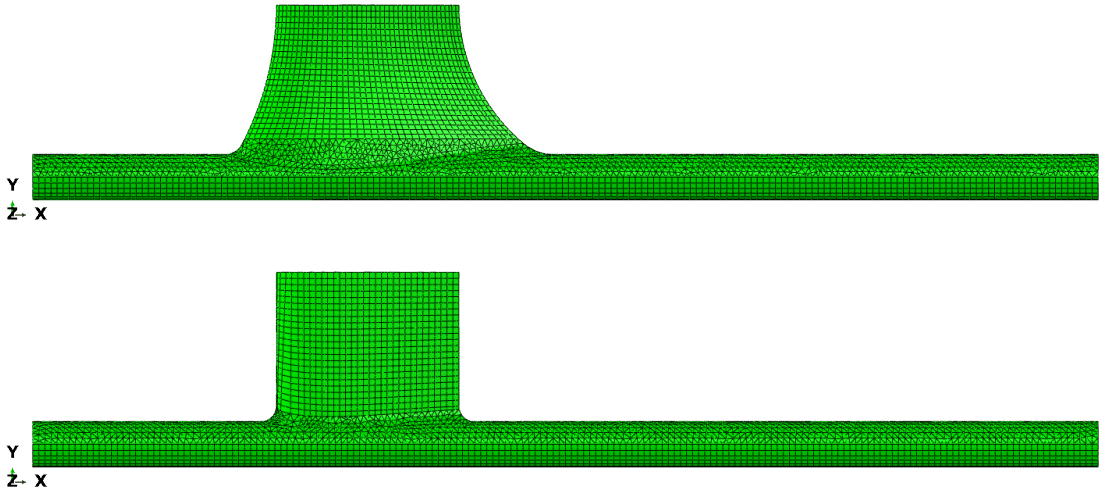

Figure 5.17: Side view of the second fuselage design (at the top) compared with first fuselage design (at the bottom).

The new fuselage geometry was imported into Abaqus/CAE for analysis. The mounting plate and mast core parts were unmodified from the previous simulation, while the geometry of fiber skin was edited to fit with the new flange design. In this analysis, only the response of the forged CFRP material is of interest; hence, only these properties are used for the mounting plate and fuselage. However, the new design would also enhance the performance of aluminum and BMC. The load, boundary conditions, and interactions remain the same as in the previous simulation. So does the mesh, except that the partitions are slightly different to facilitate the new flange design.

The stress results clearly show that the new design geometry successfully decreased the stresses in the areas of interest. In the transition at the leading edge, the stress distribution is more even with the surrounding areas, and the stress concentration value is drastically reduced. When probing the field output using the elemental nodal positioning method, the highest recorded stress in this area was 144MPa. This is about a 30% reduction in stress compared with the respective value of 207MPa for the first design iteration. Using this probed value and the same failure stress criterion as previously, then the factor of safety comes out to be 1.33. This FOS is comparable to the ones obtained for aluminum and BMC in the previous design.

It is also visible that the band of stress running along the chord length of the flange has almost disappeared compared with the first design iteration. The maximum stress is still found at the trailing edge, where the carbon fiber skin ends. However, when probing, the stress peak is localized to only a single node in tie constraint between hexahedral and tetrahedral elements, while the surrounding nodes show lower stress. Due to the tie constraint and generally poor element geometry in this area, the exact stress values here are of little analytical value.

In conclusion, the new design allows the use of forged CFRP as the fuselage material. As a constraint for the new flange design was the premise that the flange was to have a constant

NACA0012 profile. If the loft could have a more variable cross-section, it should be possible to create a better design that further eliminates the notch effects. A downside to having a more gradual transition, such as in the new design iteration, is that cutting and applying the fiber skin layup will be slightly more complicated. The new flange design geometry could also be implemented to the mounting plate to achieve better stress distributions in this part as well. However, the already established mounting plate design is deemed to be adequate.

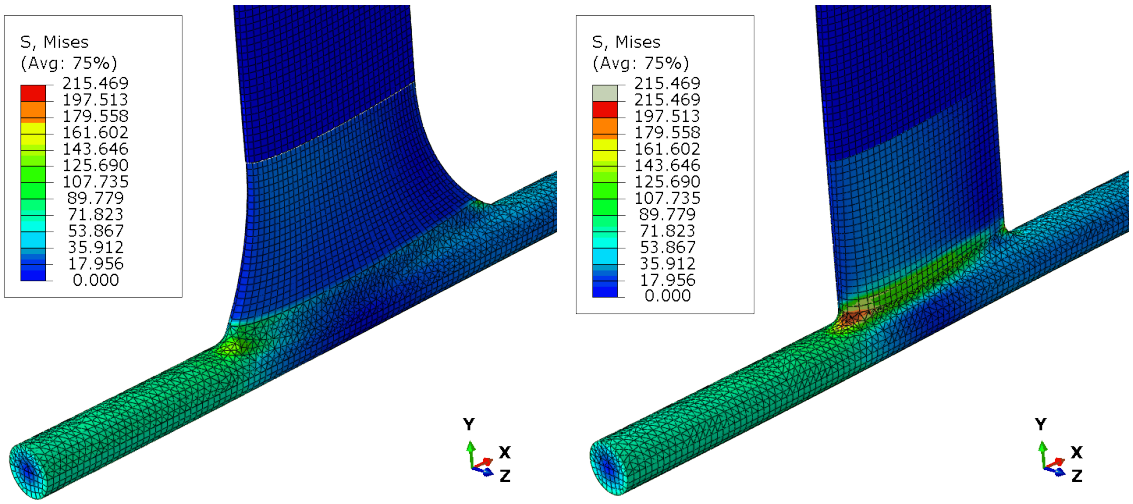

Figure 5.18: Comparison between the second (left) and the first (right) design iteration regarding the stress distribution and the stress concentration located at the front of the fuselage flange.

5.5 Prototype Development

Based on the new iteration of developed part designs, it is desired to create prototype parts to explore if the carbon fiber forging process is suitable for such parts in practice. As discussed earlier, the mounting plate and fuselage are of interest to manufactured from forged CFRP, and molds for forging these two parts were therefore designed.

Due to restricted access to machinery and manufacturing equipment, it was decided to manufacture the mold tools with additive manufacturing in the same manner as the mold tools for the material test specimens. The FFF printer accessible was a Prusa MK3S, so the tool designs were adapted to be manufactured with this machine. The mold tool parts were designed for full-scale prototypes. However, due to time constraints and the printer's build volume restrictions, it was decided to manufacture the molds at 60% scale for more rapid results. At 60% scale, it was possible to manufacture all the mount mold components as single pieces, while the long fuselage mold components needed to be manufactured in two pieces. The fuselage mold pieces were then joined through adhesive bonding with epoxy resin. The printer settings were set to 0.15mm layer height and an infill density of 15% with a gyroid pattern. These are identical settings to the material test molds in Chapter 4.

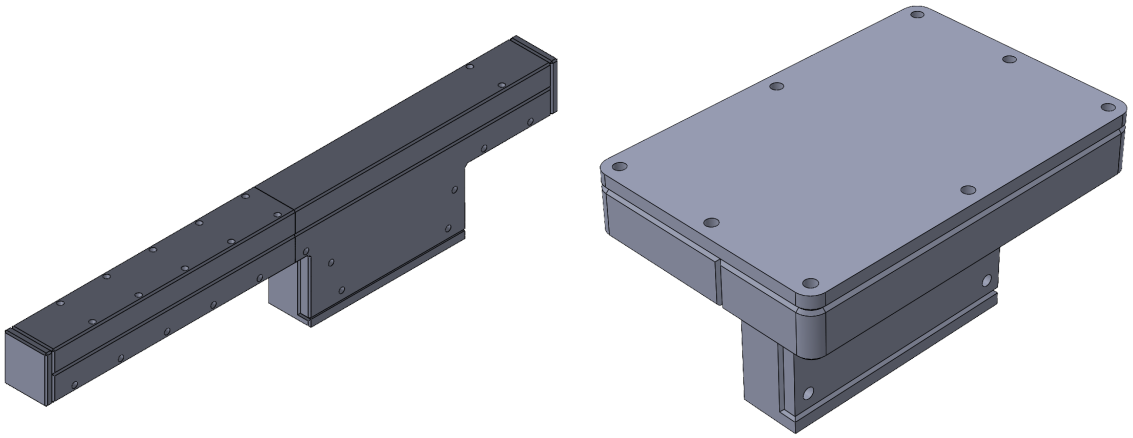

(a) SolidWorks model of the fuselage mold design.

(b) SolidWorks model of the mounting plate mold design.

Figure 5.19: The prototype mold assemblies.

Both molds were designed as 3-piece configurations after experiencing some difficulty with removing the forged CFRP plates from the 2-piece test mold designs. Due to the shape of the parts, this configuration has the added benefit of making the molds easier to load with the material. Another key feature of the mold designs is the piston-like geometry at the core sides of the molds. Through experimentation in Chapter 4, it was experienced that a considerable piston effect was necessary to keep the material from escaping the mold when pressure is applied. A draft angle of 15° was implemented between all the mold pieces. This was done to ensure that the pieces would easily come apart when extracting the forged CFRP parts. A symmetric chamfer of 2mm was also implemented on all edges between the mold pieces to aid extraction. Since the molds were to be manufactured at 60% scale, the bolt bores were designed to be oversized to facilitate the use of the intended full-scale bolt diameter.

The modeling aspect of designing the molds was done with the following techniques. The molds were created in an assembly as solids surrounding the part geometry of the mounting plate and fuselage, respectively. The geometric volume of the mounting plate and fuselage was then subtracted from these solids. This left the solids with mold cavities of the exact part geometry that is desired for the forged parts. Then parting surfaces were created to split the solids into separate individual mold pieces. All the pieces fit together perfectly using this technique. Lastly, features such as chamfers and bolt bores were added to the designs.

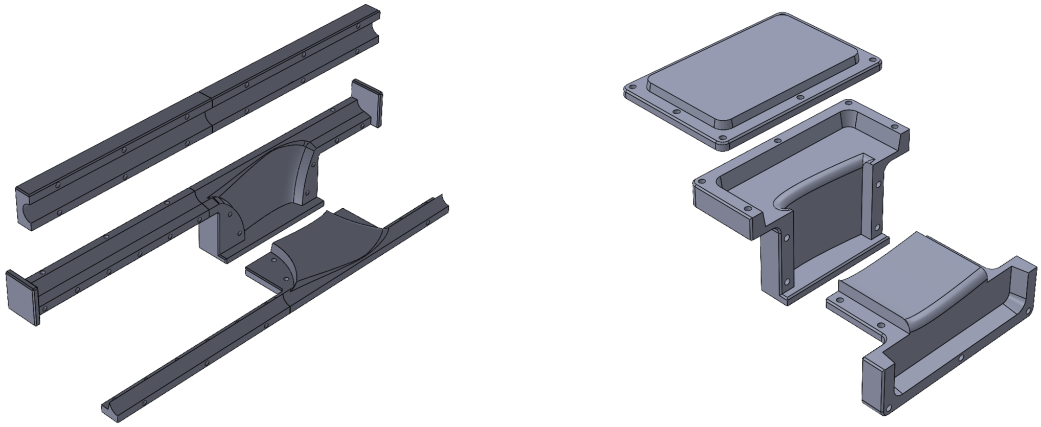

(a) SolidWorks model of the fuselage mold design.

(b) SolidWorks model of the mounting plate mold design.

Figure 5.20: Exploded views of the prototype mold assemblies.

After printing, the molds were sanded to reduce the layer lines in the print. The layup process was then executed similarly to when making the test specimens in the second batch. Due to the complex geometry, it was decided to premix the chopped fiber and epoxy resin. Since there is a large volume of dry fiber, it is easier to wet it out and reduce the bulk volume as much as possible before loading the molds. Hence, the fiber mass was measured and thoroughly mixed into the resin. The mixture was then compressed by hand in the mixing cup and put into a vacuum chamber for degassing. After degassing, the material was compressed even further. This resulted in a wet material with a considerable resemblance to a bulk molding compound. Due to the compact volume, the material was easy to load into the molds despite the relatively complex shape. The molds were bolted shut, and clamps were applied. The parts were left to cure for 30 hours. After the initial cure, the molds were opened, and the parts were post-cured at 80°for 24 hours. The 3-piece mold designs proved successful in making it easy to extract the parts. The molds were not damaged when opened but should be regarded for single-time use due to the printed construction.

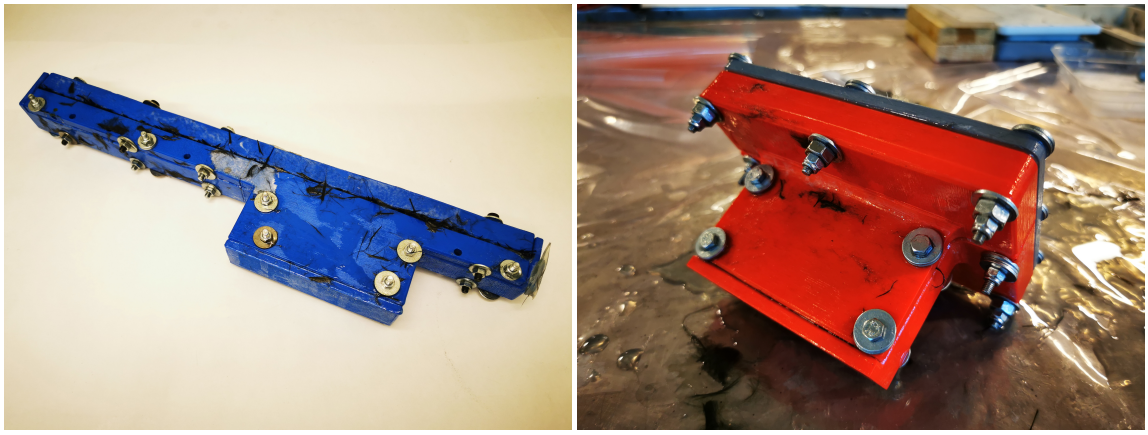

(a) The fuselage mold loaded and bolted together.

(b) The mount mold loaded and bolted together.

Figure 5.21: Pictures of the prototype molds.

The prototyping process proved to be quite successful. The overall shape of the finished parts correlated well with the desired geometry in CAD. All the features were captured and transferred to the parts even at 60% scale. One of the most desired qualities of forged CFRP is the low density and hence the potential for making strong yet lightweight parts. The masses of the 60% scaled mounting plate and fuselage prototypes were measured to be 117.4g and 219.1g, respectively. At full scale, this would equate to 543.5g and 1014.3g, respectively. In SolidWorks, it was estimated that the same parts made from aluminum 6061 would have masses of 995.4g regarding the mounting plate and 1851.3g regarding the fuselage. Hence the equivalent parts made from aluminum would be about 83% heavier than the same parts made from forged CFRP. In other words, the forged CFRP parts are almost half the weight of equivalent aluminum parts.

(a) The finished forging of the mounting plate.

(b) A defect at the flange transition.

(c) The finished forging of the fuselage showing the flange transition at the front.

(d) Full view of the finished forged fuselage.

Figure 5.22: The final prototypes of the forged CFRP parts.

Table 5.9: The mass and material of the different parts in the proposed design.

Part	**Mass**	**Material**
Mounting Plate	543.5g	Forged CFRP
Fuselage	1014.3g	Forged CFRP
Mast Core	44.4g	PVC Foam
Mast Fibre	732.1g	3 Layers Triaxial CFRP
Front Wing Core	96.9g	PVC Foam
Front Wing Fibre	629.3g	2 Layers Triaxial CFRP
Rear Wing	207.1g	Forged CFRP
Total	**3267.6g**	

The mass of the individual parts with the respective materials and the total mass of the entire hydrofoil assembly was estimated and summarized in table 5.9. The total mass of the hydrofoil assembly was calculated to be 3267.6 grams when assuming a carbon fiber/epoxy density of $\rho = 1.6g/cm^3$ for the fabric laminates. For comparison, the industry-leading Duotone Daytona D-LAB hydrofoil has a reported total mass of 2950 grams. The Dayton was designed with the purpose of competing in the coming Olympic Games and is a highly optimized racing hydrofoil. It is made with high modulus pre-preg carbon fiber, capable of reaching 40 knots, and comes with a price tag of €2899. Hence this project can be regarded as quite successful in having developed a design that achieves such a low weight for a design intended to be inexpensive and catered towards novice riders.

The prototyped parts are not entirely without flaws. Most obviously are the imprinted parting lines from where the mold pieces come together. This is primarily a cosmetic flaw and has little influence on the structural integrity of the parts. More concerning are the pinholes, which can be found at various locations of the parts. The pinholes likely stem from tiny air bubbles being trapped during the forging process. These pinholes may indicate that air bubbles are also trapped inside the structure, which increases porosity and directly affects the strength of the parts. The surface finish could be improved and pinholes reduced by sanding the surface and applying a clear coat. This will, however, incur more manual labor in the manufacturing process.

The most concerning flaws for structural integrity are spots that lack a sufficient amount of resin. Such a spot was found at the rear of the flange transition of the mounting plate, as shown in figure 5.22a. These defects seem to be occurring at abrupt angles as they can also be found at the exterior right angles of the parts. It seems wise to avoid sharp angles and incorporate gradual transitions into the part designs to minimize these defects. Molds with a smoother surface and higher consolidation pressure could also be a solution, as this would force more fiber and resin to fill these pockets.

Overall the finished prototypes were rather satisfactory, given the rudimentary manufacturing equipment. However, the process of forging CFRP parts with these 3D printed molding tools does not reach the quality of commercial standards. The process is, on the other hand, quick and effective for the purpose of prototyping parts. Hence the technique could provide value in the concept development stages of product development. The process of compression forging parts in 3D printed molds makes it fast and easy to test different design iterations and bring them to reality without it incurring significant expenses to the project. With the given method, parts with close to exact CAD geometry and physical feel can be created without the need for expensive mold tools. This opens the opportunity for a new form of rapid prototyping. With professional mold tools, the concept has the possibility of creating parts of commercial quality and improved mechanical properties.

Chapter 6

Conclusion

6.1 Conclusion of the Hydrofoil Development

The main objective of this thesis was to develop a new and functional hydrofoil design concept that is possible to bring to market with low initial investment and low manufacturing cost per unit.

In Chapter 2, the effect and relevance of different hydrodynamic design parameters were investigated and analyzed. The effects of changing these design parameters were explored with simulations in Xflr5, and the results were compiled into an easy-to-navigate table. The purpose of the table was to explain which parameters to change when tuning a hydrofoil design for a specific riding style. By consulting this table, parameters were decided for a hydrodynamic design in compliance with the needs of a novice rider. The developed table can be a great, time-saving tool for future designs as it systematizes the iterative tuning process. The investigation was limited to only select foil profiles chosen on presumed knowledge. These foil profiles are not necessarily the optimal solution, and future work should strive to develop a system for choosing the optimal foil profiles based on the desired riding style. The investigation was also limited to flat wings due to the ease of manufacturing such wings. Future work should ideally also develop a system to identify the amount of dihedral and anhedral for the desired stability response.

In Chapter 3, different materials and manufacturing methods were discussed. A new, never seen concept was proposed that combines forged CFRP parts with a traditional foam core and carbon/epoxy skin laminate to produce a single structural part with no fasteners. It was decided that a 4-axis hot wire CNC machine was the most favorable and affordable option for manufacturing the foam cores of the mast and front wing. Forged CFRP was chosen as the other material due to the low material cost and since parts can be manufactured from it with minimal equipment and no need for skilled labor.

Due to little information about forged CFRP in the literature, it was decided to investigate the mechanical properties of forged CFRP through 4-point flexural along with mold design testing in Chapter 4. The elastic modulus was found to be 25670.92MPa and the characteristic strength to be 191.27MPa. However, there were significant inconsistencies in the results among samples and between the batches. Future work should determine the effect of parameters such as fiber length, fiber volume fraction, and consolidation pressure on the resulting mechanical properties through a more systematic approach. It was hypothesized that with more sophisticated manufacturing equipment, it should be possible to achieve better mechanical performance with forged CFRP.

In Chapter 5, FEA was conducted to verify that the structural design concept would be viable in the real world. Three different materials were compared for the mounting plate and fuselage, with the main focus being on forged CFRP. The concept proved successful for aluminum 6061 and BMC, while polyamide/glass fiber was discarded due to insufficient strength and stiffness. Forged CFRP proved to have sufficient stiffness, while the strength was a little too low for it to be a viable material choice. Another design iteration was created with geometric changes made to the fuselage flange. With the new iteration, a safety factor of 1.33 was achieved. This is comparable to the safety factors achieved with aluminum 6061 and BMC, and the new design was deemed successful. Further improvements can still be made to achieve lower stress at the concentrations. The analysis would also benefit from mesh refinement at the trailing edge, where the elements are of poorer quality. It would also be interesting to analyze how the parts are damaged by fatigue.

Based on the knowledge gained about forging and mold design in Chapter 4, molds were developed for prototyping the mounting plate and the fuselage. The prototypes incorporated the final verified design analyzed in Chapter 5. The molds were 3D printed in PLA at 60% scale with standard settings on a Prusa MK3s. The forging process was successful, and the final prototyped parts were deemed entirely satisfactory. The weights of the final parts were almost half the weight of equivalent aluminum parts. Although the prototypes had a couple of flaws and did not live up to commercial standards, this manufacturing process provides a fast and simple way of prototyping forged parts. Further work should explore the potential of forging parts in permanent mold tools of industry standards. It would be interesting to explore if it is possible to create parts of commercial grade and see if forged CFRP can compete with the mechanical performance of BMC. It is also of interest to physically test the parts and compare the findings with the FEA results.

Overall this thesis has laid the groundwork for a product that incorporates the proposed design and material concept. The findings have shown enough potential that the author desires to use them in further development and explore the commercial possibility.

References

[1] J. Holt, C. Ho and H. Mindlin, *Structural Alloys Handbook: 1996 Edition; Incorporating Supplements Throught 1995*. Cindas/Purdue Univ., 1997. [Online]. Available: https://books.google.no/books?id=dB9TmwEACAAJ.

[2] W. H. Mason, *Applied Computational Aerodynamics*. Cambridge University Press, 1997, ISBN: 9781107053748.

[3] R. M. Jones, *Mechanics of Composite Materials*. Taylor Francis, 1999, ISBN: 1-56032-712-X.

[4] 'Aerodynamic lift and drag and the theory of flight', Electropedia. (2005), [Online]. Available: https://www.mpoweruk.com/flight_theory.htm (visited on 15th Dec. 2021).

[5] A. C. Kermode, R. H. Bernard and D. R. Philpott, *Mechanics of Flight*. Pearson, 2006, ISBN: 978–1–4058–2359–3.

[6] F. Mujika, 'On the difference between flexural moduli obtained by three-point and four-point bending tests', *Polymer testing*, vol. 25, no. 2, pp. 214–220, 2006.

[7] M. L. Huber, R. A. Perkins, A. Laesecke *et al.*, 'New international formulation for the viscosity of h 2 o', *Journal of Physical and Chemical Reference Data*, vol. 38, no. 2, pp. 101–125, 2009.

[8] PerformanceComposites. 'Mechanical properties of carbon fibre composite materials, fibre / epoxy resin (120°c cure)', PerformanceComposites. (2009), [Online]. Available: http://www.performance-composites.com/carbonfibre/mechanicalproperties_2.asp (visited on 12th Mar. 2022).

[9] M. Smith, *ABAQUS/Standard User's Manual, Version 6.9*, English. United States: Dassault Systèmes Simulia Corp, 2009.

[10] C. Kassapoglou, *Design and Analysis of Composite Structures: With Applications to Aerospace Structures*. John Wiley Sons, Ltd, 2010, ISBN: 9780470972717.

[11] D. D. Howell and S. Fukumoto, 'Compression molding of long chopped fiber thermoplastic composites', in *Proceedings of the CAMX Conference Proceedings, Orlando, FL, USA*, 2014, pp. 13–16.

[12] K. Bell, *Konstruksjonsmekanikk Del II: Fasthetslære*. Fagbokforlaget Vigmostad Bjørk AS, 2015.

[13] F. E. Hitchens, *The Encyclopedia of Aerodynamics*. AUK Academic, 2015, ISBN: B0186256XY.

[14] S. Ekşı and K. Genel, 'Comparison of mechanical properties of unidirectional and woven carbon, glass and aramid fiber reinforced epoxy composites', *composites*, vol. 132, pp. 879–882, 2017.

[15] TUDelft, *Longitudinal static stability*, TU Delft, 2017. [Online]. Available: https://ocw.tudelft.nl/wp-content/uploads/Hand-out-Stability_01.pdf (visited on 15th Dec. 2021).

[16] *Closed cell pvc core foam*, Easy Composites, 2018. [Online]. Available: https://media.easycomposites.co.uk/datasheets/EC-TDS-EASYCell-40-75.pdf.

[17] K. Perry, *Interpreting fea results: Integration point data*, 2018. [Online]. Available: http://drperry.org/2009/interpreting-fea-results-integration-point-data/.

[18] *Tecamid 66/x gf50 black*, AD, Ensinger, 2018. [Online]. Available: https://www.ensinger-online.com/modules/public/sheet/createsheet.php?SID=1381&FL=0&FILENAME=TECAMID_66-X_GF50_black_0.PDF&ZOOM=1.2.

[19] P. B. Serra, 'Hydrofoil design and construction', M.S. thesis, BarcelonaTech, 2019.

[20] *Toray ms-1h*, Toray, 2019. [Online]. Available: https://www.toraytac.com/media/b9c7a4a2-0340-487e-8186-1c5722629602/yjaVDw/TAC/Documents/Data_sheets/Bulk%5C%20molding%5C%20compounds/Bulk%5C%20molding%5C%20compounds/MS-1H_Epoxy_PDS.pdf.

[21] T. A. Laux, 'Experimental and computational characterisation of composite laminates subjected to multiaxial loading', Ph.D. dissertation, University of Southampton, 2020.

[22] 'Mast technology', RRD. (2020), [Online]. Available: https://equipment.robertoriccidesigns.com/multiple-sport-hydrofoil-masts/ (visited on 15th Dec. 2021).

[23] *How to compression mould forged carbon fibre components*, Easy Composites, 2021. [Online]. Available: https://www.easycomposites.co.uk/learning/compression-moulding-forged-carbon-fibre (visited on 15th Mar. 2022).

[24] Simscale. 'What is fea — finite element analysis?', Simscale. (2021), [Online]. Available: https://www.simscale.com/docs/simwiki/fea-finite-element-analysis/what-is-fea-finite-element-analysis/ (visited on 21st May 2022).

[25] N. P. Vedvik. 'Flexural testing', NTNU. (2021), [Online]. Available: https://folk.ntnu.no/nilspv/TMM4175/flexural-testing.html (visited on 12th Feb. 2022).

[26] ——, 'Material variability and characteristic strength', NTNU. (2021), [Online]. Available: https://folk.ntnu.no/nilspv/TMM4175/material-variability-and-characteristic-strength.html (visited on 12th Feb. 2022).

[27] Ensinger. 'Glass filled polyamides', Enisnger. (), [Online]. Available: https://www.ensingerplastics.com/en/shapes/modified-plastics/glass-filled-polyamides (visited on 7th Jun. 2022).

[28] Instron. 'What is bend testing?', Instron. (), [Online]. Available: https://www.instron.com/en/our-company/library/test-types/flexure-test (visited on 4th Feb. 2022).

[29] Kevra. 'Vacuum injection', Kevra. (), [Online]. Available: https://kevra.fi/guides/vacuum-infusion/?lang=en (visited on 7th Jun. 2022).

[30] Siemens. 'Computer-aided engineering (cae)', Siemens. (), [Online]. Available: https://www.plm.automation.siemens.com/global/en/our-story/glossary/computer-aided-engineering-cae/13112 (visited on 22nd May 2022).

[31] '6061 aluminum vs 6063 in extrusion applications', Clinton Aluminium. (Sep. 2017), [Online]. Available: https://www.clintonaluminum.com/6061-aluminum-vs-6063-in-extrusion-applications/ (visited on 19th Dec. 2021).

[32] L. N. Bonikowsky, 'Hydrofoil', in The Canadian Encyclopedia, Mar. 2015. [Online]. Available: https://www.thecanadianencyclopedia.ca/en/article/hydrofoil (visited on 16th Dec. 2021).

[33] C. Cutler. 'How does aspect ratio affect your wing?', Boldmethod. (Dec. 2015), [Online]. Available: https://www.boldmethod.com/learn-to-fly/aircraft-systems/how-does-aspect-ratio-affect-a-wing/ (visited on 15th Dec. 2021).

[34] D. Daniel. 'Airfoil selection', Ultralight Design. (Oct. 2017), [Online]. Available: https://ultralightdesign.wordpress.com/2017/10/22/aerofoil-selection/ (visited on 15th Dec. 2021).

[35] 'Fibre-reinforced plastic composites — determination of flexural properties', International Organization for Standardization, Geneva, Switzerland, Standard, Mar. 1998.

[36] P. Latteier. 'Carbon fiber weaves: What they are and why to use them', Elevated Materials. (Jan. 2019), [Online]. Available: https://www.elevatedmaterials.com/carbon-fiber-weaves-what-they-are-and-why-to-use-them/ (visited on 19th Dec. 2021).

[37] MiT, *Lab 8 notes – basic aircraft design rules*, Massachusetts Institute of Technology, Apr. 2006. [Online]. Available: https://ocw.mit.edu/courses/aeronautics-and-astronautics/16-01-unified-engineering-i-ii-iii-iv-fall-2005-spring-2006/systems-labs-06/spl8.pdf (visited on 15th Dec. 2021).

[38] Shalmali. 'Drag force - aerodynamics force resolution', Mech Flow. (Jul. 2021), [Online]. Available: https://www.mechnflow.com/post/drag-force-aerodynamics-force-resolution (visited on 15th Dec. 2021).

[39] *Xflr5 analysis of foils and wings operating at low reynolds numbers*, Xflr5, Oct. 2009. [Online]. Available: https://engineering.purdue.edu/~aerodyn/AAE333/FALL10/HOMEWORKS/HW13/XFLR5_v6.01_Beta_Win32%5C%282%5C%29/Release/Guidelines.pdf (visited on 16th Dec. 2021).

Appendix

A Equations for Constructing NACA 4-digit Foil Profiles

The NACA 4-digit foil profiles are constructed by combining a thickness envelope with a camber or mean line. The equations which describe this procedure are [2];

$$x_u = x - y_t(x)sin\theta \tag{1}$$

$$y_u = y_c(x) + y_t(x)cos\theta \tag{2}$$

and

$$x_l = x + y_t(x)sin\theta \tag{3}$$

$$y_l = y_c(x) - y_t(x)cos\theta \tag{4}$$

where $y_t(x)$ is the thickness function, $y_c(x)$ is the camber line function, and

$$\theta = arctan(\frac{dy_c}{dx}) \tag{5}$$

is the camber line slope. The NACA 4-digit thickness distribution is given by:

$$\frac{y_t}{c} = (\frac{t}{c})[a_0\sqrt{\frac{x}{c}} - a_1(\frac{x}{c}) - a_2(\frac{x}{c})^2 + a_3(\frac{x}{c})^3 - a_4(\frac{x}{c})^4] \tag{6}$$

a_0	a_1	a_2	a_3	a_4
1.4845	0.6300	1.7580	1.4215	0.5075

The camber line is given by:

$$y_c = \frac{M}{P^2}[2P(x/c) - (x/c)^2] \tag{7}$$

$$\frac{dy_c}{dx} = \frac{2M}{P^2}[P - (x/c)] \tag{8}$$

for $(x/c) < P$, and

$$y_c = \frac{M}{(1-P)^2}[1 - 2P + 2P(x/c) - (x/c)^2] \tag{9}$$

$$\frac{dy}{dx} = \frac{2M}{(1-P)^2}[P - (x/c)] \tag{10}$$

for $(x/c) > P$ [2]

B $C_m - \alpha$ plots

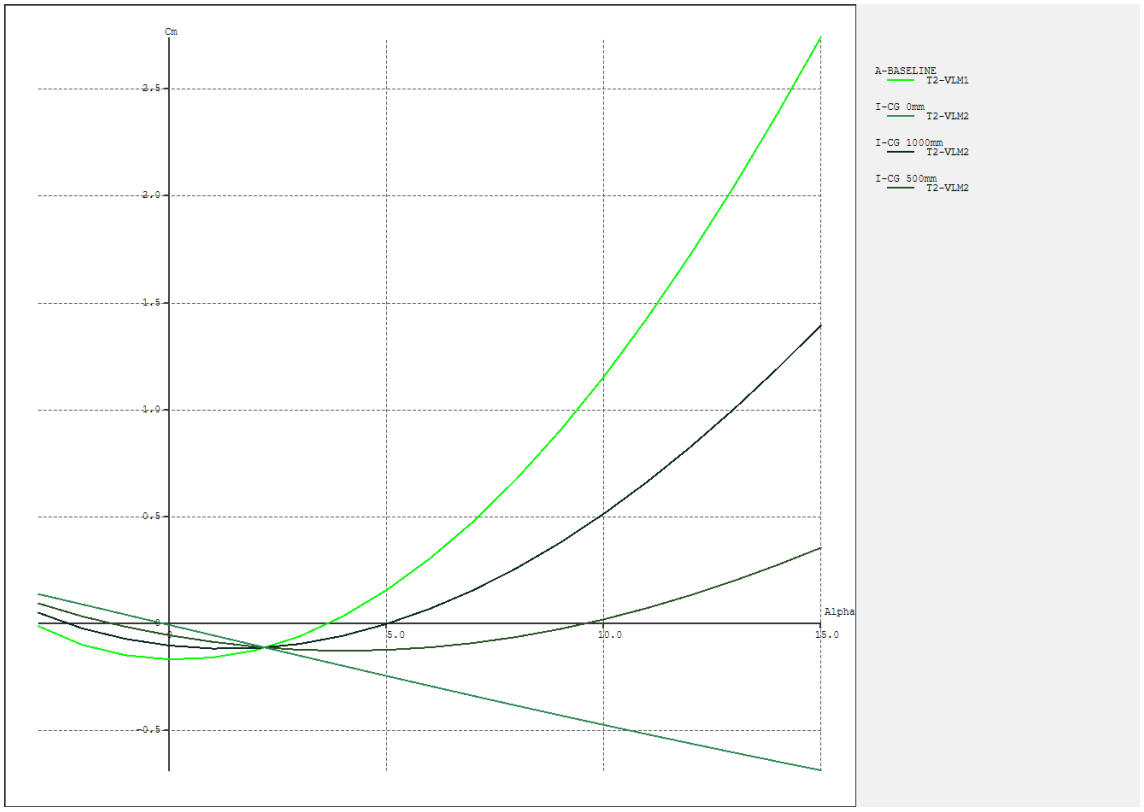

Figure 1: Vertical centre of gravity effect.

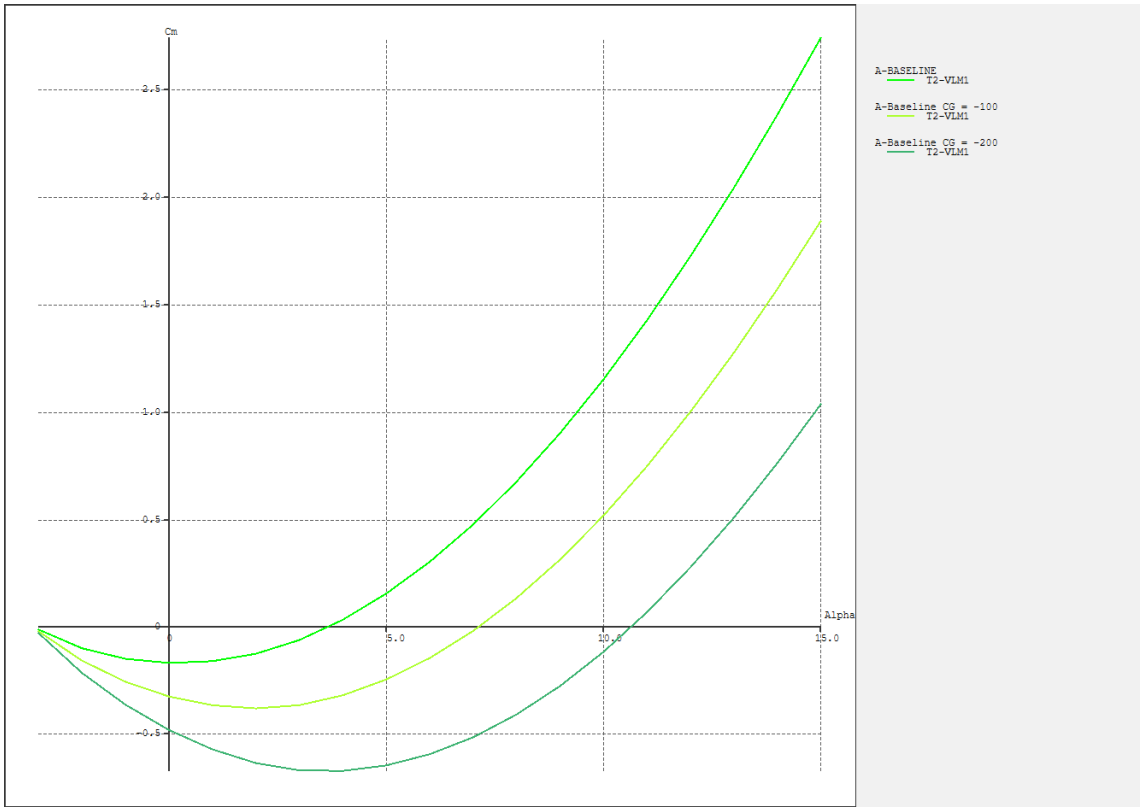

Figure 2: Longitudinal centre of gravity effect.

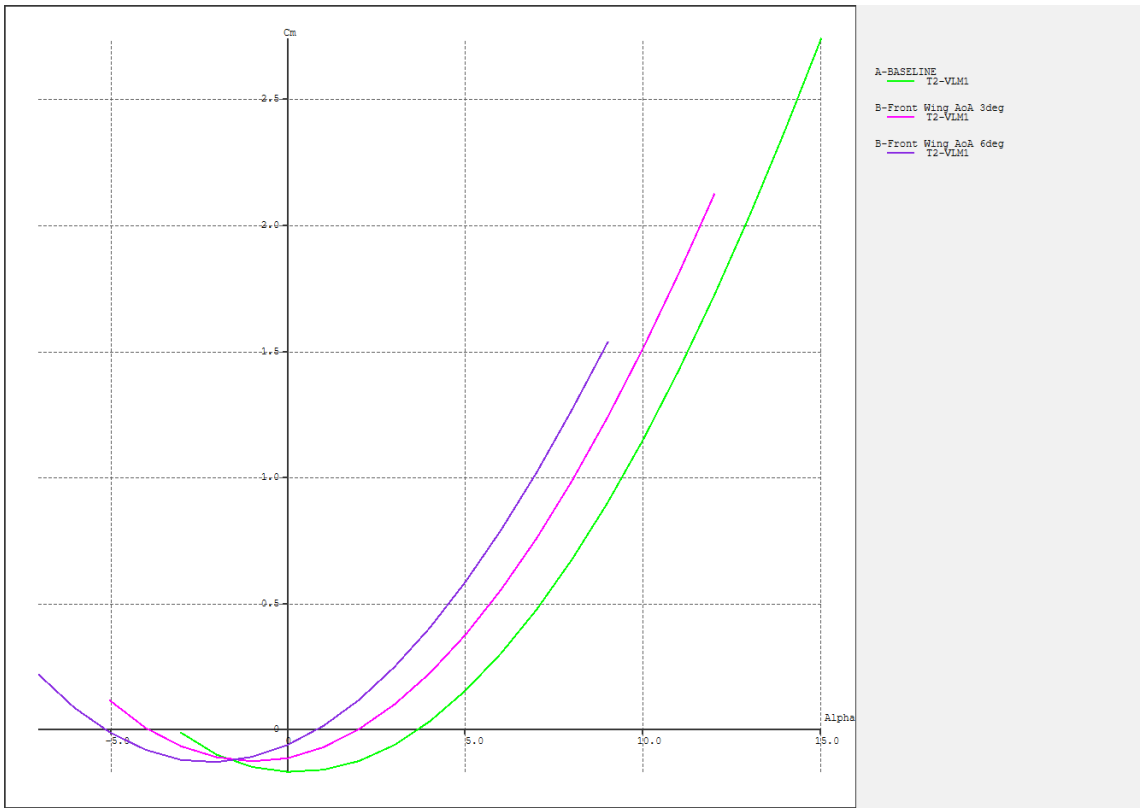

Figure 3: Front wing angle of incidence effect.

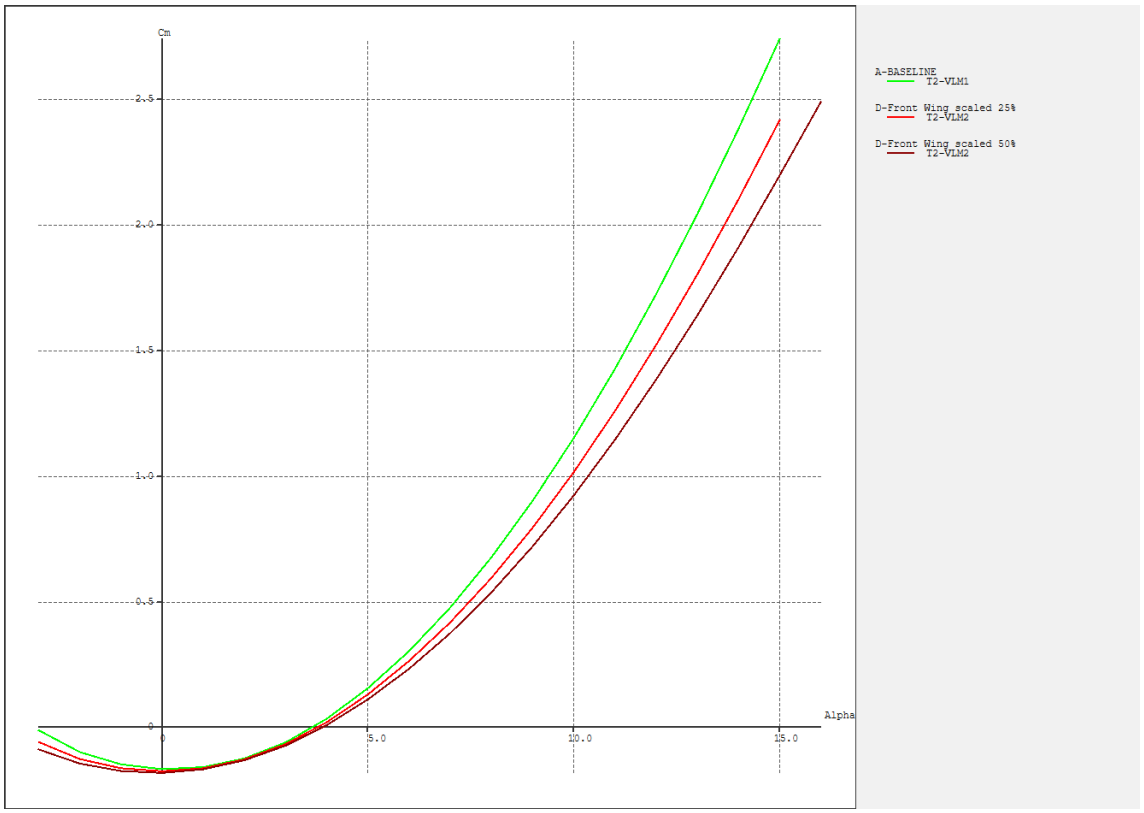

Figure 4: Front wing area effect.

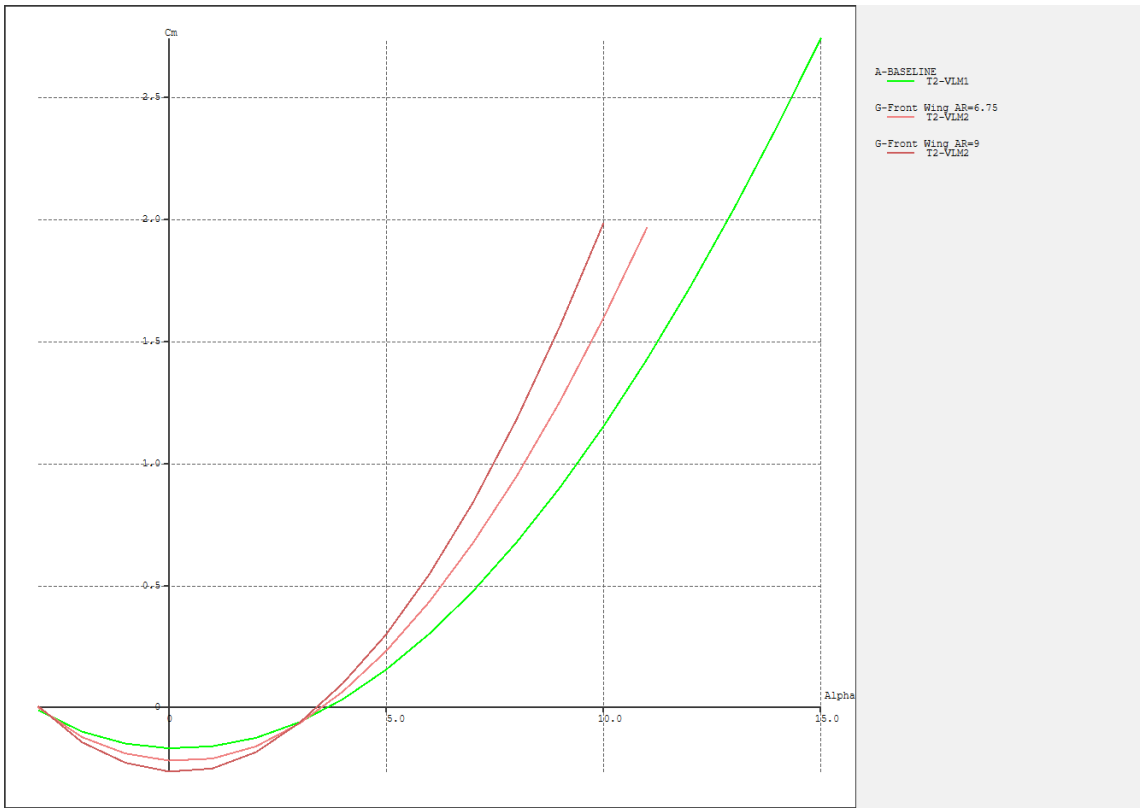

Figure 5: Front wing aspect ratio effect.

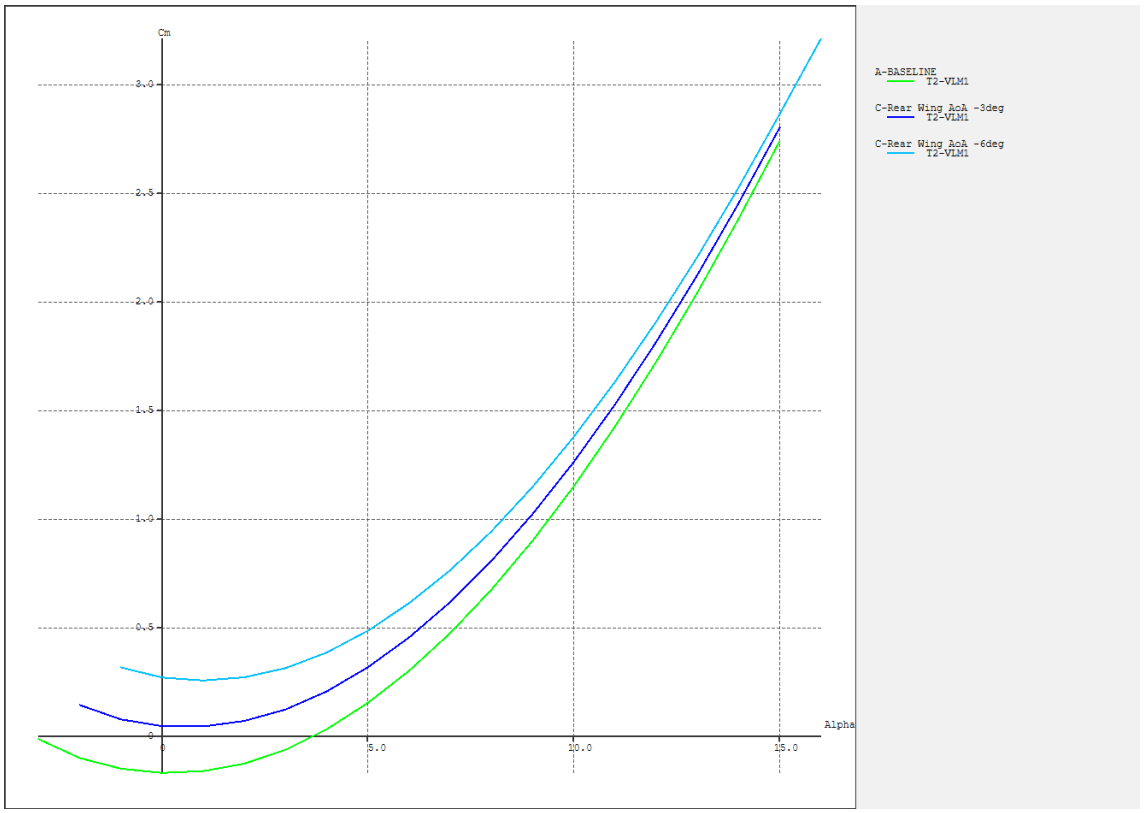

Figure 6: Rear wing angle of incidence effect.

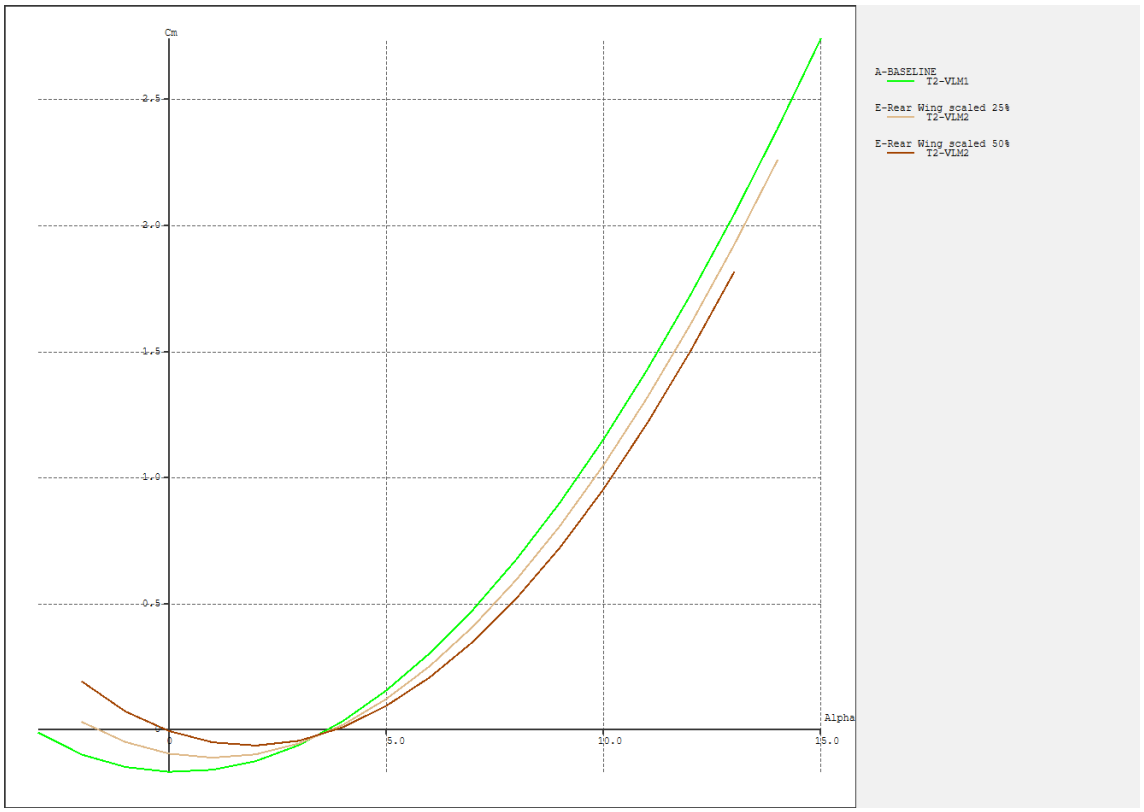

Figure 7: Rear wing area effect.

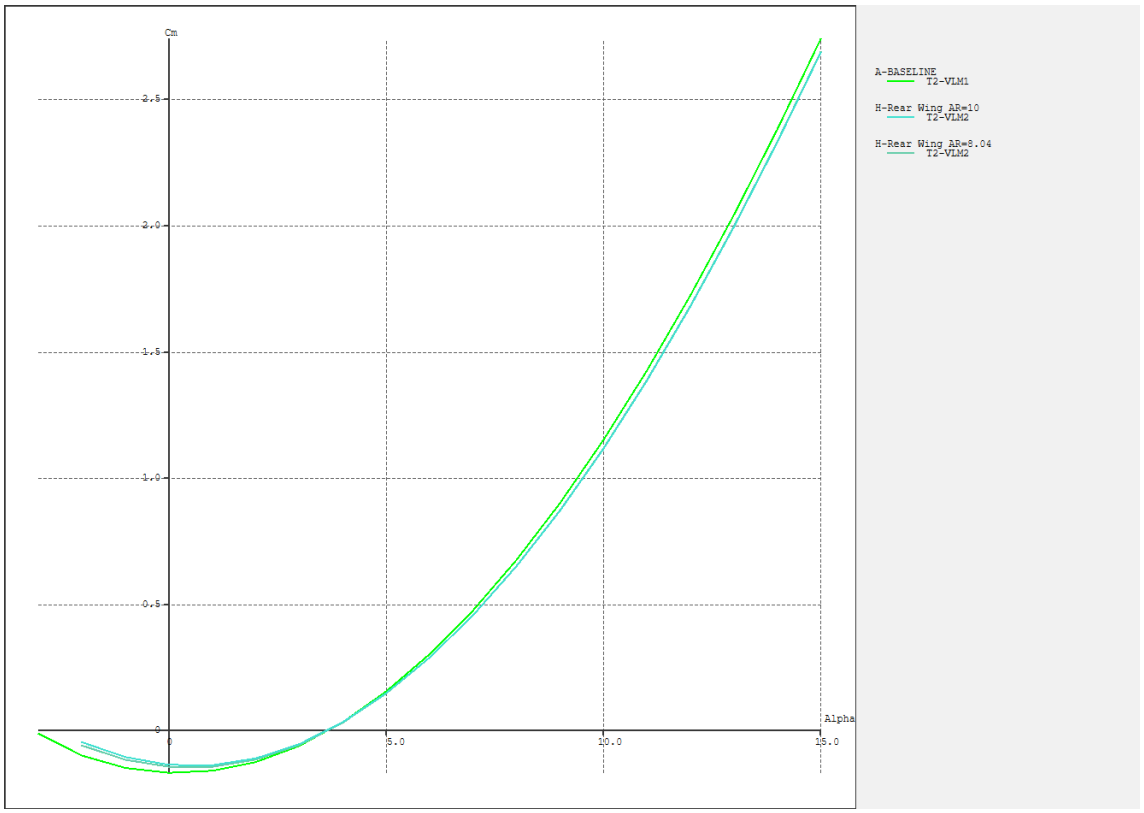

Figure 8: Rear wing aspect ratio effect.

C $C_L/C_D - \alpha$ plots

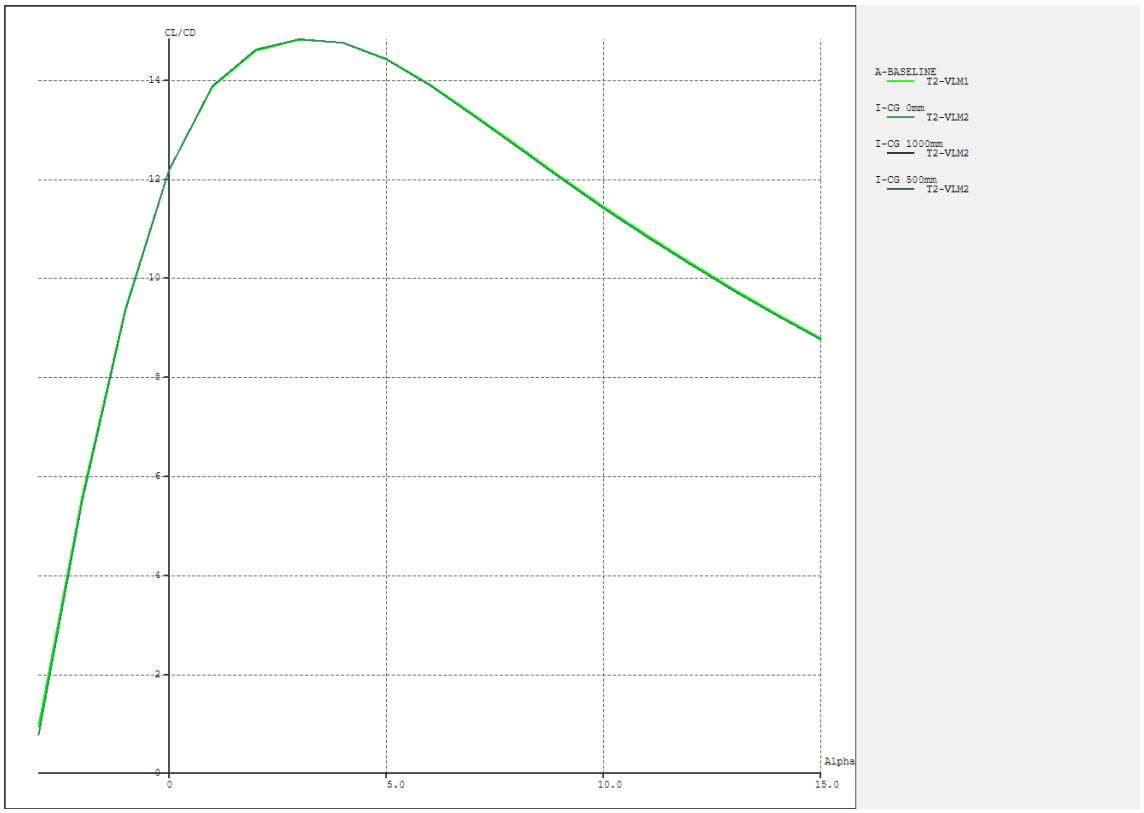

Figure 9: Vertical centre of gravity effect.

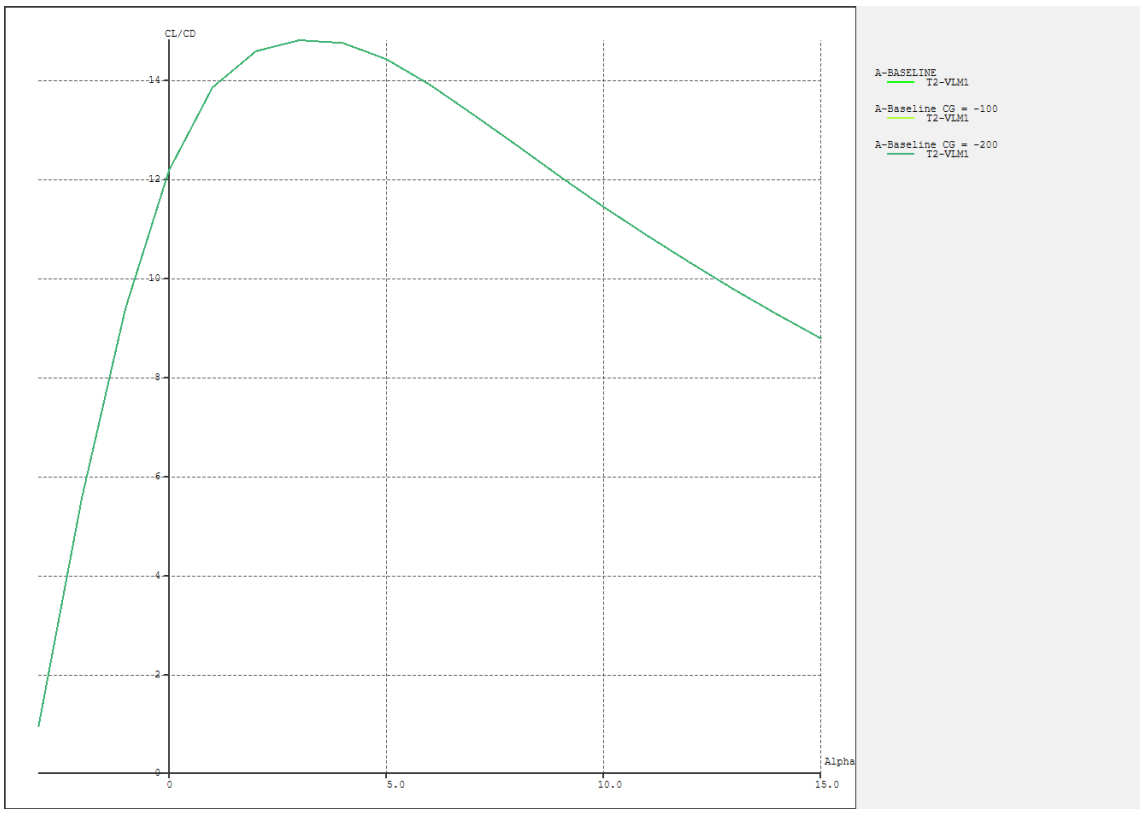

Figure 10: Longitudinal centre of gravity effect.

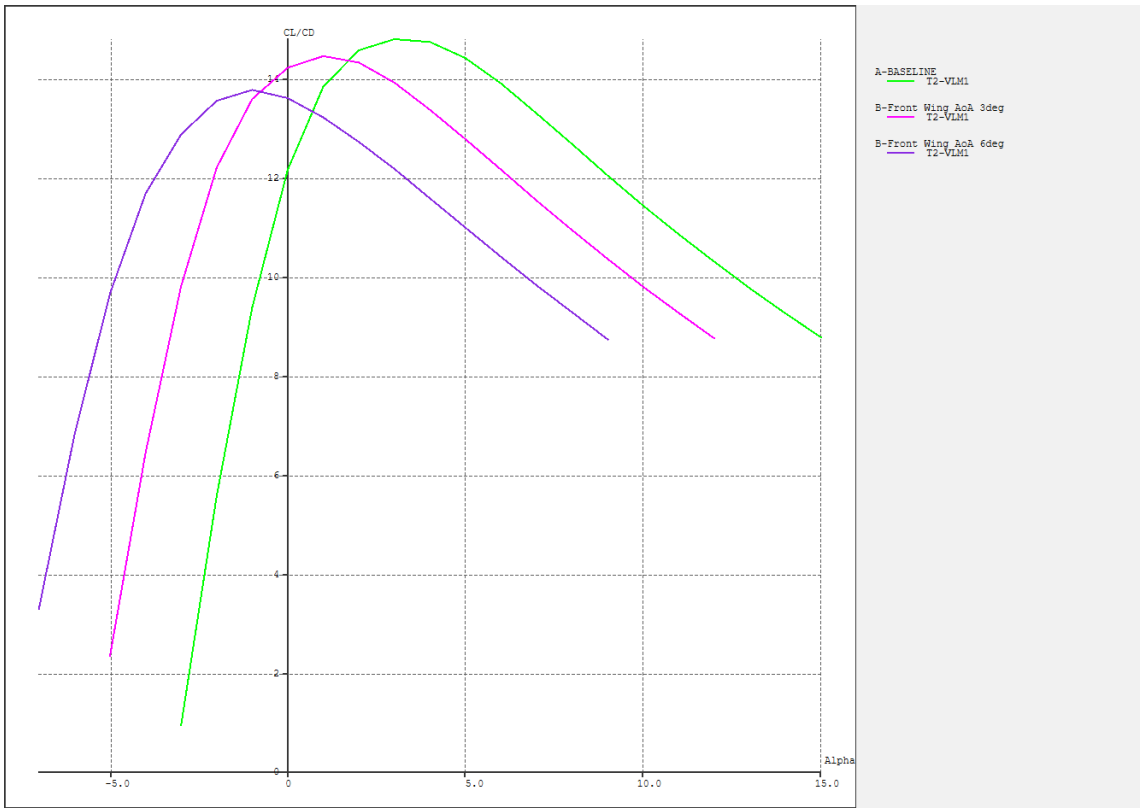

Figure 11: Front wing angle of incidence effect.

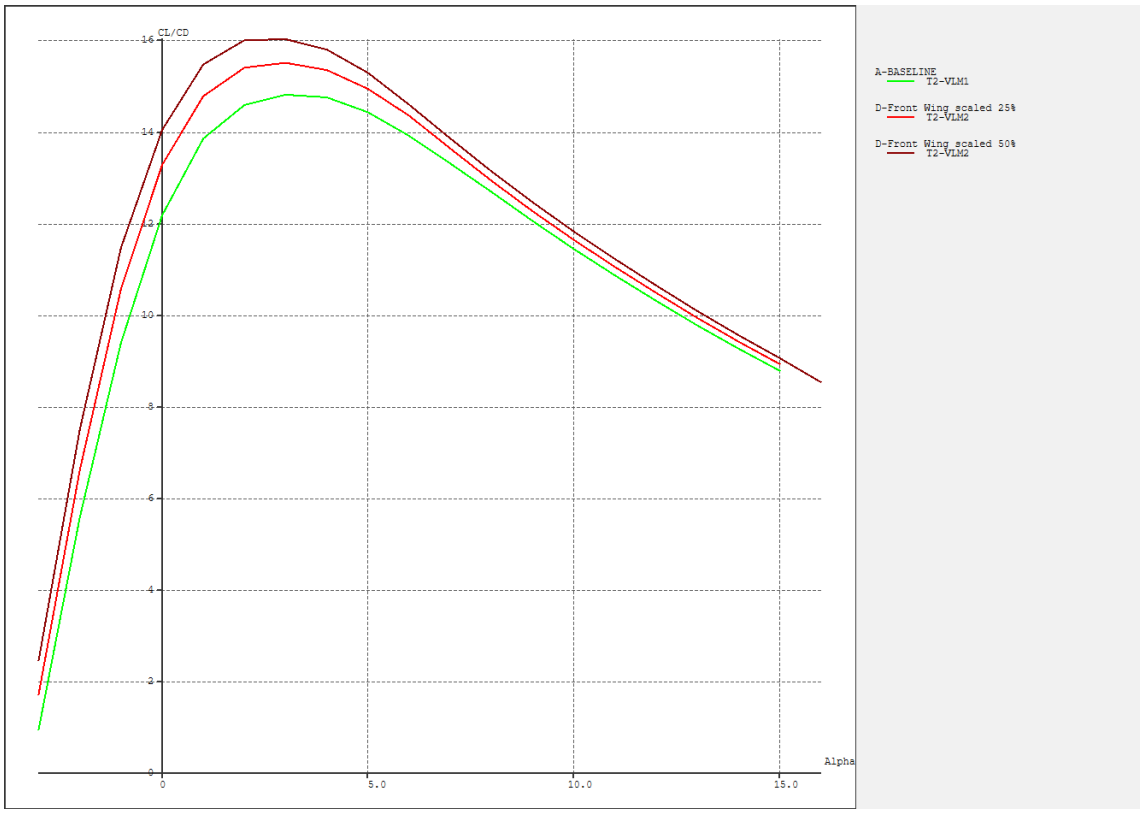

Figure 12: Front wing area effect.

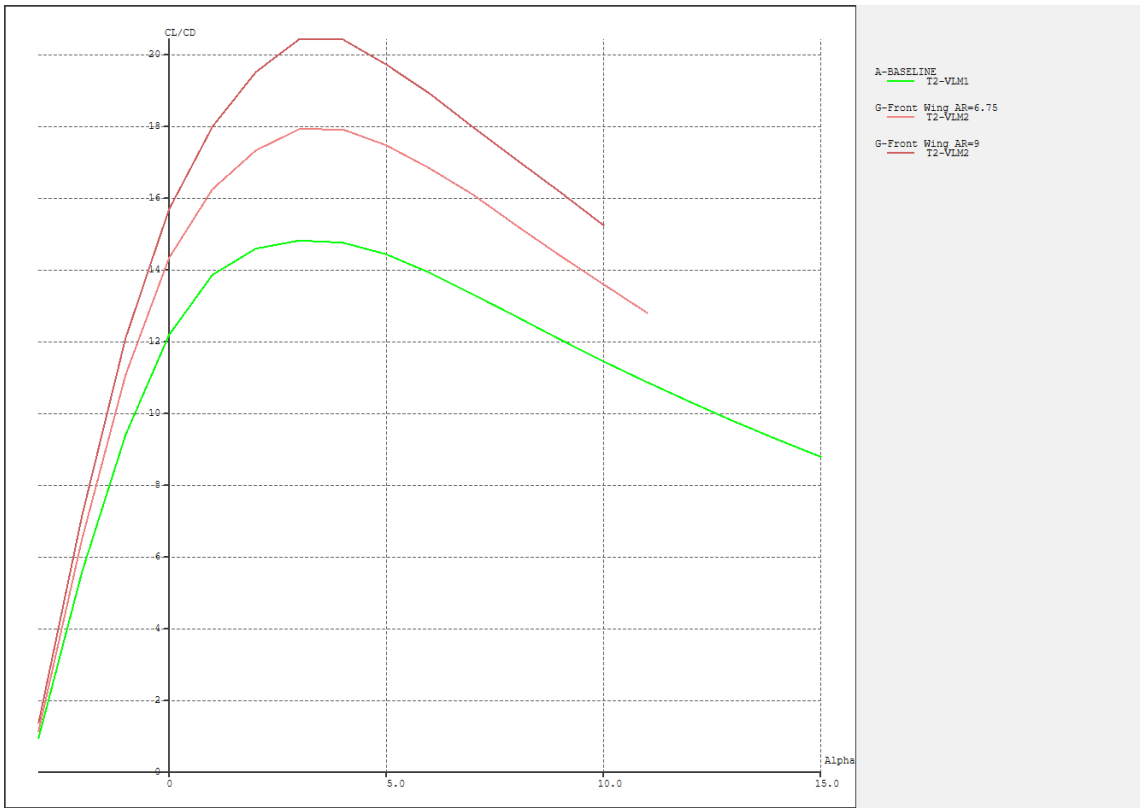

Figure 13: Front wing aspect ratio effect.

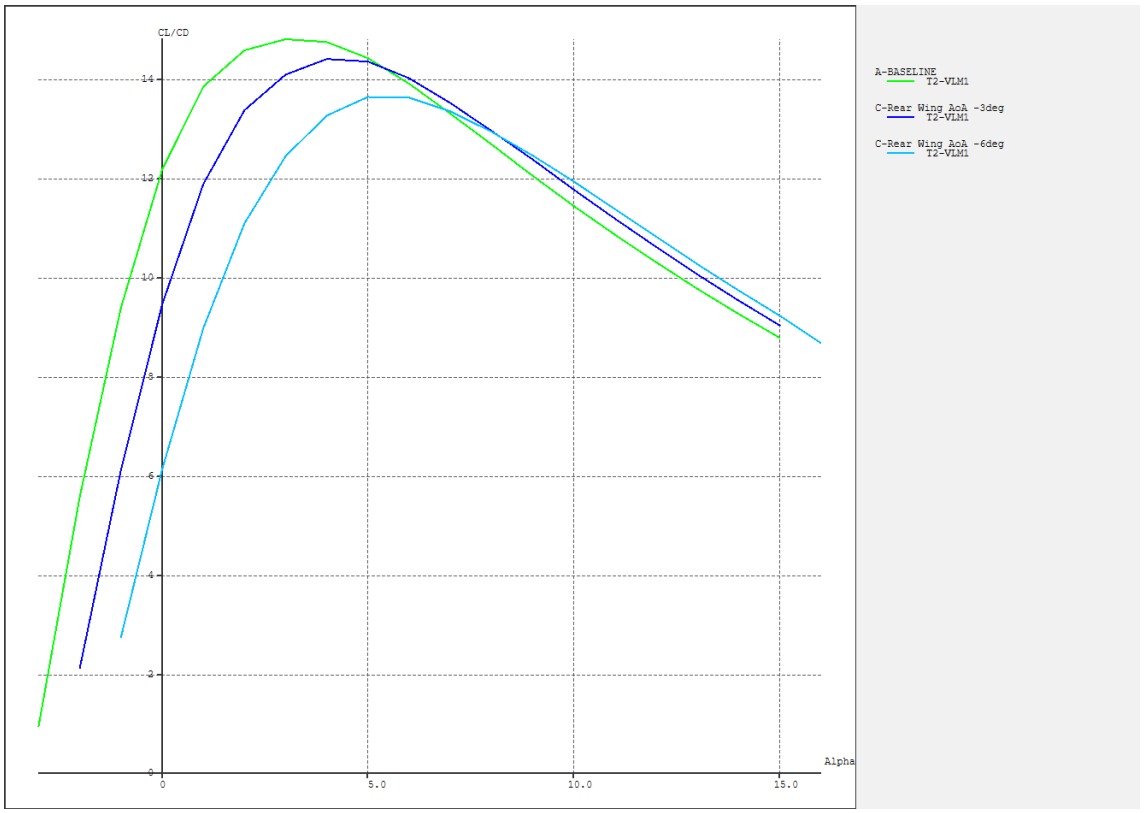

Figure 14: Rear wing angle of incidence effect.

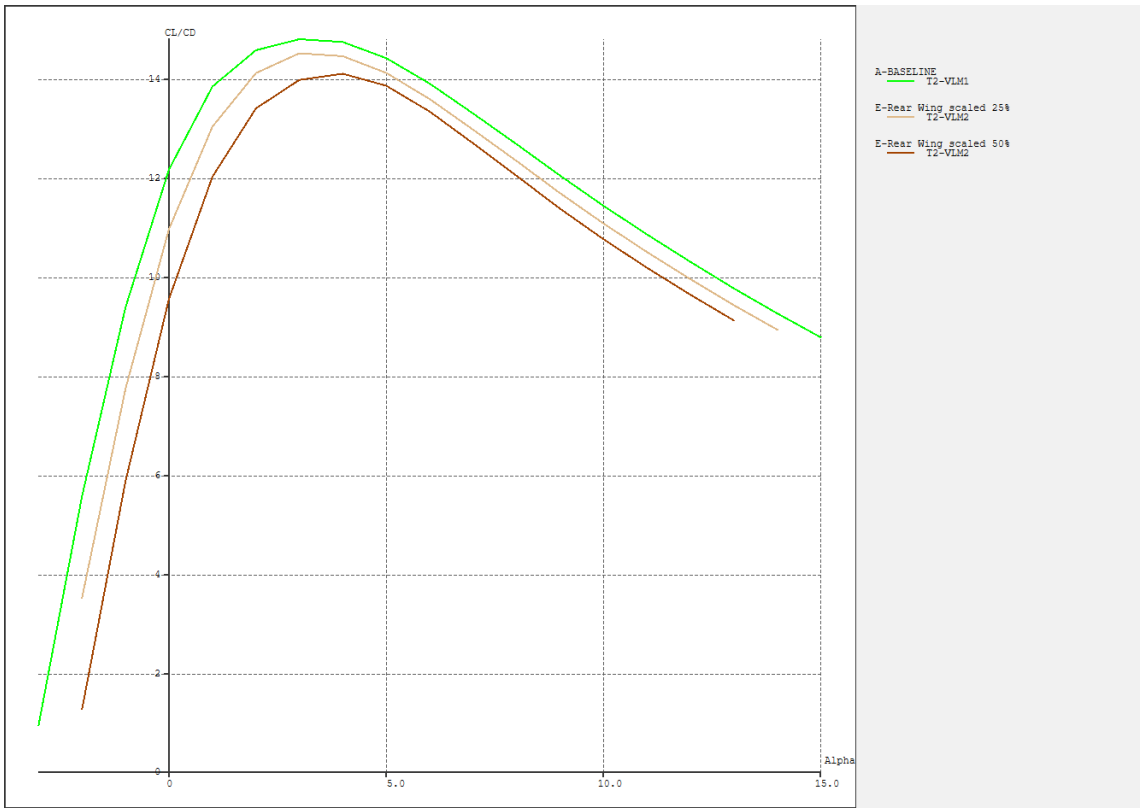

Figure 15: Rear wing area effect.

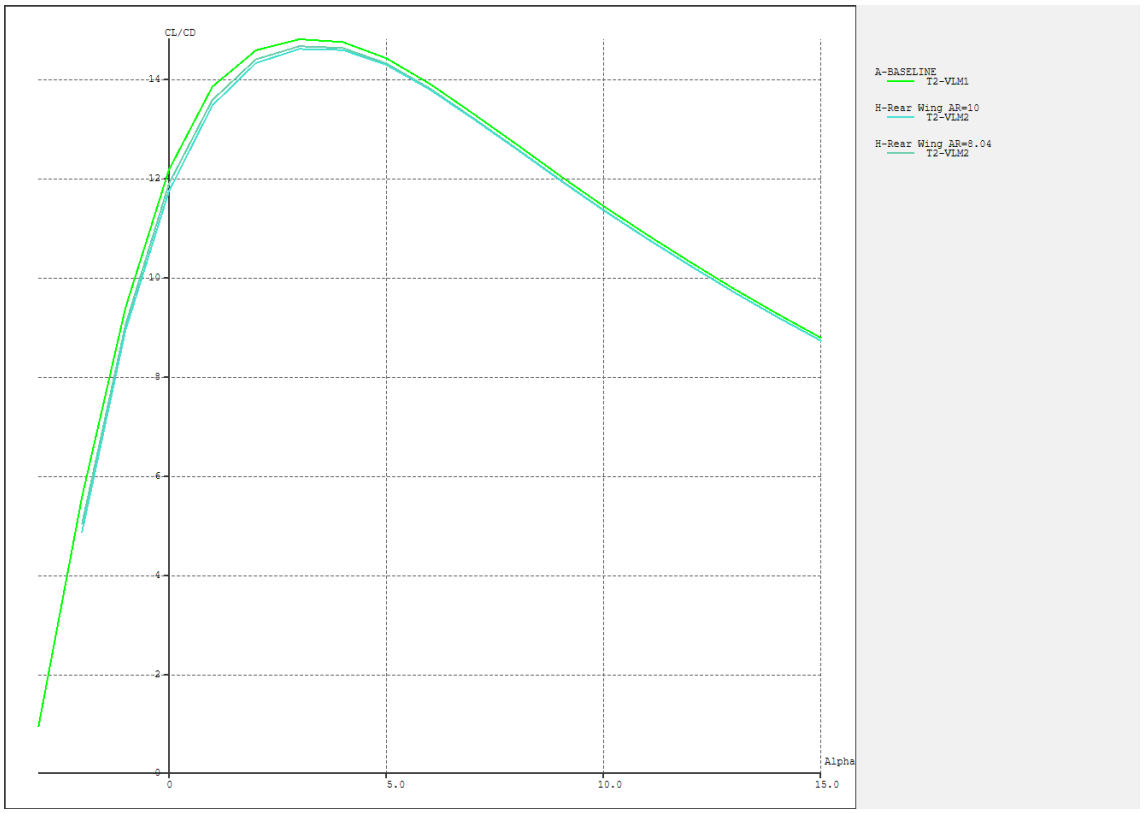

Figure 16: Rear wing aspect ratio effect.

D Python Script for Calculation of Modulus

```
import math
import pandas as pd
from matplotlib import pyplot as plt

Ef = float(input("Enter Ef [MPa]: "))
Em = float(input("Enter Em [MPa]: "))

Vf = [0.0, 0.1, 0.2, 0.3, 0.4, 0.5, 0.6, 0.7, 0.8, 0.9, 1.0]

E1_list = []
E2_list = []

for i in Vf:
    E1 = Ef * i + Em * (1.0 - i)
    E1_list.append(E1)

    E2 = (Ef * Em) / (Ef * (1 - i) + Em * i)
    E2_list.append(E2)

    print("Fibre Volume: " + str(i), "| Longitudinal modulus: " + str(E1) +
    ↪  "MPa", "| Transverse modulus: " + str(E2) + "MPa")

plt.plot(Vf, E1_list)
plt.plot(Vf, E2_list)
plt.title("Stress-volumeFraction")

plt.show()
```

E Python Code for Plotting Statistics

```
import pandas as pd
import matplotlib.pyplot as plt
import numpy as np
import shapely
from shapely.geometry import LineString, Point
# %matplotlib inline
from scipy.stats import norm

# SET VARIABLES -------------------------

L = 60  # Support Span mm
a = 20  # Loading Span mm
h = 4.05   # Thickness mm
b = 14.96  # Width mm

s1 = (0.0005*L**2)/(4.7*h) # Deflection 1
s2 = (0.0025*L**2)/(4.7*h) # Deflection 2

I = (b*h**3)/(12)

# f1 = 0  # Load 1
# f2 = 0  # Load 2

# sigma1 = 0
# sigma2 = 0

# EQUATIONS FROM ISO---------------------

# Ef = (0.21*L**3)/(b*h**3) * (f2-f1)/(s2-s1)

# Ef = 500*(sigma2 - sigma1)

# delta = (F*a)/(48*Ef*I) * (3*L**2 - 4*a**2)

# strain = (4.7*delta*h)/(L**2)

# IMPORTER FILER------------------------
sample1 = pd.read_csv()
sample2 = pd.read_csv()
sample3 = pd.read_csv()
sample4 = pd.read_csv()
sample5 = pd.read_csv()
sample6 = pd.read_csv()
sample7 = pd.read_csv()
sample8 = pd.read_csv()
sample9 = pd.read_csv()
sample10 = pd.read_csv()


file_list = [sample1, sample2, sample3, sample4, sample5, sample6, sample7,
↪  sample8, sample9, sample10]

x_list = []
y_list = []

sigma_list = []
```

```
epsilon_list = []
Ef_list = []    # List of flexural modulus
#deflection_list = []

# KOPIER VERDIENE FRA FILENE INN I LISTER
↪  ----------------------------------------

for file in file_list:
    x = []
    y = []

    sigma = []
    epsilon = []
    #deflection = []

    crosshead = file.iloc[:, 0]
    #print(crosshead.to_string())

    load = file.iloc[:, 1]
    #print(load.to_string())

    for s in crosshead:
        x.append(s)
        '''
        strain = (4.7*s*h)/(L**2)
        epsilon.append(strain)

    epsilon_list.append(epsilon)
    '''

    for F in load:
        y.append(F)
        stress = (F*L)/(b*h**2)
        sigma.append(stress)

    x_list.append(x)
    y_list.append(y)
    sigma_list.append(sigma)

    sigma1 = sigma[150]
    sigma2 = sigma[150 + 120]
    Ef = 500 * (sigma2 - sigma1)
    Ef_list.append(round(Ef, 2))

    # THIS ONLY WORKS IN THE LINEAR REGION
    for F in load:
        #delta = (F * a) / (48 * Ef * I) * (3 * L ** 2 - 4 * a ** 2)
        #strain = (4.7 * delta * h) / (L ** 2)
        #deflection.append(delta)

        M = (1 / 2) * F * (L / 2)  # Moment
        strain = (h * M / 2 * Ef * I)
        epsilon.append(strain)

    #deflection_list.append(deflection)
    epsilon_list.append(epsilon)

# PRINT STUFF ----------------------------
```

```
print('Ef list:')
print(Ef_list)
print('\n')
#print(s1)
#print(s2)

#print(len(epsilon_list[0]))
#print(len(sigma_list[0]))

#print(type(x_list[0][1]))
#print(type(Ef_list[0]))


# PLOT LOAD - DISPLACEMENT ----------------------------------------

v = []  # List of yield strength of the samples

for i in range(len(file_list)):

    # PLOT STRESS - DISPLACEMENT
    plt.plot(x_list[i], sigma_list[i])

    # PLOT OFFSET YIELD CURVE
    point1 = [x_list[i][30], sigma_list[i][30]]
    point2 = [x_list[i][300], sigma_list[i][300]]

    x_values = [point1[0], point2[0]]
    y_values = [point1[1], point2[1]]

    print(sigma_list[1].index(max(sigma_list[1])))

    m = (y_values[1] - y_values[0])/(x_values[1] - x_values[0])     # Slope Ef
    y_ex = y_values[0] + (m * (x_list[i][sigma_list[i].index(max(sigma_list[i]))]
    ↪  - x_values[0]))   # Extrapolation formula
    ex_point = [x_list[i][sigma_list[i].index(max(sigma_list[i]))], y_ex]
    # y_ex = y_values[0] + (m * (x_list[i][900] - x_values[0]))
    #ex_point = [x_list[i][900], y_ex]

    #b = -0.1 * m

    x_values.append(ex_point[0])
    y_values.append(ex_point[1])

    offsett_y_values = [m * (x-0.2) for x in x_values]  # Shift the line to the
    ↪  right

    #plt.plot(x_values, y_values)
    #plt.plot(x_values, offsett_y_values)   # Skru denne på

    # FIND INTERSECTION
    first_line = LineString(np.column_stack((x_list[i], sigma_list[i])))
    second_line = LineString(np.column_stack((x_values, offsett_y_values)))
    intersection = first_line.intersection(second_line)

    v.append(round(intersection.y, 2))

    # Skru på denne
```

```
    if intersection.geom_type == 'MultiPoint':
        plt.plot(*LineString(intersection).xy, 'o')
    elif intersection.geom_type == 'Point':
        plt.plot(*intersection.xy, 'o')

    print('SAMPLE ' + str(i+1))
    print('Ef: ' + str(Ef_list[i]))
    print('Intersection point:')
    print(intersection)
    print('Peak stress: ' + str(round(max(sigma_list[i]), 2)))
    print('\n')

plt.title('Stress and Displacement')
plt.xlabel('Displacement [mm]')
plt.ylabel('Stress [MPa]')
plt.grid()
plt.show()

# PLOT STRESS - STRAIN -------------------------
'''
for i in range(len(file_list)):
    plt.plot(epsilon_list[i], sigma_list[i])

plt.title('Stress and Strain')
plt.xlabel('Strain')
plt.ylabel('Stress [MPa]')
plt.grid()
plt.show()
'''

# PLOT STRENGTH STATS ------------------------

n    =  len(v)
vmin =  np.amin(v)
vmax =  np.amax(v)
vmean=  np.mean(v)
vstd =  np.std(v,ddof=1)
vcov =  100*vstd/vmean

print('----- STATS -----')
print('Sample size:', str(n), '\n')

print('--- Strength ---')
print('Min:        ', str(vmin))
print('Max:        ', str(vmax))
print('Mean:       ', str(vmean))
print('Stdev:      ', str(vstd))
print('COV%:       ', str(vcov))

x=np.linspace(vmin-3*vstd, vmax+3*vstd, 1000)
y=norm.pdf(x, vmean, vstd)
fig, ax = plt.subplots(figsize=(10, 4))
ax.plot(x, y, color='black')
n, bins, patches=plt.hist(v, bins=10, density=True, facecolor='orange', alpha=0.6
↪  )
ax.set_xlabel('Strength [MPa]')
ax.set_ylabel('Frequency')
```

```
ax.set_title('Normal distribution of strength')
ax.set_xlim(0,)
ax.set_ylim(0,)
ax.grid(True)
plt.show()

p050 = vmean-1.645*vstd
p025 = vmean-1.960*vstd

fig, ax = plt.subplots(figsize=(10, 4))
ax.plot(x, y, color='black')
ax.plot((p050, p050), (0, max(y)), '--', color = 'blue', label='5th percentile')
ax.plot((p025, p025), (0, max(y)), '--', color = 'red', label='2.5th percentile')
ax.set_xlabel('Strength [MPa]')
ax.set_ylabel('Frequency')
ax.set_title('Normal distribution of strength')
ax.set_xlim(0,)
ax.set_ylim(0,)
ax.grid(True)
ax.legend(loc='best')
plt.show()

print('5th percentile:  ', p050)
print('2.5th percentile:', p025)
print('\n')

# PLOT Ef STATS--------------------------

Ef_min =  np.amin(Ef_list)
Ef_max =  np.amax(Ef_list)
Ef_mean=  np.mean(Ef_list)
Ef_std =  np.std(Ef_list,ddof=1)
Ef_cov =  100*Ef_std/Ef_mean

print('--- Flexural Modulus ---')
print('Min:         ', str(Ef_min))
print('Max:         ', str(Ef_max))
print('Mean:        ', str(Ef_mean))
print('Stdev:       ', str(Ef_std))
print('COV%:        ', str(Ef_cov))

x=np.linspace(Ef_min-3*Ef_std, Ef_max+3*Ef_std, 1000)
y=norm.pdf(x, Ef_mean, Ef_std)
fig, ax = plt.subplots(figsize=(10, 4))
ax.plot(x, y, color='black')
n, bins, patches=plt.hist(Ef_list, bins=10, density=True, facecolor='orange',
↪  alpha=0.6 )
ax.set_xlabel('Flexural Modulus [MPa]')
ax.set_ylabel('Frequency')
ax.set_title('Normal distribution of modulus')
ax.set_xlim(0,)
ax.set_ylim(0,)
ax.grid(True)
plt.show()

#p050 = Ef_mean-1.645*Ef_std
#p025 = Ef_mean-1.960*Ef_std
p_low = Ef_mean-Ef_std
```

```
p_high = Ef_mean+Ef_std

fig, ax = plt.subplots(figsize=(10, 4))
ax.plot(x, y, color='black')
ax.plot((Ef_mean, Ef_mean), (0, max(y)), '--', color = 'red', label='Mean')
ax.plot((p_low, p_low), (0, max(y)), '--', color = 'blue', label='-sigma')
#ax.plot((p025, p025), (0, max(y)), '--', color = 'red', label='2.5th
↪  percentile')
ax.plot((p_high, p_high), (0, max(y)), '--', color = 'blue', label='+sigma')
ax.set_xlabel('Flexural Modulus [MPa]')
ax.set_ylabel('Frequency')
ax.set_title('Normal distribution of modulus')
ax.set_xlim(0,)
ax.set_ylim(0,)
ax.grid(True)
ax.legend(loc='best')
plt.show()

print('-sigma: ', p_low)
print('+sigma: ', p_high)
print('\n')
```

F Normal Distributions

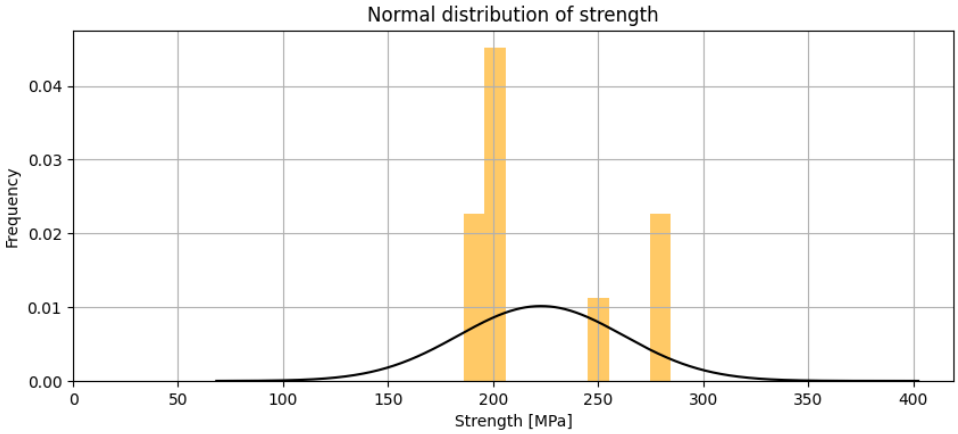

Figure 17: Normal distribution of strength for batch 1.

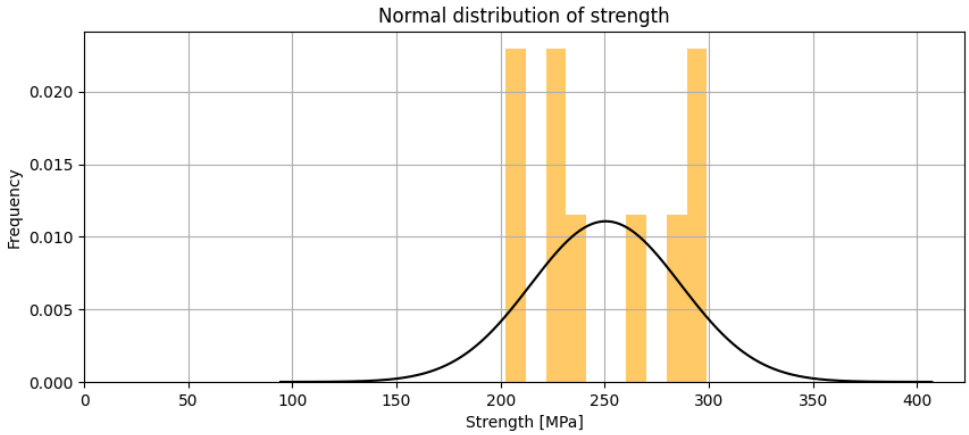

Figure 18: Normal distribution of strength for batch 2.

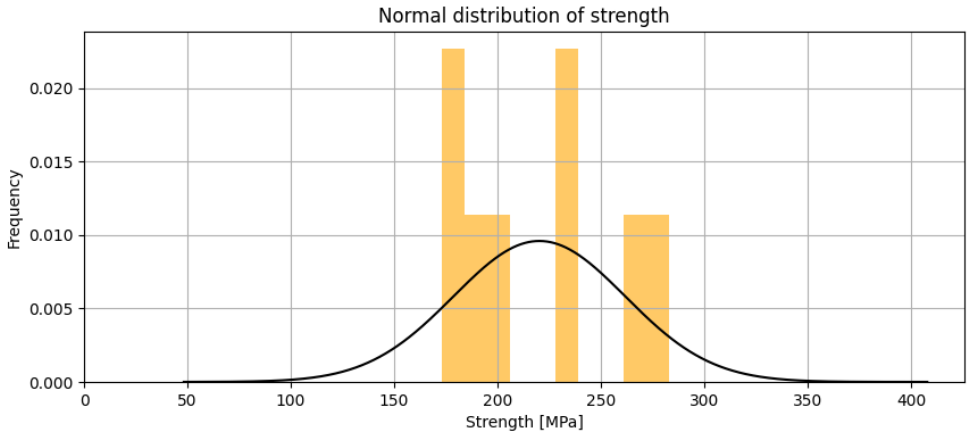

Figure 19: Normal distribution of strength for batch 3.

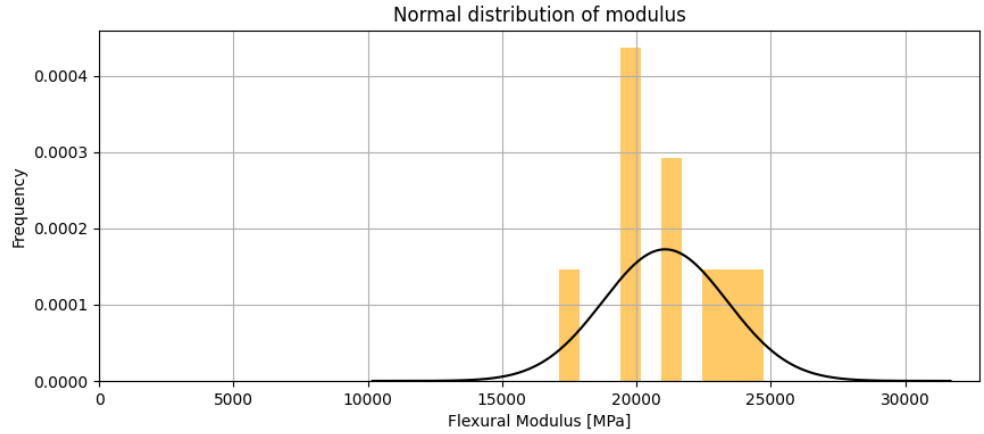

Figure 20: Normal distribution of elastic modulus for batch 1.

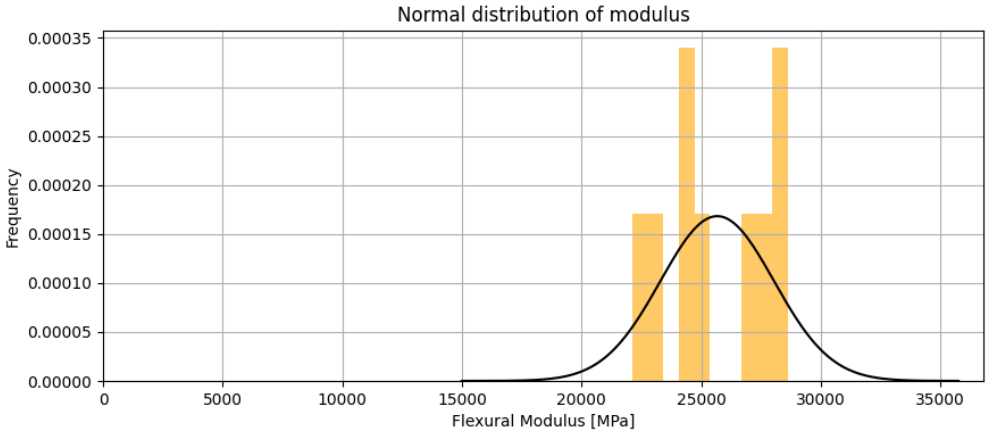

Figure 21: Normal distribution of elastic modulus for batch 2.

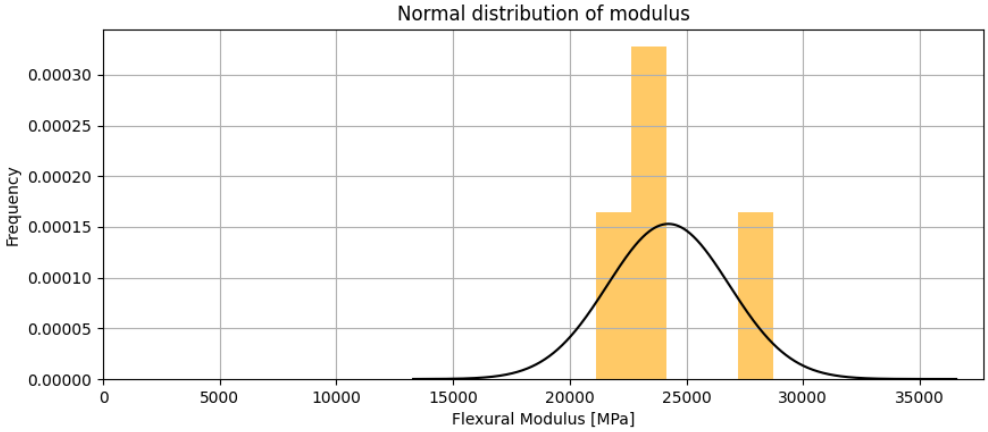

Figure 22: Normal distribution of elastic modulus for batch 3.

G Epoxy Data Sheet

HEXION

Technical Data Sheet

Issued: August 2006

EPIKOTE™ Resin MGS™ RIMR 135 and EPIKURE™ Curing Agent MGS™ RIMH 134–RIMH 137

CHARACTERISTICS

Approval	German Lloyd
Application	Specially designed for infusion processes (RMT, SCRIMP/VARI); rotor blades for wind turbines, boat and shipbuilding, sports equipment
Operational Temperature	-60 °C up to +50 °C (-76 °F up to 122 °F) without heat treatment -60 °C bis +80 °C (-76 °F up to 176 °F) after heat treatment
Processing	At temperatures between 10 °C and 50 °C (50-122 °F) due to the very low mixing viscosity especially suited for infusion, injection and pultrusion
Features	Very low viscosity, excellent initial curing properties at room temperature, pot life from approx. 0,5 hours to approx. 4 hours, short curing times at high temperatures
Storage	Shelf life of 24 months in originally sealed containers

APPLICATION

Very low viscosity laminating resin system with different pot lives for processing of glass, carbon and aramide fibers. Due to its good mechanical properties, this system is suitable for the production of components featuring high static and dynamic loadability.

The range of pot lives is between approx. 0,5 hour and 3-4 hours. The parts can be worked and demoulded after curing at room temperature. Curing at higher temperatures (up to approx. 80-100 °C, 176-212 °F) is possible, depending on layer thickness and geometry of the parts to be manufactured. The curing times can be reduced to a few minutes by this.

Adding internal parting agents, such as zinc stearate, etc., has proven useful for pultrusion processes. Profiles with good surface qualities are obtained. Depending on profile geometry, mould temperatures in the range of 180-230 °C (356-446 °F) are possible, thus permitting high drawing speeds.

The mixing viscosity is very low, which is especially advantageous for infusion and injection processes. It may be lowered to approx. 150 mPas by heating the resin mass (see diagram). This means that even complicated molded parts with long flow paths can be easily infused. The temperature rise with hardener RIMH 137 remains very low up to a mold temperature of approx. 30 °C, so that even parts of greater thickness can be produced at elevated temperatures.

The infusion resin system does not contain any unreactive components. The raw materials used feature a

Figure 23: Page 1 of the Epocote RIMR 135/RIMR 137 resin system.

MIXING RATIOS

	Infusion Resin RIMR 135 : Hardener RIMH 134 – RIMH 137
Parts by weight	100 : 30 ± 2
Parts by volume	100 : 36 ± 2

The specified mixing ratios must be observed as exactly as possible. Adding more or less hardener will not effect a faster or slower reaction - but in incomplete curing which cannot be corrected in any way. Resin and hardener must be mixed very thoroughly. Mix until no clouding is visible in the mixing container. Pay special attention to the walls and the bottom of the mixing container.

TEMPERATURE DEVELOPMENT

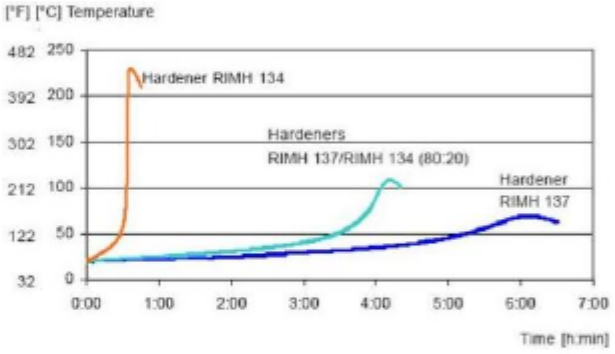

Quantity: 100 g / 20 °C (77 °F)

The optimum processing temperature is in the range between 20 °C and 25 °C (68-77 °F). Higher processing temperatures are possible, but will shorten pot life. A rise in temperature of 10 °C (50 °F) will halve the pot life. Water (for example very high humidity or contained in fillers) causes an acceleration of the resin/hardener reaction. Different temperatures and humidities during processing have no significant effect on the strength of the hardened product.

Do not mix large quantities - particularly of highly reactive systems - at elevated processing temperatures. The heat flow from the mixing container is very low, so the contents will heat up fast because of the dissipating reaction heat (exothermic resin-hardener reaction). This can result in temperatures of more than 200 °C (392 °F) in the mixing container, which may cause smoke-intensive burning of the resin mass.

Figure 24: Page 4 of the Epocote RIMR 135/RIMR 137 resin system.

MECHANICAL DATA

Mechanical Data of Neat Resin		
Density	[g/cm³]	1,18 - 1,20
Flexural strength	[N/mm²]	90 - 120
Modulus of elasticity	[kN/mm²]	2,7 - 3,2
Tensile strength	[N/mm²]	60 - 75
Compressive strength	[N/mm²]	80 - 90
Elongation of break	[%]	8 - 16
Impact strength	[KJ/m²]	70 - 80
Water absorption at 23 °C	24 h [%] 7 d [%]	0,10 - 0,20 0,20 - 0,50
Fatigue strength under reversed bending stresses acc. to DLR Brunsw.	10% 90%	exp. > 1 x 10^6 exp. > 2 x 10^6
Curing: 24 h at 23° C (74° F) + 15 h at 60° C (140° F), partly cured/full cure Typical data according to WL 5.3203 Parts 1 and 2 of the GERMAN AVIATION MATERIALS MANUAL		

Advice: Mechanical data are typical for the combination of laminating resin RIMR 135 with hardener RIMH 137. Data can differ in other applications.

Figure 25: Page 7 of the Epocote RIMR 135/RIMR 137 resin system.

H Prototype Molds

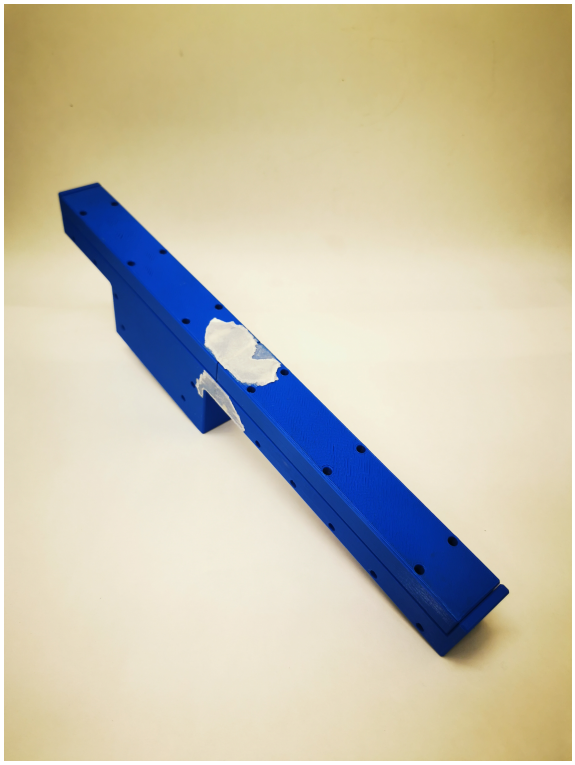

(a) The fuselage mold parts fitted together.

(b) The materials used for the forging of the fuselage.

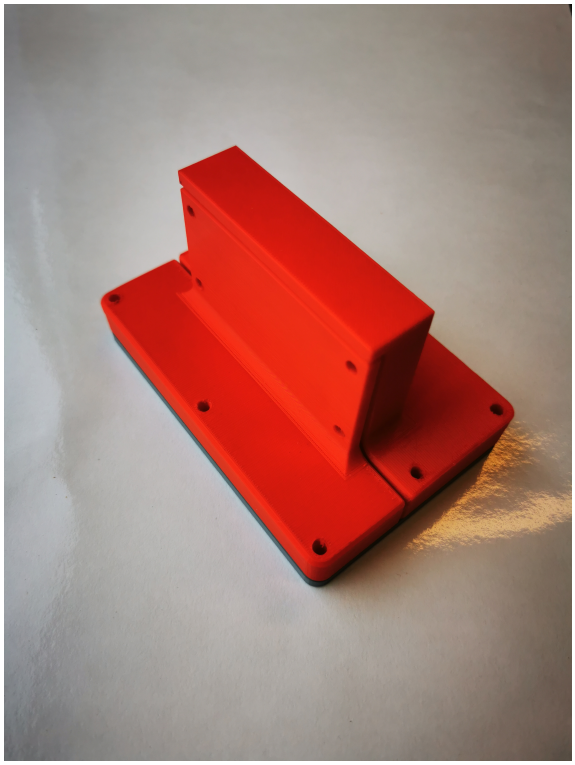

(c) The mounting plate mold parts fitted together.

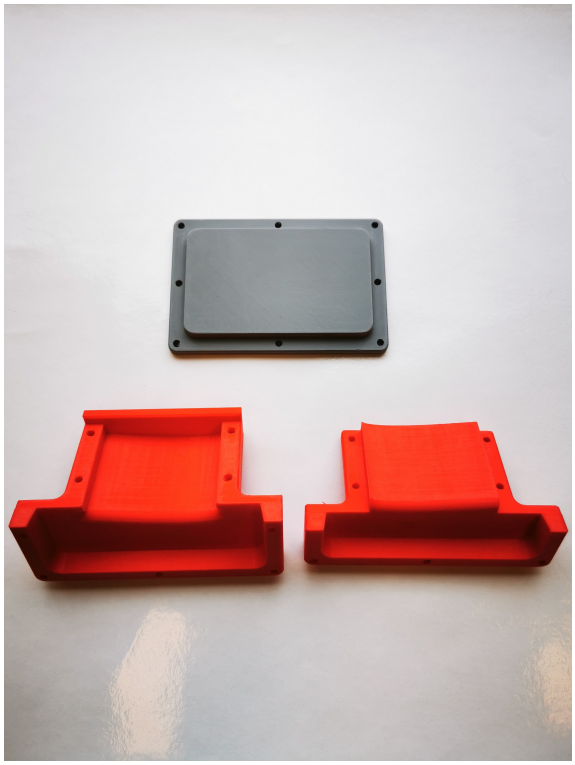

(d) Exploded view of the mounting plate mold.

Figure 26: Pictures of the prototype mold.

Kristoffer Sjøwall

Hydrodynamic Design Principles and Structural Verification of a Hydrofoil Concept for Kiteboarding

NTNU
Norwegian University of
Science and Technology